



**HAL**  
open science

**Graphene: FET and Metal Contact Modeling.  
Graphène : modélisation du FET et du contact  
métallique**

Giancarlo Vincenzi

► **To cite this version:**

Giancarlo Vincenzi. Graphene: FET and Metal Contact Modeling. Graphène : modélisation du FET et du contact métallique. Micro and nanotechnologies/Microelectronics. Université Paul Sabatier - Toulouse III, 2014. English. NNT : . tel-00938701

**HAL Id: tel-00938701**

**<https://theses.hal.science/tel-00938701v1>**

Submitted on 29 Jan 2014

**HAL** is a multi-disciplinary open access archive for the deposit and dissemination of scientific research documents, whether they are published or not. The documents may come from teaching and research institutions in France or abroad, or from public or private research centers.

L'archive ouverte pluridisciplinaire **HAL**, est destinée au dépôt et à la diffusion de documents scientifiques de niveau recherche, publiés ou non, émanant des établissements d'enseignement et de recherche français ou étrangers, des laboratoires publics ou privés.



Université  
de Toulouse

# THÈSE

En vue de l'obtention du

## DOCTORAT DE L'UNIVERSITÉ DE TOULOUSE

Délivré par :

Université Toulouse 3 Paul Sabatier (UT3 Paul Sabatier)

---

**Présentée et soutenue par :**

**Giancarlo VINCENZI**

**le** lundi 13 janvier 2014

**Titre :**

Graphene: FET and Metal Contact Modeling  
Graphène : modélisation du FET et du contact métallique

---

**École doctorale et discipline ou spécialité :**

ED GEET : Électromagnétisme et Systèmes Haute Fréquence

**Unité de recherche :**

Laboratoire d'Analyse et Architecture de Systèmes

**Directeur(s) de Thèse :**

Patrick PONS, Fabio COCCETTI

**Jury :**

Thierry PARRA, Président du Jury

Marco FARINA, Rapporteur

George KONSTANTINIDIS, Rapporteur

Patrick PONS, Directeur de Thèse

Fabio COCCETTI, Co-directeur de Thèse

Charlotte TRIPON-CANSELIET, Examineur

Luca PIERANTONI, Invité

George DELIGEORGIS, Invité



# *Abstract*

Doctor of Philosophy

## **Graphene: FET and metal contact modeling**

by Giancarlo VINCENZI

Nine years have passed since the discovery of graphene, all of them dense of research works and publications that, piece by piece, shed more light on the properties of this extraordinary material. With more understanding of its best qualities, a more precise prospect of the applications that would better profit from its use has been defined. High Frequency devices, like mixers and power amplifiers, and Flexible and Transparent electronics are the most promising fields.

In those fields great attention is devoted to two subjects: the downscaling of the dimensions of the graphene transistor, in order to reduce the carriers travel time and attain increasingly larger fractions of ballistic electronic transport; and the optimization of the contact parasitics. Both are highly beneficial to the maximization of the device's RF Figures Of Merit.

In this thesis, Two models have been developed to address such topics: the first served both the quasi-ballistic large-area graphene and graphene nanoribbon transistors. It demonstrated the correlation between ballistic and diffusive electron transport and device length, and extracted the large signal DC currents and transconductances. The second reproduced the high-frequency conduction through graphene and its contact parasitics. The latter also motivated the development and fabrication of a RF test bed on a dedicated plastic technology, enabling the RF characterization of the contact impedance and of the specific interfacial impedance of monolayer CVD graphene.



# Contents

<b>Abstract</b>	<b>ii</b>
<b>List of Figures</b>	<b>v</b>
<b>List of Tables</b>	<b>vii</b>
<b>1 Introduction</b>	<b>1</b>
1.1 Thesis structure . . . . .	3
<b>2 Literature Review</b>	<b>5</b>
2.1 Graphene Technology . . . . .	5
2.1.1 Graphene Isolation and synthesis . . . . .	5
2.2 Graphene Physics . . . . .	8
2.2.1 Electronic Bandstructure . . . . .	8
2.2.2 Consequences of the absence of bandgap . . . . .	9
2.3 Graphene FET models . . . . .	11
2.3.1 Physical models . . . . .	12
2.3.2 Empirical models . . . . .	14
2.4 Graphene/metal contact and propagation models . . . . .	15
2.4.1 Physical and Chemical models of the contact . . . . .	16
2.4.2 DC models and measurements . . . . .	24
2.4.3 RF measurements and models . . . . .	25
2.5 Conclusions . . . . .	27
<b>3 Graphene DC model</b>	<b>39</b>
3.1 Motivation . . . . .	39
3.2 Objectives of the study . . . . .	40
3.3 Model: Top of the Barrier . . . . .	40
3.3.1 The Landauer Equation, carriers and contacts . . . . .	41
3.3.2 Electrostatics . . . . .	43
3.3.3 The channel population: closing the loop . . . . .	44
3.4 Method: Extending the model to GFETs . . . . .	46
3.4.1 Scattering and channel population . . . . .	47
3.5 Results . . . . .	49
3.5.1 GNRFET . . . . .	49
3.5.2 GFET . . . . .	50
3.6 Future work . . . . .	53

3.7	Conclusions . . . . .	53
<b>4</b>	<b>Graphene RF model</b>	<b>57</b>
4.1	Motivation . . . . .	57
4.2	Objectives of the study . . . . .	58
4.3	Model . . . . .	59
4.4	Method . . . . .	60
4.4.1	Technology and design . . . . .	61
4.4.2	EM model (MoM) and schematic . . . . .	61
4.5	Results . . . . .	63
4.5.1	Performance projection with other graphene materials . . . . .	64
4.6	Chapter conclusions and future/ongoing work . . . . .	65
<b>5</b>	<b>Plastic test beds</b>	<b>69</b>
5.1	Motivation . . . . .	69
5.2	Objectives of the study . . . . .	71
5.2.1	Design Specifications . . . . .	71
5.3	Method . . . . .	72
5.3.1	Technology . . . . .	72
5.3.1.1	Fabrication of CPW on SiO <sub>2</sub> /HR Silicon . . . . .	73
5.3.1.2	Fabrication of CPW on Polymeric substrates . . . . .	73
5.3.2	Design . . . . .	75
5.3.2.1	Modeling . . . . .	76
5.3.3	Fabricated structures . . . . .	80
5.3.3.1	De-embedding . . . . .	86
5.4	Results: Graphene monolayer, CVD . . . . .	90
5.5	Future work . . . . .	91
5.6	Conclusions . . . . .	92
<b>6</b>	<b>Conclusions</b>	<b>95</b>
6.1	Future work . . . . .	96

# List of Figures

2.1	Quality vs. Cost for graphene production . . . . .	8
2.2	Work functions of metal and Graphene in contact . . . . .	18
2.3	Potential and resistivity along the channel of a graphene FET . . . . .	20
2.4	Access resistance of a double-gate graphene FET . . . . .	21
2.5	TLM circuit . . . . .	24
3.1	Cross-section of a graphene FET . . . . .	41
3.2	Electrostatic part of the problem . . . . .	43
3.3	Injection of carriers into the channel . . . . .	45
3.4	Quasi-ballistic injection into a nanoscale semiconductor . . . . .	46
3.5	Quasi-ballistic injection in graphene . . . . .	48
3.6	$I_d$ - $V_{gs}$ of FET1 . . . . .	50
3.7	Structure of FET2 . . . . .	51
3.8	$I_d$ ( $V_{sd}$ ) of FET2 . . . . .	51
4.1	Small signal circuit of a FET . . . . .	57
4.2	EC of the FET and its parasitics . . . . .	59
4.3	Microphotograph of the CPW . . . . .	60
4.4	SEM of the CPW . . . . .	60
4.5	CPW test bed . . . . .	62
4.6	Reference structure S-parameters . . . . .	63
4.7	Graphene-loaded structure S-parameters . . . . .	63
4.8	S-parameters, prospective simulation . . . . .	65
5.1	De-embedding standards . . . . .	70
5.2	HRS MoM layout . . . . .	73
5.3	Graphene on HRS, process steps . . . . .	74
5.4	Graphene on Polyimide, process steps . . . . .	74
5.5	Photograph of PI sample . . . . .	75
5.6	Layout of the full period . . . . .	77
5.7	Final layout . . . . .	79
5.8	BCB MoM simulations . . . . .	80
5.9	Open-Short $ S_{21} $ difference, MoM simulations . . . . .	81
5.10	SU8 sample electrode separation in SEM . . . . .	82
5.11	PI sample electrode separation in SEM . . . . .	83
5.12	Total losses for HRS, SU8 and PI compared . . . . .	84
5.13	SU8 sample, meas. and MoM sim. compared . . . . .	85
5.14	PI sample, meas. and MoM sim. compared . . . . .	85



5.15 Test DUT circuit . . . . .	86
5.16 TRL de-embedding . . . . .	87
5.17 Open-Short and Cascade-Thru compared . . . . .	89
5.18 Equivalent circuit . . . . .	91
5.19 Graphene devices measurements and simulations . . . . .	91

# List of Tables

2.1	Contact Resistance at Room Temperature . . . . .	16
2.2	Contact Resistance at Low Temperature . . . . .	16
3.1	Structure dimensions . . . . .	49
3.2	Simulated $g_m$ for FET1 . . . . .	50
3.3	Peak transconductance $g_m$ for FET2 . . . . .	52
3.4	Fit parameters for FET1 and FET2 . . . . .	52
3.5	Model Comparison . . . . .	53
4.1	MoM simulation materials . . . . .	62
4.2	Comparison of contact resistances . . . . .	64
4.3	Simulated performance comparison with alternative solutions . . . . .	65
5.1	TRL Line standards . . . . .	76
5.2	Materials param for $Z_0$ . . . . .	78
5.3	CPW line parameters . . . . .	78
5.4	Errors of de-embedding techniques . . . . .	89
5.5	Open-Short and Cascade-Thru de-embedding errors compared . . . . .	89
5.6	Measured DC resistance values . . . . .	90
5.7	Extracted contact and sheet resistances . . . . .	90



# Chapter 1

## Introduction

Graphene, in its simplest definition, is a single atomic sheet isolated out of the graphitic stack. In each one of these sheets, carbon atoms occupy the vertices of hexagons in what is sometimes called the *honeycomb lattice*. They form a very strong  $\sigma$  bond with the three adjacent atoms through  $sp^2$  hybridization. The remaining 2p orbital is then available to form a  $\pi$  bond with adjacent atoms. The so formed extended  $\pi$ -electron system allows for the electronic conduction in graphene and determines its electrical and optical properties [1]. Graphene is one of the many allotropes in which molecular carbon can be found and some of them are related to its very structure. Fullerenes and Carbon Nanotubes (CNT) are hollow structures where the graphene sheet is rolled on itself or around an axis (the *tube axis*, orthogonal to the *chiral vector*), while graphite is the result of stacking graphene planes in the hexagonal (AB) or rhombohedral (ABC) order. The characteristics of those allotropes thus derive directly from graphene. The strength of its  $sp^2$  bonds and its consequent chemical stability are the ground for its excellent mechanical properties: a Young's modulus of 1 TPa [2], which is more than the double of silicon carbide [3], and a breaking strength virtually 100 times larger than a steel film of the same thickness.

Electrical properties of graphene are just as good as, or even more exciting than, mechanical ones: electron mobilities beyond  $2.5 \times 10^5 \text{ cm}^{-2}\text{V}^{-1}\text{s}^{-1}$  have been found *at room T*, four times than state of art III-V semiconductors [4] and 200 times that of Si, thanks to the reduced electron-phonon interaction [5] when the substrate is carefully chosen [6] or eliminated by suspension technology [7]. These high values are associated with long distances between scattering events for traveling electrons: mean free paths larger than  $1 \mu\text{m}$  have been reported [6], allowing the exploration of room-temperature ballistic transport electronics with existing technological capabilities. Higher values of mobilities were obtained for graphene suspended devices at liquid helium temperatures

(more than  $1.0 \times 10^6 \text{ cm}^{-2}\text{V}^{-1}\text{s}^{-1}$ , [8]), but not yet as good as compound semiconductors ( $35 \times 10^6 \text{ cm}^{-2}\text{V}^{-1}\text{s}^{-1}$  has been achieved, [9]), supporting and limiting the interest in room temperature operation.

Graphene's performance in electron and thermal conduction are full of records: electron saturation velocities demonstrated experimentally and theoretically up to  $7 \times 10^7 \text{ cm/s}$  [10],[11], much higher than both peak and high-field saturation velocities for Si and III-V semiconductors; current density as large as  $10^8 \text{ A/cm}^2$  [12], five orders of magnitude higher than copper interconnects; in-plane thermal conductivity higher than  $3,000 \text{ Wm}^{-1}\text{K}^{-1}$  [13], larger than single-crystal diamond and ten times larger than copper.

Finally, optical properties of graphene are very peculiar too: an optical opacity of 2.3% over a very broad spectrum, practically wavelength-independent in the range between far-infrared and blue light [14]. Moreover, compared with other semiconductors used as saturable absorbers, graphene absorbs more photons per unit surface and unit thickness, meaning greater efficiency per volume and greater chances to saturate with high-intensity light pulses.

However, graphene's properties are such for the isolated single layer, and stacking more layers on top of each other gives mere graphite as a result, a quite different material from graphene. This means that the great majority of physical properties that depend also on the thickness of the material, such as the sheet resistance, the maximum current density, and the optical absorptivity per surface, show values that, even when comparable with established technologies, are not excellent.

Graphene has been shown to really be a unique material, with many excellent properties that cannot be found altogether in one material alone. However, the unsatisfying values of other essential properties hinder its application as a replacement for every electronic technology developed up to date: In high frequency electronics, graphene will not likely replace Si or III-V semiconductors in the short term. The domain of flexible and transparent electronics instead is quickly gaining momentum, since today's most used material, Indium-Tin Oxide, is increasingly expensive and difficult to find. Graphene, with its superior mechanical and optical properties has already attracted the attention of consumer electronics giants like Samsung and Sony [15]. Both high frequency and flexible electronics domains need an accurate study of graphene's contact parasitics. Finally, there's an entirely new domain that can be explored and that can pave the way for millimeter waves and THz electronics, and that is room-temperature ballistic electronics [16]. This thesis will scrutinize the effects of ballistic transport and the contact parasitics, respectively on field effect transistors and interconnects.

## 1.1 Thesis structure

Chapter 2 will introduce a collection of fundamental concepts about the physics of graphene. This will be used to review and understand the state of the art on graphene modeling. Two main subjects will be discussed: in the first part a survey of the modeling of graphene field effect transistors in DC will be done; in the second part, the modeling of graphene passive structures will be reviewed. The metal contact and the electronic propagation in graphene are considered as two deeply connected aspects of the same subject, and their analysis will be developed in both DC and RF.

In Chapter 3 the DC model of a graphene nanoribbon FET will be presented, along with the modifications needed to extend it to large-area graphene devices.

In Chapter 4 an RF structure, a CPW line, loaded with graphene, will be analyzed by means of an equivalent circuit for graphene and electromagnetic modeling of the line. This will allow for the extraction of the metal/graphene contact impedance.

In Chapter 5 the design of an improved RF structure with a set of deembedding standards will be shown, along with measurements, analysis of the EM data and retro-simulations results. This will provide a low-loss access fixture for the RF characterization of graphene and deembedding of data. The graphene sheet and contact impedance will be measured and analyzed in both low and high frequency.

In the Conclusions chapter the innovations to the state of art contained in this manuscript will be resumed, and possible new directions of work will be outlined.

## References

- [1] P. Wallace, “The Band Theory of Graphite”, *Physical Review*, vol. 71, no. 9, pp. 622–634, May 1947. DOI: [10.1103/PhysRev.71.622](https://doi.org/10.1103/PhysRev.71.622).
- [2] C. Lee, X. Wei, J. W. Kysar, and J. Hone, “Measurement of the elastic properties and intrinsic strength of monolayer graphene.”, *Science (New York, N.Y.)*, vol. 321, no. 5887, pp. 385–8, Jul. 2008. DOI: [10.1126/science.1157996](https://doi.org/10.1126/science.1157996).
- [3] L. Tong, M. Mehregany, and L. G. Matus, “Mechanical properties of 3C silicon carbide”, *Applied Physics Letters*, vol. 60, no. 24, p. 2992, 1992. DOI: [10.1063/1.106786](https://doi.org/10.1063/1.106786).
- [4] K. Nakayama, K. Nakatani, S. Khamseh, M. Mori, and K. Maezawa, “Step Hall Measurement of InSb Films Grown on Si(111) Substrate Using InSb Bilayer”, *Japanese Journal of Applied Physics*, vol. 50, 01BF01, Jan. 2011. DOI: [10.1143/JJAP.50.01BF01](https://doi.org/10.1143/JJAP.50.01BF01).
- [5] S. Morozov, K. Novoselov, M. Katsnelson, F. Schedin, D. Elias, J. Jaszczak, and A. Geim, “Giant Intrinsic Carrier Mobilities in Graphene and Its Bilayer”, *Physical Review Letters*, vol. 100, no. 1, pp. 11–14, Jan. 2008. DOI: [10.1103/PhysRevLett.100.016602](https://doi.org/10.1103/PhysRevLett.100.016602).

- [6] A. S. Mayorov, R. V. Gorbachev, S. V. Morozov, L. Britnell, R. Jalil, L. a. Ponomarenko, P. Blake, K. S. Novoselov, K. Watanabe, T. Taniguchi, and a. K. Geim, “Micrometer-scale ballistic transport in encapsulated graphene at room temperature.”, *Nano letters*, vol. 11, no. 6, pp. 2396–9, Jun. 2011. DOI: [10.1021/nl200758b](https://doi.org/10.1021/nl200758b).
- [7] K. Bolotin, K. Sikes, Z. Jiang, M. Klima, G. Fudenberg, J. Hone, P. Kim, and H. Stormer, “Ultrahigh electron mobility in suspended graphene”, *Solid State Communications*, vol. 146, no. 9-10, pp. 351–355, 2008.
- [8] E. V. Castro, H. Ochoa, M. I. Katsnelson, R. V. Gorbachev, D. C. Elias, K. S. Novoselov, a. K. Geim, and F. Guinea, “Limits on Charge Carrier Mobility in Suspended Graphene due to Flexural Phonons”, *Physical Review Letters*, vol. 105, no. 26, p. 266 601, Dec. 2010. DOI: [10.1103/PhysRevLett.105.266601](https://doi.org/10.1103/PhysRevLett.105.266601).
- [9] V. Umansky, M. Heiblum, Y. Levinson, J. Smet, J. Nübler, and M. Dolev, “MBE growth of ultra-low disorder 2DEG with mobility exceeding  $35 \times 10^6 \text{cm}^2/\text{Vs}$ ”, *Journal of Crystal Growth*, vol. 311, no. 7, pp. 1658–1661, Mar. 2009. DOI: [10.1016/j.jcrysgro.2008.09.151](https://doi.org/10.1016/j.jcrysgro.2008.09.151).
- [10] I. Meric, C. Dean, A. Young, J. Hone, P. Kim, and K. L. Shepard, “Graphene field-effect transistors based on boron nitride gate dielectrics”, in *2010 International Electron Devices Meeting*, IEEE, Dec. 2010, pp. 23.2.1–23.2.4. DOI: [10.1109/IEDM.2010.5703419](https://doi.org/10.1109/IEDM.2010.5703419).
- [11] D. K. Ferry, “Transport in graphene on BN and SiC”, in *2012 12th IEEE International Conference on Nanotechnology (IEEE-NANO)*, IEEE, Aug. 2012, pp. 1–5. DOI: [10.1109/NANO.2012.6322126](https://doi.org/10.1109/NANO.2012.6322126).
- [12] J. Moser, A. Barreiro, and A. Bachtold, “Current-induced cleaning of graphene”, *Applied Physics Letters*, vol. 91, no. 16, p. 163 513, 2007. DOI: [10.1063/1.2789673](https://doi.org/10.1063/1.2789673). arXiv: [0709.0607v1](https://arxiv.org/abs/0709.0607v1).
- [13] A. a. Balandin, “Thermal properties of graphene and nanostructured carbon materials.”, *Nature materials*, vol. 10, no. 8, pp. 569–81, Aug. 2011. DOI: [10.1038/nmat3064](https://doi.org/10.1038/nmat3064).
- [14] R. R. Nair, P. Blake, a. N. Grigorenko, K. S. Novoselov, T. J. Booth, T. Stauber, N. M. R. Peres, and a. K. Geim, “Fine structure constant defines visual transparency of graphene.”, *Science (New York, N.Y.)*, vol. 320, no. 5881, p. 1308, Jun. 2008. DOI: [10.1126/science.1156965](https://doi.org/10.1126/science.1156965).
- [15] T. Kobayashi, M. Bando, N. Kimura, K. Shimizu, K. Kadono, N. Umezue, K. Miyahara, S. Hayazaki, S. Nagai, Y. Mizuguchi, Y. Murakami, and D. Hobaru, “Production of a 100-m-long high-quality graphene transparent conductive film by roll-to-roll chemical vapor deposition and transfer process”, *Applied Physics Letters*, vol. 102, no. 2, p. 023 112, 2013. DOI: [10.1063/1.4776707](https://doi.org/10.1063/1.4776707).
- [16] G. Moddel, Z. Zhu, S. Grover, and S. Joshi, “Ultrahigh speed graphene diode with reversible polarity”, *Solid State Communications*, vol. 152, no. 19, pp. 1842–1845, Oct. 2012. DOI: [10.1016/j.ssc.2012.06.013](https://doi.org/10.1016/j.ssc.2012.06.013).

## Chapter 2

# Literature Review

In this chapter some fundamentals on graphene technology and physics will be presented. The current state of the art in graphene DC and RF modeling will be reviewed, as well as some recent studies on the graphene/metal contact. Those subjects will be elemental parts of a larger concept: a graphene universal model, from DC to RF that includes metal contact parasitics.

### 2.1 Graphene Technology

Graphene can be obtained from various sources achieving different levels of quantity and quality. Moreover, each source allows for different processes, devices and finally applications that can be targeted.

#### 2.1.1 Graphene Isolation and synthesis

The first report on the isolation of graphene was published in 2004 in a seminal paper from K. Novoselov and A. Geim [1]. Their simple but very effective method of the scotch-tape, associated with the optical identification on 285 nm SiO<sub>2</sub> substrates, gave virtually anybody access to a breakthrough research subject as graphene, without the need of important resources to acquire and process the material. Although the circumstances are now changed, for the first few years the mechanical exfoliation of graphene was the preferred method to get sparse, small but high-quality graphene flakes. The graphite source can be natural or artificial (HOPG or Kish). The flake size achievable would rarely be larger than 100  $\mu\text{m}$ , with the exception of those sold by commercial firms like Graphene Industries that can reach one millimeter in length. This is anyway a very small value compared to artificially grown graphenes, making its price very high.



Moreover, these flakes are sparsely distributed over the wafer and it's a very human-intensive operation to look for them. This prevents the fabrication of a batch of devices on the same wafer, limiting strongly the number of devices that can be fabricated within reasonable time and resources. The flake is a continuous region of one or few layers of graphene. The relatively low density of defects within the crystallites and their large size in exfoliated graphene compared to other graphene forms, like CVD graphene, are the origin of its high quality in terms of electron mobility, with mobility values typically around  $2 \times 10^4 \text{ cm}^2\text{V}^{-1}\text{s}^{-1}$  on  $\text{SiO}_2$  substrates, while values of  $2.5 \times 10^5 \text{ cm}^2\text{V}^{-1}\text{s}^{-1}$  have been reached at room temperature on hexagonal-BN (h-BN) substrates [2]. Similar values have been obtained for suspended exfoliated graphene [3], eliminating all substrate interaction, but the high complexity of such a technology hinders any realistic application. Easy access and high quality made this graphene source the most preferred for lab research and small-number prototype fabrication.

Graphene from SiC decomposition is a high-quality graphene source discovered from the group of W. de Heer [4]. It is based on the thermal decomposition of SiC by Si sublimation and the segregation of C atoms on graphitic layers; in early reports is also called epitaxially grown graphene. The C segregation can happen on both the faces of the wafer: the (0001) and the (000 $\bar{1}$ ) one, respectively the Si-face and the C-face. Typical temperatures and pressures are 1600° and 100 mbar for Si-face and 1450° and  $1e^{-4}$  mbar for C-face, both in argon atmosphere [5]. This thermal process results in the formation of few-layer graphene on the Si-face and of a thicker graphene stack on the C-face, although in some cases high-quality graphene monolayer have been obtained on the C-face too [6]. Because of the Si desorption the surface of SiC forms narrow terraces of graphene a few micrometers wide, connected by steps with higher electrical resistance. This type of graphene allows for both batch processing and high quality samples, but has the inconvenient of the very high cost of the pristine SiC wafers and their small size compared to those normally used in electronic industry. Moreover, SiC is a very hard and difficult to process material. A bandgap around 260 meV is associated with few-layer graphene on SiC; this value appear to depend inversely on the sample thickness and should reach zero for four layers [7], suggesting some interaction from the underlying substrate. Other reports correlate the bandgap to the strain induced by the substrate [8]. Anyhow, its value is too small to allow for the complete switch-off of the transistor [9]. The electron mobility reaches  $3.0 \times 10^4 \text{ cm}^2\text{V}^{-1}\text{s}^{-1}$  [10], although it depends on the alignment of the direction of transport with substrate terraces [11]. SiC graphene is then a high-cost, high-performance material for batch fabrication of devices, though only for niche applications like high-frequency electronics.

Chemical Vapor Deposition (CVD) of polycrystalline graphene is based on the decomposition at 1000° of a carbon precursor (methane or ethanol) and segregation of carbon

atoms on a foil of catalyst, a transition metal with low solubility for carbon (in most cases Cu) with a very smooth surface [12]. In order to be used, graphene must be separated by the catalyst: a transfer polymer (typically PMMA) is spun on graphene to provide an alternative substrate, the catalyst is etched away and graphene can then be placed on any substrate desired; in some reports graphene is simply peeled off the metal with a PDMS polymer allowing for the reuse of the catalyst [13], but the mechanical stress of the peeling can break the graphene, especially in manual operation. Roll-to-roll production has been demonstrated by Samsung in 2010 with the fabrication of a 30-inch graphene foil [14], and recently industrial-grade continuous production has been performed by Sony, yielding a 100 m long monolayer graphene foil [15], revealing evident interest from both industrial groups in developing transparent and flexible electronics. Large continuous areas of graphene can be synthesized, but unfortunately the crystallite size is rather small and the quality depends strongly on the roughness of the catalyst metal. Mobility values of 0.5 and  $2 \text{ m}^2\text{V}^{-1}\text{s}^{-1}$  can be obtained respectively on  $\text{SiO}_2$  and h-BN substrates. Finally, the transfer step exposing graphene to PMMA or other polymers pollutes its surface with polymer residues, affecting its electron mobility and surface charge [16]. To date this technique, although cheaper than SiC decomposition, still bares high costs because of energy consumption and the production of a smooth Cu foil to be etched off. The optimization of the process can offer a cheap way to large-scale production of graphene for photonics and displays applications.

Liquid-phase suspensions of graphene can be obtained through the exfoliation of graphite in non-aqueous solvents [17] or water-based surfactants [18]. The surface tension of these solvents favors an increase in the total area of the graphite material, making it to split in thinner platelets. Particle size is typically below  $1 \mu\text{m}$ . Another way to obtain a liquid-phase graphitic material is to oxidize graphite to obtain graphene oxide, which is easily soluble in water. It can be deposited as an ink and ultrasound sonication allows its thinning down to monolayer. However, it must be reduced by thermal treatment to obtain graphene, although a complete reduction of all oxide is hardly achievable [19]. Laser scribing allows selective reduction of graphene oxide and allows the interesting possibility to pattern Reduced Graphene Oxide (RGO) without the use of lithography [20]. Graphene and RGO solutions provide low-quality but very low cost techniques. This makes them attractive for applications like printed and flexible electronics, electromagnetic shielding and supercapacitors.

In Fig. 2.1 a comparison between cost and quality of the type of graphene is shown. In conclusion, depending on the application targeted it's possible to select the most appropriate type of graphene, choosing upon the desired cost, performance and adaptability.

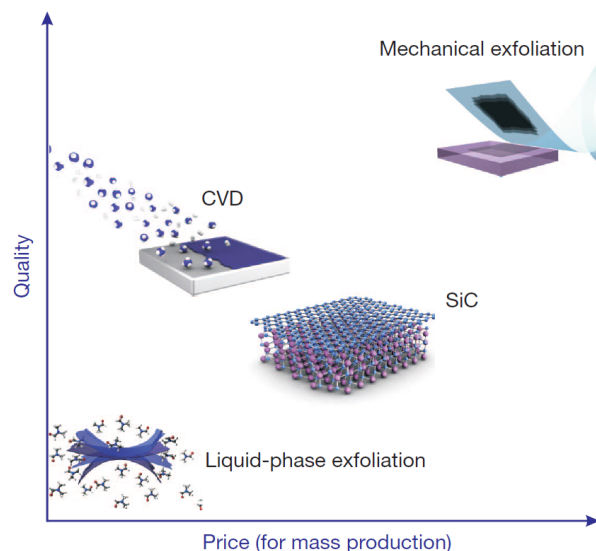


FIGURE 2.1: Quality vs. Cost for graphene production. Adapted from [21].

## 2.2 Graphene Physics

The theoretical investigations on the band structure of graphene started in 1947 with the work of Wallace [22]. At the time perfectly 2D crystals were considered unstable at any physical temperature [23], and graphene was just considered as a building block for graphite. The interest on the detailed physical properties came indeed from this latter material, as it was used a few years earlier by Enrico Fermi as a neutron moderator in the first nuclear pile. A quantum model of the electronic properties of monolayer graphene was then necessary, and was later enriched by the Slonczewski-Weiss-McClure (SWM) band structure of graphite [24],[25], derived within the tight-binding description up to the second-nearest neighbor hopping term. A more detailed and updated formulation can be found in [26]. Semi-classical physics have been used as the bare minimum to understand the origin of graphene's physical properties. A full-quantum description of graphene, including Dirac fermions, spinors and Pauli matrices, although fascinating is unfortunately out of scope for this manuscript, as well as the treatment of the effects of magnetic fields. A more detailed explanation can be found in [27].

### 2.2.1 Electronic Bandstructure

The six atoms in the hexagonal honeycomb structure can be thought as a triangular lattice with a basis of two atoms per unit cell, residing respectively in the two equivalent lattice sites  $A$  and  $B$ . The two lattice vectors are  $\mathbf{A}_0 = (a/2)(3, \sqrt{3})$  and  $\mathbf{B}_0 = (a/2)(3, -\sqrt{3})$ , where  $a \approx 0.142$  nm is the carbon-carbon distance. In

momentum space the first Brillouin zone is delimited by the two inequivalent points  $\mathbf{K} = (2\pi/3a, 2\pi/(3\sqrt{3}a))$  and  $\mathbf{K}' = (2\pi/3a, -2\pi/(3\sqrt{3}a))$ . These corners are called Dirac points and the physics of electron and hole carriers in the close vicinity of those points is of particular importance. The electronic band dispersion obtained for the conduction ( $\pi^*$ ) and the valence ( $\pi$ ) bands, a low-energy approximation zeroing the second-nearest neighbor hopping term, is usually written as follows:

$$E_{\pm}(q) = \pm\hbar v_F q + \mathcal{O}(q/k)^2, \quad (2.1)$$

where  $\mathbf{q}$  is the translation of the momentum vector  $\mathbf{k}$  at one Dirac point and its modulus is small ( $q = |\mathbf{q}| \ll 2\pi/a$ ). This bandstructure has two remarkable properties: first, at the Dirac points ( $q = 0$ ) the conduction and valence band touch each other and intersect, leaving no energy gap. This qualifies graphene as a zero band-gap semiconductor or, as it is also called, a semi-metal. Second, the energy dispersion is linear with momentum, resulting in a carrier group velocity constant over energy ( $v_g \simeq v_F$ , where  $v_F \approx 1e^8 \text{ ms}^{-1}$  is the Fermi velocity); moreover, the effective mass is directly proportional to momentum and zeroes at zero energy [28]. This is a very different behavior than common semiconductors, whose dispersion has a parabolic shape and carrier velocity is function of the second derivative of the dispersion.

The density of states (DOS) is linear too; its value is zero at thermal equilibrium ( $E = 0$ ) and 0 K. Each point  $\mathbf{q}$  is twofold spin degenerate (indicated with  $g_s = 2$ ) and, because of the two inequivalent Dirac points  $\mathbf{K}$  and  $\mathbf{K}'$ , also called valleys, is also twofold valley degenerate ( $g_v = 2$ ). The DOS then reads as follows [29]:

$$\rho_{gr}(E) = \frac{g_s g_v}{2\pi(\hbar v_F)^2} |E|. \quad (2.2)$$

At non-zero temperature, the energy integral of the DOS times the Fermi-Dirac distribution results always in a non negligible electron sheet density. Moreover, graphene is not perfectly planar and presents some corrugation on its surface (ripples), that however are the reason for which it can exist at non-zero temperatures without crumbling or decomposing [30]. This should induce charge inhomogeneities in neutral graphene, i.e. electron and hole puddles that increase the graphene conductivity at zero energy.

### 2.2.2 Consequences of the absence of bandgap

The most striking consequence of the lack of a bandgap is that *a device made of graphene cannot stop the current flow*. One of the most important achievements of Si CMOS technology, along with the ideal signal reconstruction, is the possibility to completely switch off the logic element to reduce the power consumption of the IC. A bandgap at

least comprised between 400 and 500 meV should be necessary for digital logic operation [9], [31]. Recently, the importance of a transport gap has also been stated for RF transistors [32], where devices don't switch off completely but a high output resistance  $r_0$ , i.e. saturation behavior, is necessary to obtain a high intrinsic gain  $G_{int} = g_m r_0$  [9]. Graphene FETs provide very high transconductance, but the lack of a well-defined saturation region reduces heavily the advantage of a graphene power amplifier.

A few methods exist to open a gap in the bandstructure of graphene, while some device concepts other than the conventional FET allowed for a remarkable  $I_{ON}/I_{OFF}$  ratio. The first, perhaps most obvious, way to create a bandgap is to localize the electronic wavefunction by reducing the lateral size of the Graphene Nanoribbon (GNR), down to a few nanometers or tens of nanometers, obtaining a quasi-1D structure. The small DOS and the reduced dimensions of the GNR nanotransistor enhanced ballistic quantum transport, making graphene competitive with carbon nanotubes and III-V HEMTs. GNRs are very similar to carbon nanotubes, with the difference that a CNT has periodic boundary conditions. The confinement gap typically scales as the reciprocal of the width ( $1/W$ ), depending on the crystallographic direction, i.e. the edge [33]: conversely to CNTs, zigzag GNRs are always metallic while armchair GNRs result in three families, two of which semiconducting and one metallic, depending on the width. The inverse proportionality of the bandgap with the width has been validated experimentally with values reaching 300 meV for ribbons smaller than 30 nm, but without any decisive evidence of a dependence on crystallographic direction [34]. Moreover, defective edges and charge puddles alter the transport properties of the nanoribbon, eventually fragmenting it in a collection of quantum dots, making the transport gap to include conductance peaks instead of a homogeneous switch-off behavior [35]–[37]. Edge disorder also perturbs heavily the mobility, which is the main advantage of graphene over Si [38]. However, the need for a saturating behavior has pushed researchers to pattern graphene in reduced-width strips in high-frequency mixers [39] and amplifiers [40]. Ribbons of 100 nm in the first case and 50 nm in the second one allowed to increase the  $I_{ON}/I_{OFF}$  ratio and to improve RF Figures of Merit (FOM) as  $f_{max}$ .

A particular kind of bilayer graphene (BLG), the Bernal stacked one, has the interesting property of creating a small gap between the parabolic conduction and valence bands (sometimes referred to as a “Mexican hat”) when a vertical electric field is applied. In Bernal stacked graphene, half of the carbon atoms are placed above the center of the underlying hexagon, and half above the corners, i.e. above C atoms. Unfortunately Bernal BLG is mostly obtained by mechanical exfoliation, which is a costly and human-intensive task. The number of studies available in literature of direct growth of Bernal BLG is also very limited [41], [42]. In addition, the working principle is more complicated and to create a vertical electric field two gate electrodes are necessary. Achievable

bandgaps are quite limited, with experimental values of 130 meV and  $I_{ON}/I_{OFF}$  ratios of 100 at RT [43].

An alternative, more exotic, configuration is the Vertical Graphene Transistor based on the tunnel current through a thin dielectric between a graphene layer and another electrode. A device with a graphene layer as second electrode has been presented in 2012, where in addition to the tunnel stack a third isolated gate is present (a doped Si wafer and its surface oxide) which allowed for the triode modulation of the tunnel current [44]. An  $I_{ON}/I_{OFF}$  ratio of 50 has been achieved. No RF operation has been demonstrated yet.

A variant of this configuration is the graphene hot-electron transistor, which is actually a graphene implementation of the hot-electron metal-insulator-metal-insulator-metal (M-I-M-I-M) transistor, a concept close to the BJT. Graphene is used as a low resistivity and extremely thin base electrode of a device composed by an emitter-base tunnel junction and a base-collector filtering dielectric (a relatively thick Alumina layer). This operation principle has been explored independently by two labs, and interesting  $I_{ON}/I_{OFF}$  ratios of  $10^5$  have been achieved [45], [46]. Unfortunately, present-day literature has not yet recognized the main problem involved by such devices, which is the same that plagued in the first place the concept of a M-I-M-I-M tunnel transistor: an extremely low current gain, which resulted in collector currents 10 orders of magnitude smaller than those simulated with NEGF models [47].

## 2.3 Graphene FET models

As stated in § 2.2, full-quantum models like Tight-Binding (TB) [26] and Density-Functional Theory (DFT) [48] calculations were the first to be developed for graphene. When graphene was experimentally discovered in 2004, they were the first tool used for the investigation of its properties. However, their computational cost depends on the number of atoms of the material piece to be modeled, thus its use is limited to extremely small surfaces (or volumes). This fact influenced the kind of devices which theoretical researchers were first interested to. GNRs are structures of very limited surface and considerable bandgap. They were the motivation for the highly envisaged “graphenium-inside” computer processor [49], in the sense that it was a research subject that offered exciting performances derived directly from a quantum effect like ballistic transport [50]–[53]. In addition, semiclassical ballistic models were applied to GNR-FET [54]–[57]. However, the validation of GNR models versus device measurement is more complicated due to the technological difficulties in realizing defect-free ribbon edges, so

it was mainly done against TB models. The development of an empirical model of the GNR-FET has been largely inhibited for the same reason.

On the other hand, empirical characterization of graphene was done on micrometer-sized devices, therefore transistors based on large-area graphene (GFET). For that range of dimensions, the main electronic transport mechanism is drift-diffusion and, due to its larger dimensions compared to GNR-FET, the simulation of its behavior was hardly achievable with full-quantum models. Semiclassical modeling was instead a more appropriate tool for the analysis of its characteristics, and existing physical and semi-empirical models [58], [59] for semiconductors were adapted to graphene [60], [61]. The comparison of those models to device measurement is easily achievable and strengthens the reliability and the accuracy of those approaches. In this work, large-area graphene transistors will be simply referred as GFET. Moreover, the aim of this work is to model single-layer graphene devices, whereas few-layer devices will be considered as out of scope.

### 2.3.1 Physical models

Quantum models are numerical tools in which the set of quantum mechanics equations are discretized and evaluated for each atom of the entire device. Those models allow for the computation of the drain current in the ballistic limit through Tight Binding (TB) theory for all drain and gate biases. The TB problem is solved using Non-Equilibrium Greens Functions (NEGF) formalism [52], [62], [63] or the scattering matrix approach [64], [65].

The TB simulation of the device is done in a number of steps, here briefly reviewed: the Dirac Hamiltonian is discretized using the Finite Difference (FD) method; the  $N \times N$  FD matrix, where  $N$  is the number of atoms in the channel, is constructed using the values of the overlap integrals computed through finer models as DFT; the solution for the eigenvalues of the matrix gives the bandstructure of the channel, from which the number of transmitting modes is extracted for the specified gate and drain bias; finally the Landauer equation is applied to each mode, yielding the net current of the device. The overall computational cost of TB methods, already elevated, scales as  $N^2$  and is not suitable for compact modeling in circuit simulators. The band structure produced by those models is generally compared for validation with DFT simulations. Large-area short-channel graphene has also been simulated, although in the ballistic transport limit [63].

Semiclassical ballistic models for GNR-FET simulation are simplified approaches that avoid the Hamiltonian discretization step typical of TB models; they instead derive the bandstructure using either analytical equations or off-line TB-computed values. They

include a number of approaches, both semi-analytical and analytical ones. A type of semiclassical semi-analytical nanotransistor model can be found in [54], [66]; it is the adaptation to GNR of the MOS nanotransistor Top-of-the-barrier model [67]. In this theoretical framework the conduction relies on transmission modes, each allowing a quantized amount of current through the Landauer equation [68] for ballistic transport. The net number of transmitting modes is the result of the balance of two injected electron fluxes, one from source and one from drain [69]. The channel potential determines which modes are able to transmit by changing the alignment of the energy state distribution to the Fermi energy. The electrostatic problem for the channel is simplified into the solution of a single non-linear system of equations, which is solved iteratively by successive approximations. Finally the current is evaluated for transmitting modes through the Landauer equation for ballistic transport. The model operation will be discussed in greater detail in 3. Analytical implementations of this type of model, which employ only closed-form equations for the computation of the channel potential, has also been presented [70], [71]. In conclusion, Top-of-the-barrier models allow for the simulation of the ballistic conduction phenomenon, which is a quantum effect and is significant for GNR-FET, without the use of extensively numerical tools and taking into account a simplified picture for device electrostatics. The drift-diffusion conduction mechanism is not considered here, neither is any scattering mechanism. Being ideal ballistic conduction the theoretical limit to which nanoscaled devices tend, there doesn't exist yet any measurable device that can be fabricated to validate those models.

A more complicate semiclassical analytical model for single layer and BLG nanoribbon transistor simulation is shown in [57], with the implementation of a scattering mechanism in [72]. It is based on the Boltzmann Transport Equation for the electron transport and represents the channel potential in the weak nonlocality approximation formalism; this allows expressing the channel potential in an analytical form. The model is then evaluated to various limiting cases corresponding to the amount of charge induced in the channel by the top-gate electrode. This model allows relating analytically the current and the transconductance with geometrical dimensions of the device. However, the validation is an issue even for this work, which does not present any comparison to finer models or measurements.

Semiclassical approaches have been applied also to large-area graphene FET devices. Although they are all based upon the drift-diffusion transport equations, they can be categorized from semi-analytical to purely analytical approaches. The existence of a large number of GFET device measurements in literature enables the validation of these models.



A type of semiclassical semi-analytical for GFET is shown in refs. [60], [73], [74]. In those works a numerical approach for the computation of the channel electrostatics is employed: the channel length dimension is discretized in a vector of points; the self-potential of channel carriers and the quantum capacitance effects are then iteratively evaluated for each point. The resulting potential profile is used to find the longitudinal electric field and the current using the drift-diffusion transport equation. Another semi-analytical approach derives a closed-form expression to account for quantum capacitance [75]; on the other hand, it uses an iterative method to solve for the internal bias of the intrinsic transistor. Finally, purely analytical models don't use iterative methods at all [76], [77], but it's not clear whether they take into account the contribution of external drain and source resistance as [75] does. Those models are well suited for the simulation of long-channel GFET devices, and include short-channel effects through the empirical account for saturation velocity. In this way they can take into account a limited amount of ballistic transport in a more general drift-diffusion picture. However, the case of the nanotransistor where nearly the entirety of transport is sustained by quantum effects cannot be correctly taken into account. The validation of those models is generally done versus measurements, except for the work presented in [76], [77]. Their accuracy together with the small computational load makes those models suitable for compact modeling in circuit simulators. An example of such a possibility is given by the implementation in VHDL-AMS and SPICE language of a semi-analytical drift-diffusion model as shown in [78], [79].

### 2.3.2 Empirical models

Empirical models are less devoted to the understanding of the physics involved in the device operation, while they are more suitable for the reproduction of the measurements of a small class of devices, typically brought together for similar geometrical dimensions and materials used. Those models generally contain a greater number of parameters that don't have any physical meaning. Moreover, they typically use a smaller amount of iterative loops in favor of closed form expressions.

An empirical physics-based compact model is presented in [61]. It extends the virtual-source model originally developed for short-channel Si CMOS [59] to the GFET case. It is similar to the Top-of-the barrier model, with the use of the drift-diffusion theory in the place of the ballistic transport. In this model the operation of the device is divided in three regions, depending on the type of carriers present in the channel: only electrons, only holes or both of them. The charge density is computed empirically, while the current in the intrinsic transistor is computed with the drift-diffusion equation for each region. As in [75], the computation of the current is part of an iterative loop

that ensures its self-consistence with both internal and external (applied) bias. This step is also commonly done by SPICE-like tools as in [80], but in this particular one it must be done inside the model itself to determine the correct operating region. Finally empirical smoothing functions are employed to ensure the continuity of the current up to the first derivative between two regions. The simulated current is then validated versus measurements. This model provides a numerically efficient and accurate compact model of the GFET operation that can be readily implemented in circuit simulators. However, the use of different set of equations for different regions may introduce artifacts in the shape of the transconductance  $g_m$ . Moreover, while its continuity is ensured by the smoothing functions, the continuity of its derivative is not taken into account and can represent an issue of this approach (see section 1.3 in [81]).

In conclusion, it has been shown that the simulation of graphene devices can be approached with different levels of physical detail, starting from full-quantum modeling of graphene nanotransistors to the empirical modeling of large-area graphene transistors. Greater detail is associated to a geometrically smaller domain that can be simulated and in which the assumptions introduced maintain their validity. A model with validity extending from the GNR nanotransistor to the long-channel GFET is not known to date. Moreover, the validation versus measurements should be gauge of quality, that for GFET are available while for nanotransistors are not.

## 2.4 Graphene/metal contact and propagation models

In mono-layer graphene the conduction takes place onto the surface of the material, in the system of  $\pi^*$  electrons and  $\pi$  holes that are located out of the plane. The surface also is in direct contact with metals; thus the electronic conduction properties are deeply influenced by the type and strength of the interaction between metal and graphene. It is then reasonable to say that the contacted graphene behaves as a different material compared to freestanding graphene. The graphene under the metal together with the layers of the metal with which it interacts is called a graphene-metal complex. The modeling of its specific physical and electrical properties is addressed by means of physical-chemical modeling and empirical modeling.

The most relevant electrical parameter is the contact resistance  $R_C$ . The regions that are adjacent to the contact are also chemically and electrically affected by the metal. Those regions contribute as well to the overall resistance of the device because of altered amount and type of carriers they contain. In this work the *access resistance* in a typical graphene device will be referred as the total resistance between the bulk of the metal and the contact-independent graphene. In the specific case of a FET, this latter region

TABLE 2.1: Contact Resistance at Room Temperature.

Ref.	Metal stack	$R_C$ [ $\Omega \cdot \mu\text{m}$ ]
[85]	Pd/Au	230 $\div$ 900
[85]	Ti/Au	430 $\div$ 900
[86]	thin Cr/Pd	350 $\div$ 750
[87]	Ni	> 500
[88]	Ti/Pd/Au	525 (top)
[89]	Clean Au	95 $\div$ 128
[90]	Ti	20 $\div$ 80

TABLE 2.2: Contact Resistance at Low Temperature.

Ref.	Metal stack	$R_C$ [ $\Omega \cdot \mu\text{m}$ ]	T
[85]	Pd/Au	110 $\div$ 470	6 K
[91]	Ti/Au	> 800	0.25 K
[92]	Cu	135	4 K

will be the one controlled by the gate electrode alone. The contact resistance will be defined instead as the resistance between metal and graphene directly underneath. The case of a device too short to show a contact-independent region will not be considered.

The contact resistance is a parasitic that inhibits the performance of a device, in particular the transconductance [82]. The extrinsic transconductance is obtained by the derivative  $\delta I_D / \delta V_G$  measured on the external device terminals; it is related to the intrinsic one as follows:

$$g_{m,x} = \frac{g_m}{1 + R_S g_m} \quad (2.3)$$

where  $R_S$  is the source access resistance (which contains the contact resistance term). The International Technology Roadmap for Semiconductors has selected the contact resistance as one of the target parameters to be minimized for graphene to be employed in semiconductor industry. A target value of  $1e-8 \Omega \cdot \text{cm}^{-2}$  has been proposed [83]. For MOSFET technology instead it is  $80 \Omega \cdot \mu\text{m}$  per contact, which is about the 10% of the transistor's on-resistance  $V_{DD} / I_{ON}$  [84]. In Tables 2.1 and 2.2 a summary of values of  $R_C$  from recent studies is collected.

#### 2.4.1 Physical and Chemical models of the contact

Metal-graphene contact is a very active subject of current study, and the physical mechanisms behind it are not completely understood. Advances in the modeling of the contact were motivated by new phenomena, introduced by new experiments and that it was necessary to account for.

In the first graphene transistors an asymmetry in the electron and hole branches of the V-shaped  $I_D(V_G)$  was shown. It was first noticed by [93] and was later explained experimentally by the presence of doping: along with the shift of the minimum conductivity point (i.e. Dirac point) in the  $V_G$  axis, the slope of the left branch increased for p-type doping, and conversely on the right branch for n-type doping [94]. A photocurrent study confirmed the presence of p-n junctions in the region adjacent the metal contacts, suggesting the possibility that doping was induced by the metals that contacted graphene [95]. P-n junctions within the channel are expected to increase the access resistance of a FET device [96], i.e. the resistance between the metal contact and gate-controlled region of the FET channel. The presence of a metal-doped region was explained by chemical models for complexes made of graphene and various metals within the density functional theory (DFT) [97], [98]. This is a quantitative technique of computational chemistry to obtain ground-state electronic properties of many-body systems, in particular atoms and molecules; more details are contained in [99].

DFT was used to study the band-structure of graphene-metal complexes, along with their work function and bonding energy for various metals. Those studies allowed distinguishing two categories of complexes upon the strength of the metal-graphene binding: *physisorbed* graphene, where graphene's band-structure is mostly preserved; and *chemisorbed* graphene, where the contact is more intimate and the band-structure of the complex is something different from both metal and graphene. Chemisorbed metals can provide better mechanical stability and electrical connection than physisorbed ones [97]. However, for the purpose of an equivalent circuit of contacted graphene, in this manuscript there will be no distinction between chemisorbed and physisorbed metals.

The formation of the graphene-metal complex is conceptually divided in four steps in Fig.2.2. In (a) the clean metal and intrinsic graphene are separated. The different magnitude of their work functions induces doping in graphene when the vacuum potential of the materials gets aligned (b). The common Fermi level is pinned to the metal's one and graphene's band structure is shifted (towards higher energies in this case), creating a doping potential  $\Delta E_F'$ .

However, a strong Pauli-exclusion interaction occurs between the metals' inner orbitals (s-electrons) and graphene  $\pi$ -electrons. It repels electrons from the metal-graphene interface and significantly shifts down graphene's energy levels, leaving unaltered the metal's ones because of the large difference in amount of states between the two materials [100]. The depletion in electrons at the interface leads to the formation of an electric dipole, influencing the magnitude and eventually the sign of the doping. The potential generated by the dipole, marked in [98] as a quantity  $\Delta_c$ , adds up with the previous potential difference value and gives  $\Delta E_{F'} = \Delta E_{F''} - \Delta_c$ , as seen in Fig.2.2(c). In [98] is

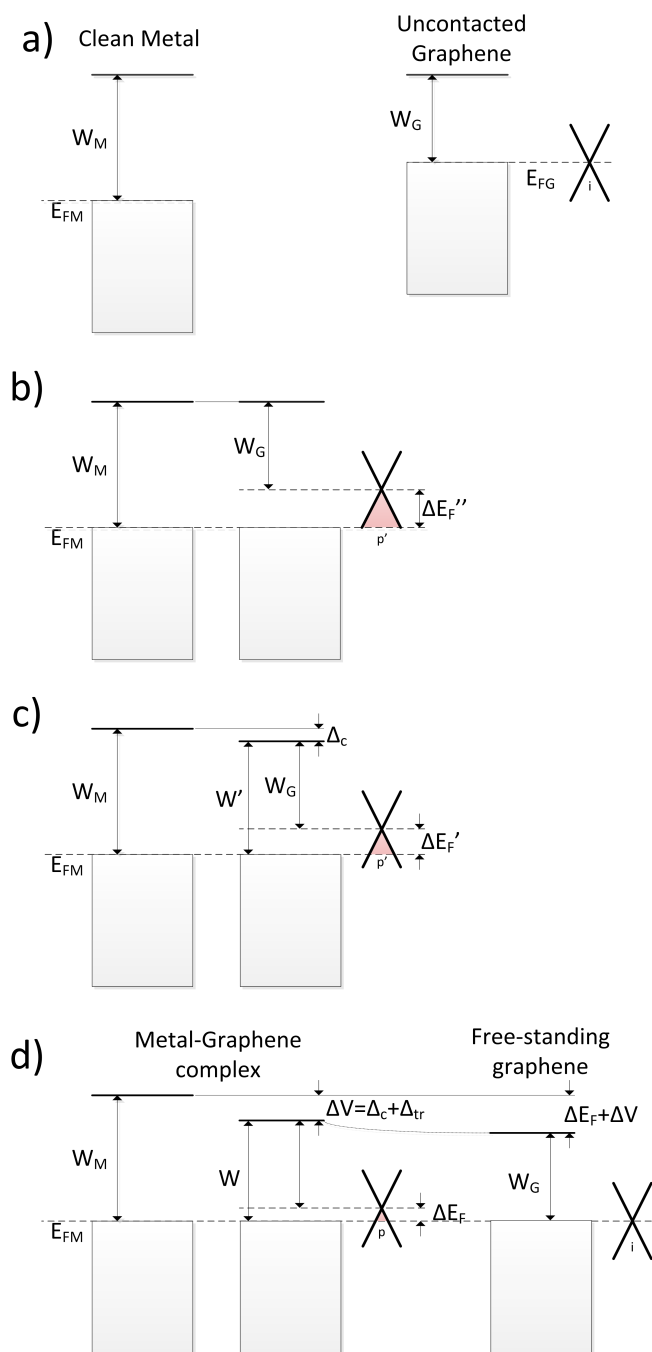


FIGURE 2.2: The Work functions of metal and Graphene, in successive steps: non in contact (a); alignment of vacuum potentials and initial graphene doping (b); the formation of the Pauli repulsion potential  $\Delta_c$  (c); the charge transfer and further reduction of the potential, up to its zeroing at a distance from the metal when pristine graphene is encountered (d).

proposed that the potential added by this Pauli-interaction dipole should have a value nearly independent from the metal or the systems, so that the doping type and value can be predicted within some limits for metals with known working functions. However, in [100] is stated that this potential value is indeed very sensitive to the filling of the outermost s-orbital of the metal, thus to the metal itself. As a consequence of the doping induction, a charge transfer process happens which mitigates the doping itself.

As matter of fact, not all of the attracted charges can be sustained by graphene for a certain amount of doping. Each elemental charge generates a self-potential, marked in Fig.2.2(d) as  $\Delta_{tr}$ , which acts on the graphene itself and, because of the limited amount of states in graphene, shifts back significantly the Fermi level to values closer to neutrality. It is useful to stress the point that transferred charge, which is generated by the re-equilibration of Gauss law, is substantially different from the charge dipole generated from the Pauli-exclusion interaction. How this latter charge behaves in presence of electric fields is still a matter of study. Transferred charge shifts graphene's energy levels up (n-doped graphene) or down (p-doped graphene), compensating the overall potential of graphene under the metal, then the doping itself. The final value of the doping is  $\Delta E_F$ . In (d) is also shown the region of graphene far from the contact which regains its intrinsic state. The region comprised between those two points is called *charge transfer region* [95].

So, with DFT studies it is possible to identify the origin of doping from adsorbed metals in graphene and predict their value. Based upon DFT calculations, an empirical model of graphene doping from metals has been presented [98]. The results proposed by DFT calculations include a detailed description of many useful physical and electrical parameters. However, those results must be taken carefully because small variations in the structural parameters of the metal's atomic lattice [101] or in the computational method used [102] can yield a difference in graphene doping of several hundreds of meV, and even a change of doping type.

Photocurrent studies have confirmed that the metal-induced doping extends spatially towards uncontacted graphene forming the charge transfer region, creating then a junction with gate-controlled graphene [95]. In Fig.2.3(a) a back-gate FET is shown that, depending on the gate potential, modulates the doping of its charge transfer regions (shaded in green for the case  $V_G = 0$  in (b)), and therefore its access resistance  $R_{S,D}$ .

The first work that focused on the extension of this region was a DFT study of metal-contacted graphene nanoribbons (GNR) [104], whereby the potential of metal-induced doping potential was suppressed after few nanometers from the edge of the contact. Moreover, this study shows that the potential of contacted graphene start a smooth transition towards uncontacted graphene before crossing the metal edge. This is a result

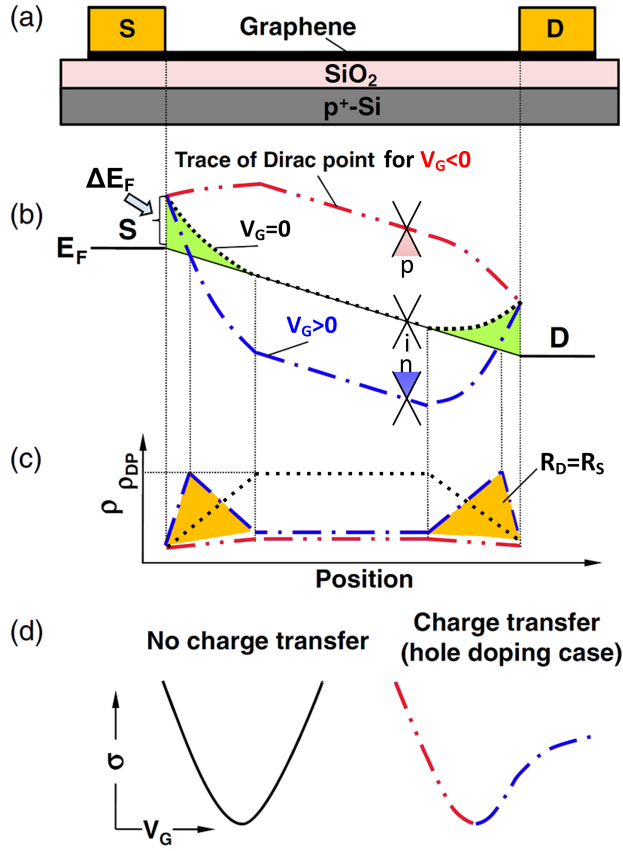


FIGURE 2.3: Potential and resistivity along the channel of a graphene FET. (a) structure of the back-gated FET; (b) Electrostatic potential represented as the trace of the Dirac point of graphene for  $V_G > 0 V$  (blue dash-dotted line),  $V_G = 0 V$  (black dotted line) and  $V_G < 0 V$  (red dash-double-dotted line); (c) Resistivity along the channel for various gate voltages. In yellow the area of the access resistances  $R_S$  and  $R_D$ .  $\rho_{DP}$  is the resistivity at the Dirac point in graphene. Adapted from [103].

that can be found in more recent models (notably [85]) and that will be discussed in greater depth in the last part of this section. However, the fact that the charge-transfer process is neglected and the use of ill-defined boundary conditions, as pointed out by [105], tend to lower the importance of this study.

An analytical model of the charge transfer region and its spatial extension has been proposed in [105]. This model uses the Thomas-Fermi approach to study the band bending caused by metal contacts on undoped, chemically doped and electrically doped (i.e. with a gate electrode) graphene. The extension of the charge transfer region depends on the decay of the electrostatic potential by the charge screening, which strength depends on the doping and on the presence of electrical gating. This screening is generally weak, and makes the potential to decay with the distance from the metal contact as  $x^{-1/2}$  and  $x^{-1}$  for undoped and doped graphene [105]. The predicted charge transfer region is therefore of considerable size. The position of the junction as well as its type (p-n, p'-p, etc.)

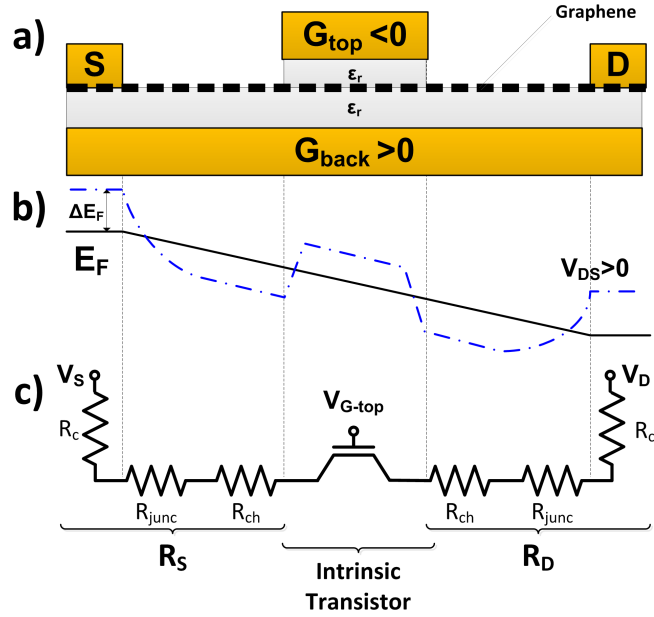


FIGURE 2.4: Access resistance of a double-gate graphene FET. (a) the structure; (b) The Fermi level  $E_F$  (solid black) and the trace of the Dirac point (blue dash-dotted) along the channel; (c) the equivalent circuit of the extrinsic transistor.

depends on the metal-induced doping and gate voltage. This model thus allows for the prediction of the dimension and type of the metal-induced junction, which is responsible for the increase of the access resistance and of the asymmetry of the  $I_D(V_G)$  transfer characteristic in graphene FETs. However its complexity and the lack of a comparison with access resistance measurements make its use difficult. On the other hand, another analytical model [106] proposes to use linear-graded charge transfer regions instead.

In Fig.2.4 a double-gated graphene FET is shown along with its equivalent circuit in (c).  $R_S$  and  $R_D$  are the access resistances; each of them is the series of the contact resistance  $R_C$ , the charge transfer junction resistance  $R_{junc}$  and of the resistance  $R_{ch}$  that comes from the section of the channel not controlled by the top-gate. Self-aligned contacts in top-gated GFETs allow for the minimization of access resistance and for a better electrostatic control of the channel [6], which results in graphene completely covered either by the gate electrode stack or by the contact electrodes. The extension of the charge transfer region should be also minimized. A comparison between a transistor with a partially gated channel and one with self-aligned contacts has been performed in [107]. A better control of the channel through the top gate was found, together with a modulation effect by the back-gate potential on the electron-hole asymmetry in the  $I_D - V_{G,top}$  characteristic. Being the term  $R_{ch}$  minimized by contact auto-alignment, it cannot contribute to the asymmetry modulation; instead, this effect is ascribed to contacted graphene. This means that a modulation of the doping profiles in the graphene



regions underneath the source/drain contacts by the back-gate voltage should be possible. Authors of [107] then claim that the back-gate impacts the alignment of the Fermi level relative to the graphene cone dispersion relation. An electrostatic control of the Fermi level of contacted graphene through the back-gate should be possible, contradicting the thesis that the Fermi level of the graphene-metal complex is firmly pinned to the metal's one. However, it's not clear what would be the effect of the back-gate on the term  $R_{junc}$ , which is neither under the contact nor totally controlled by the top-gate.

An explanation to the back-gate control of the doping of contacted graphene, along with its effect on  $R_{junc}$ , is presented in [108]. In case of weak electronic interaction between metal and graphene (physisorption), graphene's pristine electronic band structure is preserved, and the metal/graphene interfacial layer demonstrates a dielectric-like behavior. The modulation effect is then modeled through an effective thin metal-graphene interfacial dielectric layer, whose capacitance concurs with the much weaker back-gate capacitance to the electrostatic control of the Fermi-level in contacted graphene. The dielectric layer should be thin enough to sustain a tunneling current through it, defining a tunneling contact resistivity across the interface. However, an overall equivalent circuit with both the capacitive and resistive terms of the contact has not been presented by the authors. On the other hand, the transport across the junction is considered ballistic and it is modeled through the Landauer equation of transport in the NEGF formalism. The two terms of the resistance are thought independent and separated, thus the overall access resistance can be calculated as the series of all terms. This approach then allows for the computation of the electron-hole asymmetry effect through the modeling of the impact of back-gate voltage on the doping of the contact. However, it must be noted that this approach does not include any interaction between metal and graphene apart from the electrostatic one, and does not consider any Fermi level pinning; in short, the metal-graphene contact is not considered as a chemical complex. Moreover, the model by construction is not able to extract both the interface capacitance and the metal-induced doping at the same time, therefore it leaves the doping as a free parameter, which could be an issue in this approach.

The effect of the gate on the electronic properties of the contact has been studied in more depth in [100]. Within the frame of DFT simulations used to compute the band structure of physisorbed and chemisorbed graphene, the effect of an externally applied electric field to the complex has been analyzed. DFT simulations have shown that an external electric field can shift graphene's energy-levels up and down relative to the Fermi level, which is pinned by the metal substrate; this allows for the back-gate modulation of graphene's work function and doping [100]. Anyway, it's not clear whether the electric field affects only the alignment of the energy levels or affects also the Pauli-exclusion interaction dipole, i.e. the equilibrium distance between metal and carbon atoms.

A model that combines most of the results from DFT simulations with the geometry of the contact is presented in [85]. Here the transport along the graphene surface underneath the metal is also considered, proposing the concept of a distributed transmission of carriers from graphene to metal. In this model the contact is no more considered as only dependent on the width of the contact; instead, a transport mechanism would be present in contacted graphene also beyond the contact edge, and a contact length dimension would be involved. The transport from free-standing graphene, crossing the p-n junction towards beyond-the-edge contacted graphene is thought as ballistic; in addition to this, another mechanism would be the tunneling transport across the graphene/metal interface. The electric contact is considered to be the result of the concurrency of those two transport mechanisms: the only scattering process suffered by the graphene-graphene transport is the graphene/metal tunneling, and the overall transmittance is treated as the coherent cascade of the two transmittances [108]. The model includes the results of DFT simulations through the empirical model introduced by [98] for the modeling of the doping; this latter is further affected by the back-gate through electrostatic doping. The conductivity of contacted graphene depends on the doping, and so does the transmittance of the graphene-graphene transport. The unit-length contact conductance is finally evaluated using a modified Landauer formula, combining the two transmittances. Anyway, because of its complexity, this model contains a number of free physical parameters that makes its use for real measurement datasets very difficult.

At first a dependence of the contact resistance on length has been argued by [87], supporting only a width dependence of  $R_C$ ; however, those experiments were prone to the minimum feature length of around  $1 \mu\text{m}$  by the technology adopted by the authors. In [85] the residual potential difference between metal and graphene is shown to decrease with distance from the edge, in a similar way as proposed by [104], and should reach zero in few hundreds of nanometers, that is well below the experimental limits of [87]. Finally it has been shown experimentally in [109] that reducing the contact length below  $200 \text{ nm}$  would make the resistance to increase inversely linearly with contact length, thus contradicting the results of [87]. The model proposed in [85] allows relating the metal-induced doping, the electrostatic doping and the geometry of the contact to its resistance. The trend of the dependence of  $R_C$  on length has been therefore confirmed. However more accurate measurements would allow extracting a precise law for this dependence, if any; such kind of law has been extracted for semiconductors already in the '70s, and will be presented in the next section.

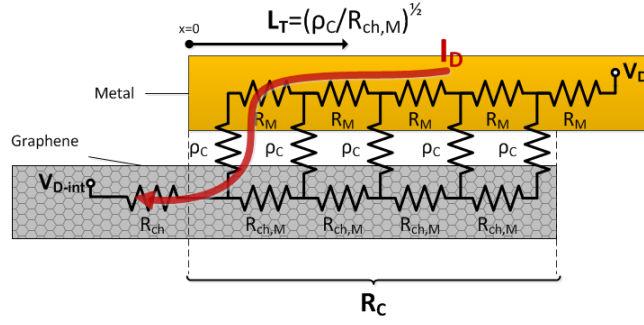


FIGURE 2.5: The Transmission Line Model (TLM) circuit for contact resistance. The current  $I_D$  crowds in a transfer length  $L_T$  neighborhood from the edge of the metal, following the least resistance path.

### 2.4.2 DC models and measurements

When a metal is in contact with another material with a lower conductivity, either a semiconductor or a semimetal, the current naturally flows through the least resistance path and enters the semiconductor only near the edge of the metal. This effect is called *contact current crowding* and it's thoroughly described in the Transmission Line Method (TLM) for planar devices by [110]. Its equivalent circuit is shown in Fig.2.5 for the case of a metal-graphene contact. The units of the quantities in the image are the following: contact resistance  $R_C$  [ $\Omega \cdot \text{mm}$ ], specific interface resistance  $\rho_C$  [ $\Omega \text{mm}^2$ ], metal sheet resistance  $R_M$  and graphene-under-metal sheet resistance  $R_{ch,M}$  [ $\Omega/\square$ ], transfer length  $L_T$  [nm].

In this model the semiconductor sheet thickness is zero, which is a perfectly adequate assumption for graphene, less for traditional semiconductors (see § 3.4 of [111]). So, the current flow is distributed on one-dimension. In horizontal direction there are the sheet resistivities,  $R_M$  for metal and  $R_{ch,M}$  for contacted graphene, and on vertical sections the interface resistivity  $\rho_C$ . For semiconductors the resistivity of the free-standing material is the same of the contacted one. The analytical solution of the model gives an hyperbolic cotangent dependence of  $R_C$  on contact length:

$$R_C(L) = \frac{\rho_C}{L_T} \coth(L/L_T). \quad (2.4)$$

This equation was also confirmed for CNT by measurements of a device in which the contact length was increasingly reduced by FIB and laser ablation [112], [113]. In [87] the sheet resistances of contact and uncontacted graphene are assumed equal in value ( $R_{ch} = R_{ch,M}$ ), but with the result that  $R_C$  is almost independent on length; this brought the authors to deduce that the most of the current crowds at the edge of the contact, mostly because of the great difference in value between  $R_{ch,M}$  and  $R_M$ .

The large difference in resistivity should be further enhanced by the higher scattering that electrons in contacted graphene should suffer, larger than in free-standing graphene; this assumption is supported by an increased signature in the defect-related D band in Raman spectroscopy of graphene through a thin metal film [103]. However, no increased signature of the D band is reported in [114]. Anyway, the TLM picture does not include the resistor  $R_{junc}$  (see Fig.2.3), so it's not clear which role should play the junction in the overall access resistances  $R_S$  and  $R_D$ .

The most used procedure to measure  $R_C$  is the Transfer Length Method (again, abbreviated as TLM) which was originally proposed by Shockley [115]. It has been later refined as the measurement of the resistance of a pairs of devices with unequal contact separation; the contact resistance  $R_C$  is extrapolated by the y-intercept of the R vs. L plot, while the resistivity of the semiconductor is given by the slope of the R-length plot. For short length contact, of the order or less than  $L_T$ , it can yield  $\rho_C$  too. This method is however prone to at least two sources of error: one that comes from the geometry, in which strip width and contact separation variation can induce significant error on the final  $R_C$  [116]. This can be minimized by the exact geometrical characterization of the measured devices, as done in [90]. Moreover, non-uniformities of the electrical parameters can lead to errors in the extracted contact parameters even if there is no error in the measured electrical and geometrical parameters [117]. Finally, metal overlays with high sheet resistances can also alter effective  $R_C$  value [118].

In conclusion, recent physical models had to comply with a larger number of phenomena observed during experiments, notably the metal-induced doping, the charge transfer junction and the dependence of  $R_C$  on geometry. A model that includes all those effects should represent a more thorough understanding of the problem. However, the large number of free physical parameters makes their use in the prediction of the contact properties for new systems and metal-graphene stacks difficult. On the other hand, empirical TLM models would be very useful for the prediction of the contact properties for a given metal-graphene stack.

### 2.4.3 RF measurements and models

The exploration of the conduction properties of graphene have also been performed in RF, with the fabrication of passive structures and the development of simple empirical models. One of the first experiments of this kind was the fabrication of a CPW line loaded with exfoliated graphene [119], [120]. The fabrication of this device was quite challenging because of the reduced dimensions of the graphene flake, around  $20 \times 80 \mu\text{m}$ ; the three electrodes of the CPW line have been designed to fit into the short side of the

flake. EM simulations were performed, assigning a sheet resistance and capacitance to a material and matching the S-parameters, for multiple DC biases. In this way a  $50 \Omega$  shunt resistance was found at some bias point between 1.0 and 2.0 V.

In [121] a very general lumped element model is used in order to extract the contact and conductivity properties for single and few-layers graphene strips. Exfoliated graphene strips of  $10 \times 10 \mu\text{m}$  are placed in series connection between the two central electrodes of an RF access structure; the model is then fitted against measured S-parameters. The model of graphene consist of a bulk resistance  $R$ , capacitance  $C$  and inductance  $L$ , together with contact resistance  $R_C$  and capacitance  $C_C$ . The circuit parameters used therein are however function of frequency. As remarked in [122] for a similar work on CNTs, the system is overdetermined: 5 parameters have to be fitted for each frequency point out of complex transmission and reflection measurements (the device is both reciprocal and symmetric, giving 4 values per data point). Among the other parameters, the inductance  $L$  is here associated to the *kinetic inductance* of graphene: it represents the inertia of ballistic electrons, which travel at Fermi velocity, against alternating longitudinal electric field. The bulk capacitance  $C$  instead is not associated to any physical quantity.

An analogous work has been done for CVD graphene on low-loss fused quartz [123]. Series and shunt connections on a CPW transmission line resulted in a sheet resistance of  $1100 \Omega$ , which was close to the DC value measured ( $1400 \Omega$ ). The contact resistance varied with frequency, indicating the presence of a capacitive effect between metal and graphene, possibly coming from local regions of resist residue. The model was simplified by ignoring the contact parasitics; it was applied only at high frequency, where the  $R_C$  is shorted by the contact capacitance and only the sheet resistance appears. Also the authors of [124] ignored the effect of the contact, but in the other hand the model they used is more complicate. They measured a  $20 \times 20 \mu\text{m}$  graphene strip in series connection up to 40 GHz. Then, they modeled it with a transmission line model, after de-embedding the access fixtures subtracting the correspondent  $\mathbf{Y}$  matrixes. However, the wavelength of a CPW on Si as the one proposed by [124] is much larger than the strip of graphene, whose phase delay should be less than  $3^\circ$  and perhaps too short to justify a transmission line model. The sheet resistance obtained was  $620 \Omega$  for single layer graphene and  $237 \Omega$  for multilayer.

Finally, a few studies analyzed the sheet conductivity of non-contacted graphene samples by immersing them in rectangular waveguides, normal to the wave propagation [125]–[127]. From the analysis of the transmission and reflection of the WG, the obtained sheet conductivities ranged from  $1670$  to  $8941 \Omega$ , while in [128] it was around  $2000 \Omega$  at zero magnetostatic field in a circular waveguide.

## 2.5 Conclusions

The study of the metal/graphene contact and of the high-frequency propagation is treated very differently among the various fields of study. They should be considered as aspects of a same, larger, problem. However, the examinations of contact are carried out only at zero frequency. A few empirical studies consider both aspects, but sometimes with over-simplified models.

On the other hand, in FET modeling the contact parasitic is taken into account. Its effects on high-frequency FOMs are deeply evaluated because of the severe impact on the transconductance and output current. High frequency performances are the main target of these experiments and models, stressing the importance of sub-micrometer scaling to attain even higher performances. And yet, contact parasitics are generally represented by a simple resistance, evaluated in DC and independent in frequency.

In conclusion, the need of a universal model connecting the finer investigation of the physics involved in sub-micrometric FET devices and the high frequency propagation is growing in importance. This work aims to bring near those two fields, putting the basis for their integration in a single domain of study.

## References

- [1] K. S. Novoselov, a. K. Geim, S. V. Morozov, D. Jiang, Y. Zhang, S. V. Dubonos, I. V. Grigorieva, and a. a. Firsov, “Electric field effect in atomically thin carbon films.”, *Science (New York, N.Y.)*, vol. 306, no. 5696, pp. 666–9, Oct. 2004. DOI: [10.1126/science.1102896](https://doi.org/10.1126/science.1102896).
- [2] A. S. Mayorov, R. V. Gorbachev, S. V. Morozov, L. Britnell, R. Jalil, L. a. Ponomarenko, P. Blake, K. S. Novoselov, K. Watanabe, T. Taniguchi, and a. K. Geim, “Micrometer-scale ballistic transport in encapsulated graphene at room temperature.”, *Nano letters*, vol. 11, no. 6, pp. 2396–9, Jun. 2011. DOI: [10.1021/nl200758b](https://doi.org/10.1021/nl200758b).
- [3] K. Bolotin, K. Sikes, Z. Jiang, M. Klima, G. Fudenberg, J. Hone, P. Kim, and H. Stormer, “Ultrahigh electron mobility in suspended graphene”, *Solid State Communications*, vol. 146, no. 9-10, pp. 351–355, 2008.
- [4] C. Berger, Z. Song, X. Li, X. Wu, N. Brown, C. Naud, D. Mayou, T. Li, J. Hass, A. N. Marchenkov, E. H. Conrad, P. N. First, and W. a. de Heer, “Electronic confinement and coherence in patterned epitaxial graphene.”, *Science (New York, N.Y.)*, vol. 312, no. 5777, pp. 1191–6, May 2006. DOI: [10.1126/science.1125925](https://doi.org/10.1126/science.1125925).

- [5] J. A. Robinson, M. Wetherington, J. L. Tedesco, P. M. Campbell, X. Weng, J. Stitt, M. a. Fanton, E. Frantz, D. Snyder, B. L. VanMil, G. G. Jernigan, R. L. Myers-Ward, C. R. Eddy, and D. K. Gaskill, “Correlating Raman spectral signatures with carrier mobility in epitaxial graphene: a guide to achieving high mobility on the wafer scale.”, *Nano letters*, vol. 9, no. 8, pp. 2873–6, Aug. 2009. DOI: [10.1021/nl901073g](https://doi.org/10.1021/nl901073g).
- [6] Z. Guo, R. Dong, P. S. Chakraborty, N. Lourenco, J. Palmer, Y. Hu, M. Ruan, J. Hankinson, J. Kunc, J. D. Cressler, C. Berger, and W. a. de Heer, “Record maximum oscillation frequency in C-face epitaxial graphene transistors.”, *Nano letters*, vol. 13, no. 3, pp. 942–7, Mar. 2013. DOI: [10.1021/nl303587r](https://doi.org/10.1021/nl303587r).
- [7] S. Y. Zhou, G.-H. Gweon, A. V. Fedorov, P. N. First, W. A. de Heer, D.-H. Lee, F. Guinea, A. H. Castro Neto, and A. Lanzara, “Substrate-induced bandgap opening in epitaxial graphene.”, *Nature materials*, vol. 6, no. 10, pp. 770–5, Oct. 2007. DOI: [10.1038/nmat2003](https://doi.org/10.1038/nmat2003). arXiv: [0709.1706](https://arxiv.org/abs/0709.1706).
- [8] N. Ferralis, R. Maboudian, and C. Carraro, “Evidence of structural strain in epitaxial graphene layers on 6H-SiC(0001)”, *Physical Review Letters*, vol. 101, p. 156 801, 2008.
- [9] F. Schwierz, “Graphene Transistors: Status, Prospects, and Problems”, *Proceedings of the IEEE*, vol. 101, no. 7, pp. 1567–1584, Jul. 2013. DOI: [10.1109/JPROC.2013.2257633](https://doi.org/10.1109/JPROC.2013.2257633).
- [10] W. A. de Heer, C. Berger, M. Ruan, M. Sprinkle, X. Li, Y. Hu, B. Zhang, J. Hankinson, and E. Conrad, “Large area and structured epitaxial graphene produced by confinement controlled sublimation of silicon carbide.”, *Proceedings of the National Academy of Sciences of the United States of America*, vol. 108, no. 41, pp. 16 900–5, Oct. 2011. DOI: [10.1073/pnas.1105113108](https://doi.org/10.1073/pnas.1105113108).
- [11] Y. Lin, D. Farmer, and K. Jenkins, “Enhanced Performance in Epitaxial Graphene FETs With Optimized Channel Morphology”, *Electron Device*, vol. 32, no. 10, pp. 1343–1345, 2011.
- [12] X. Li, W. Cai, J. An, S. Kim, J. Nah, D. Yang, R. Piner, A. Velamakanni, I. Jung, E. Tutuc, S. K. Banerjee, L. Colombo, and R. S. Ruoff, “Large-area synthesis of high-quality and uniform graphene films on copper foils.”, *Science (New York, N.Y.)*, vol. 324, no. 5932, pp. 1312–4, Jun. 2009. DOI: [10.1126/science.1171245](https://doi.org/10.1126/science.1171245).
- [13] P. J. Ko, H. Takahashi, S. Koide, H. Sakai, T. V. Thu, H. Okada, and A. Sandhu, “Simple method to transfer graphene from metallic catalytic substrates to flexible surfaces without chemical etching”, *Journal of Physics: Conference Series*, vol. 433, p. 012 002, Apr. 2013. DOI: [10.1088/1742-6596/433/1/012002](https://doi.org/10.1088/1742-6596/433/1/012002).
- [14] S. Bae, H. Kim, Y. Lee, X. Xu, J.-S. Park, Y. Zheng, J. Balakrishnan, T. Lei, H. R. Kim, Y. I. Song, Y.-J. Kim, K. S. Kim, B. Ozyilmaz, J.-H. Ahn, B. H. Hong, and S. Iijima, “Roll-to-roll production of 30-inch graphene films for transparent electrodes.”, *Nature nanotechnology*, vol. 5, no. 8, pp. 574–8, Aug. 2010. DOI: [10.1038/nnano.2010.132](https://doi.org/10.1038/nnano.2010.132).

- 
- [15] T. Kobayashi, M. Bando, N. Kimura, K. Shimizu, K. Kadono, N. Umezū, K. Miyahara, S. Hayazaki, S. Nagai, Y. Mizuguchi, Y. Murakami, and D. Hobara, “Production of a 100-m-long high-quality graphene transparent conductive film by roll-to-roll chemical vapor deposition and transfer process”, *Applied Physics Letters*, vol. 102, no. 2, p. 023 112, 2013. DOI: [10.1063/1.4776707](https://doi.org/10.1063/1.4776707).
- [16] A. Pirkle, J. Chan, A. Venugopal, D. Hinojos, C. W. Magnuson, S. McDonnell, L. Colombo, E. M. Vogel, R. S. Ruoff, and R. M. Wallace, “The effect of chemical residues on the physical and electrical properties of chemical vapor deposited graphene transferred to SiO<sub>2</sub>”, *Applied Physics Letters*, vol. 99, no. 12, p. 122 108, 2011. DOI: [10.1063/1.3643444](https://doi.org/10.1063/1.3643444).
- [17] Y. Hernandez, V. Nicolosi, M. Lotya, F. M. Blighe, Z. Sun, S. De, I. T. McGovern, B. Holland, M. Byrne, Y. K. Gun’ko, J. J. Boland, P. Niraj, G. Duesberg, S. Krishnamurthy, R. Goodhue, J. Hutchison, V. Scardaci, A. C. Ferrari, and J. N. Coleman, “High-yield production of graphene by liquid-phase exfoliation of graphite.”, *Nature nanotechnology*, vol. 3, no. 9, pp. 563–8, Sep. 2008. DOI: [10.1038/nnano.2008.215](https://doi.org/10.1038/nnano.2008.215).
- [18] A. a. Green and M. C. Hersam, “Solution phase production of graphene with controlled thickness via density differentiation.”, *Nano letters*, vol. 9, no. 12, pp. 4031–6, Dec. 2009. DOI: [10.1021/nl902200b](https://doi.org/10.1021/nl902200b).
- [19] G. Eda, G. Fanchini, and M. Chhowalla, “Large-area ultrathin films of reduced graphene oxide as a transparent and flexible electronic material.”, *Nature nanotechnology*, vol. 3, no. 5, pp. 270–4, May 2008. DOI: [10.1038/nnano.2008.83](https://doi.org/10.1038/nnano.2008.83).
- [20] M. F. El-Kady, V. Strong, S. Dubin, and R. B. Kaner, “Laser scribing of high-performance and flexible graphene-based electrochemical capacitors.”, *Science (New York, N. Y.)*, vol. 335, no. 6074, pp. 1326–30, Mar. 2012. DOI: [10.1126/science.1216744](https://doi.org/10.1126/science.1216744).
- [21] K. S. Novoselov, V. I. Fal’ko, L. Colombo, P. R. Gellert, M. G. Schwab, and K. Kim, “A roadmap for graphene.”, *Nature*, vol. 490, no. 7419, pp. 192–200, Oct. 2012. DOI: [10.1038/nature11458](https://doi.org/10.1038/nature11458).
- [22] P. Wallace, “The Band Theory of Graphite”, *Physical Review*, vol. 71, no. 9, pp. 622–634, May 1947. DOI: [10.1103/PhysRev.71.622](https://doi.org/10.1103/PhysRev.71.622).
- [23] R. E. Peierls, “Quelques proprietes typiques des corps solides”, *Ann. I. H. Poincare*, vol. 5, pp. 177–222, 1935.
- [24] J. McClure, “Band Structure of Graphite and de Haas-van Alphen Effect”, *Physical Review*, vol. 108, no. 3, pp. 612–618, Nov. 1957. DOI: [10.1103/PhysRev.108.612](https://doi.org/10.1103/PhysRev.108.612).
- [25] J. Slonczewski and P. Weiss, “Band Structure of Graphite”, *Physical Review*, vol. 109, no. 2, pp. 272–279, Jan. 1958. DOI: [10.1103/PhysRev.109.272](https://doi.org/10.1103/PhysRev.109.272).
- [26] S. Reich, J. Maultzsch, C. Thomsen, and P. Ordejón, “Tight-binding description of graphene”, *Physical Review B*, vol. 66, no. 3, p. 035 412, Jul. 2002. DOI: [10.1103/PhysRevB.66.035412](https://doi.org/10.1103/PhysRevB.66.035412).
- [27] A. Castro Neto, F. Guinea, N. Peres, K. Novoselov, and A. Geim, “The electronic properties of graphene”, *Reviews of Modern Physics*, vol. 81, no. 1, pp. 109–162, Jan. 2009. DOI: [10.1103/RevModPhys.81.109](https://doi.org/10.1103/RevModPhys.81.109).



- [28] V. Ariel and A. Natan, “Electron Effective Mass in Graphene”, *arXiv pre-print*, p. 1206.6100, Jun. 2012. arXiv: [1206.6100](https://arxiv.org/abs/1206.6100).
- [29] T. Fang, A. Konar, H. Xing, and D. Jena, “Carrier statistics and quantum capacitance of graphene sheets and ribbons”, *Applied Physics Letters*, vol. 91, no. 9, p. 092 109, 2007. DOI: [10.1063/1.2776887](https://doi.org/10.1063/1.2776887). arXiv: [0707.2242v1](https://arxiv.org/abs/0707.2242v1).
- [30] A. Fasolino, J. H. Los, and M. I. Katsnelson, “Intrinsic ripples in graphene.”, *Nature materials*, vol. 6, no. 11, pp. 858–61, Nov. 2007. DOI: [10.1038/nmat2011](https://doi.org/10.1038/nmat2011).
- [31] D. Reddy, L. F. Register, G. D. Carpenter, and S. K. Banerjee, “Graphene field-effect transistors”, *Journal of Physics D: Applied Physics*, vol. 45, no. 1, p. 019 501, Jan. 2012. DOI: [10.1088/0022-3727/45/1/019501](https://doi.org/10.1088/0022-3727/45/1/019501).
- [32] K. D. Holland, N. Paydavosi, N. Neophytou, D. Kienle, and M. Vaidyanathan, “RF Performance Limits and Operating Physics Arising From the Lack of a Bandgap in Graphene Transistors”, *IEEE Transactions on Nanotechnology*, vol. 12, no. 4, pp. 566–577, Jul. 2013. DOI: [10.1109/TNANO.2013.2260351](https://doi.org/10.1109/TNANO.2013.2260351).
- [33] K. Wakabayashi, M. Fujita, H. Ajiki, and M. Sigrist, “Electronic and magnetic properties of nanographite ribbons”, *Physical Review B*, vol. 59, no. 12, pp. 8271–8282, Mar. 1999. DOI: [10.1103/PhysRevB.59.8271](https://doi.org/10.1103/PhysRevB.59.8271).
- [34] M. Han, B. Özyilmaz, Y. Zhang, and P. Kim, “Energy Band-Gap Engineering of Graphene Nanoribbons”, *Physical Review Letters*, vol. 98, no. 20, p. 206 805, May 2007. DOI: [10.1103/PhysRevLett.98.206805](https://doi.org/10.1103/PhysRevLett.98.206805).
- [35] P. Gallagher, K. Todd, and D. Goldhaber-Gordon, “Disorder-induced gap behavior in graphene nanoribbons”, *Physical Review B*, vol. 81, no. 11, p. 115 409, Mar. 2010. DOI: [10.1103/PhysRevB.81.115409](https://doi.org/10.1103/PhysRevB.81.115409).
- [36] M. Y. Han, J. C. Brant, and P. Kim, “Electron Transport in Disordered Graphene Nanoribbons”, *Physical Review Letters*, vol. 104, no. 5, p. 056 801, Feb. 2010. DOI: [10.1103/PhysRevLett.104.056801](https://doi.org/10.1103/PhysRevLett.104.056801).
- [37] A. Pieper, G. Schubert, G. Wellein, and H. Fehske, “Effects of disorder and contacts on transport through graphene nanoribbons”, vol. cond-mat.m, Aug. 2013. arXiv: [1308.6079](https://arxiv.org/abs/1308.6079).
- [38] Y. Yang and R. Murali, “Impact of Size Effect on Graphene Nanoribbon Transport”, *IEEE Electron Device Letters*, vol. 31, no. 3, pp. 237–239, Mar. 2010. DOI: [10.1109/LED.2009.2039915](https://doi.org/10.1109/LED.2009.2039915).
- [39] O. Habibpour, J. Vukusic, and J. Stake, “A 30-GHz Integrated Subharmonic Mixer Based on a Multichannel Graphene FET”, *IEEE Transactions on Microwave Theory and Techniques*, vol. 61, no. 2, pp. 841–847, Feb. 2013. DOI: [10.1109/TMTT.2012.2236434](https://doi.org/10.1109/TMTT.2012.2236434).
- [40] N. Meng, J. F. Fernandez, D. Vignaud, G. Dambrine, and H. Happy, “Fabrication and Characterization of an Epitaxial Graphene Nanoribbon-Based Field-Effect Transistor”, *IEEE Transactions on Electron Devices*, vol. 58, no. 6, pp. 1594–1596, Jun. 2011. DOI: [10.1109/TED.2011.2119486](https://doi.org/10.1109/TED.2011.2119486).

- 
- [41] K. Yan, H. Peng, Y. Zhou, H. Li, and Z. Liu, "Formation of bilayer bernal graphene: layer-by-layer epitaxy via chemical vapor deposition.", *Nano letters*, vol. 11, no. 3, pp. 1106–10, Mar. 2011. DOI: [10.1021/nl1104000b](https://doi.org/10.1021/nl1104000b).
- [42] L. Liu, H. Zhou, R. Cheng, W. J. Yu, Y. Liu, Y. Chen, J. Shaw, X. Zhong, Y. Huang, and X. Duan, "High-yield chemical vapor deposition growth of high-quality large-area AB-stacked bilayer graphene.", *ACS nano*, vol. 6, no. 9, pp. 8241–9, Sep. 2012. DOI: [10.1021/nn302918x](https://doi.org/10.1021/nn302918x).
- [43] F. Xia, D. B. Farmer, Y.-M. Lin, and P. Avouris, "Graphene field-effect transistors with high on/off current ratio and large transport band gap at room temperature.", *Nano letters*, vol. 10, no. 2, pp. 715–8, Feb. 2010. DOI: [10.1021/nl9039636](https://doi.org/10.1021/nl9039636).
- [44] L. Britnell, R. V. Gorbachev, R. Jalil, B. D. Belle, F. Schedin, a. Mishchenko, T. Georgiou, M. I. Katsnelson, L. Eaves, S. V. Morozov, N. M. R. Peres, J. Leist, a. K. Geim, K. S. Novoselov, and L. a. Ponomarenko, "Field-effect tunneling transistor based on vertical graphene heterostructures.", *Science (New York, N.Y.)*, vol. 335, no. 6071, pp. 947–50, Feb. 2012. DOI: [10.1126/science.1218461](https://doi.org/10.1126/science.1218461).
- [45] S. Vaziri, G. Lupina, C. Henkel, A. D. Smith, M. Ostling, J. Dabrowski, G. Lippert, W. Mehr, and M. C. Lemme, "A graphene-based hot electron transistor.", *Nano letters*, vol. 13, no. 4, pp. 1435–9, Apr. 2013. DOI: [10.1021/nl304305x](https://doi.org/10.1021/nl304305x).
- [46] C. Zeng, E. B. Song, M. Wang, S. Lee, C. M. Torres, J. Tang, B. H. Weiller, and K. L. Wang, "Vertical graphene-base hot-electron transistor.", *Nano letters*, vol. 13, no. 6, pp. 2370–5, Jun. 2013. DOI: [10.1021/nl304541s](https://doi.org/10.1021/nl304541s).
- [47] W. Mehr, J. Dabrowski, J. C. Scheytt, G. Lippert, Y.-h. Xie, M. C. Lemme, M. Ostling, and G. Lupina, "Vertical Graphene Base Transistor", *IEEE Electron Device Letters*, vol. 33, no. 5, pp. 691–693, May 2012. DOI: [10.1109/LED.2012.2189193](https://doi.org/10.1109/LED.2012.2189193).
- [48] H. Hsu and L. Reichl, "Modeling graphene layers and single-walled carbon nanotubes with regularized  $\delta$ -function potentials", *Physical Review B*, vol. 72, no. 15, p. 155413, Oct. 2005. DOI: [10.1103/PhysRevB.72.155413](https://doi.org/10.1103/PhysRevB.72.155413).
- [49] A. K. Geim and K. S. Novoselov, "The rise of graphene.", *Nature materials*, vol. 6, no. 3, pp. 183–91, Mar. 2007. DOI: [10.1038/nmat1849](https://doi.org/10.1038/nmat1849).
- [50] Y.-W. Son, M. L. Cohen, and S. G. Louie, "Energy Gaps in Graphene Nanoribbons", *Physical Review Letters*, vol. 97, no. 21, p. 216803, Nov. 2006. DOI: [10.1103/PhysRevLett.97.216803](https://doi.org/10.1103/PhysRevLett.97.216803).
- [51] V. Barone, O. Hod, and G. E. Scuseria, "Electronic structure and stability of semiconducting graphene nanoribbons.", *Nano letters*, vol. 6, no. 12, pp. 2748–54, Dec. 2006. DOI: [10.1021/nl0617033](https://doi.org/10.1021/nl0617033).
- [52] G. Fiori and G. Iannaccone, "Simulation of Graphene Nanoribbon Field-Effect Transistors", *IEEE Electron Device Letters*, vol. 28, no. 8, pp. 760–762, Aug. 2007. DOI: [10.1109/LED.2007.901680](https://doi.org/10.1109/LED.2007.901680).
- [53] Y. Hancock, A. Uppstu, K. Saloriotta, A. Harju, and M. J. Puska, "Generalized tight-binding transport model for graphene nanoribbon-based systems", *Physical Review B*, vol. 81, no. 24, pp. 3–8, Jun. 2010. DOI: [10.1103/PhysRevB.81.245402](https://doi.org/10.1103/PhysRevB.81.245402).

- [54] Y. Ouyang, Y. Yoon, J. K. Fodor, and J. Guo, "Comparison of performance limits for carbon nanoribbon and carbon nanotube transistors", *Applied Physics Letters*, vol. 89, no. 20, p. 203 107, 2006. DOI: [10.1063/1.2387876](https://doi.org/10.1063/1.2387876).
- [55] G. Liang, N. Neophytou, D. E. Nikonov, and M. S. Lundstrom, "Performance Projections for Ballistic Graphene Nanoribbon Field-Effect Transistors", *IEEE Transactions on Electron Devices*, vol. 54, no. 4, pp. 677–682, Apr. 2007. DOI: [10.1109/TED.2007.891872](https://doi.org/10.1109/TED.2007.891872).
- [56] P. Zhao, M. Choudhury, K. Mohanram, and J. Guo, "Computational Model of Edge Effects in Graphene Nanoribbon Transistors", 2008. DOI: [10.1007/s12274-008-8039-y](https://doi.org/10.1007/s12274-008-8039-y).
- [57] V. Ryzhii, M. Ryzhii, A. Satou, and T. Otsuji, "Current-voltage characteristics of a graphene-nanoribbon field-effect transistor", *Journal of Applied Physics*, vol. 103, no. 9, p. 094 510, 2008. DOI: [10.1063/1.2917284](https://doi.org/10.1063/1.2917284).
- [58] W. Liu, X. Jin, X. Xi, J. Chen, M.-C. Jeng, Z. Liu, Y. Cheng, K. Chen, M. Chan, K. Hui, J. Huang, R. Tu, P. K. Ko, and C. Hu, *BSIM3v3.3 MOSFET Model*, Berkeley, 2005.
- [59] A. Khakifirooz, O. M. Nayfeh, and D. Antoniadis, "A Simple Semiempirical Short-Channel MOSFET Current–Voltage Model Continuous Across All Regions of Operation and Employing Only Physical Parameters", *IEEE Transactions on Electron Devices*, vol. 56, no. 8, pp. 1674–1680, Aug. 2009. DOI: [10.1109/TED.2009.2024022](https://doi.org/10.1109/TED.2009.2024022).
- [60] I. Meric, M. Y. Han, A. F. Young, B. Ozyilmaz, P. Kim, and K. L. Shepard, "Current saturation in zero-bandgap, top-gated graphene field-effect transistors.", *Nature nanotechnology*, vol. 3, no. 11, pp. 654–9, Nov. 2008. DOI: [10.1038/nnano.2008.268](https://doi.org/10.1038/nnano.2008.268).
- [61] H. Wang, A. Hsu, J. Kong, D. A. Antoniadis, and T. Palacios, "Compact Virtual-Source Current–Voltage Model for Top- and Back-Gated Graphene Field-Effect Transistors", *IEEE Transactions on Electron Devices*, vol. 58, no. 5, pp. 1523–1533, May 2011. DOI: [10.1109/TED.2011.2118759](https://doi.org/10.1109/TED.2011.2118759).
- [62] E. Mucciolo, A. Castro Neto, and C. Lewenkopf, "Conductance quantization and transport gaps in disordered graphene nanoribbons", *Physical Review B*, vol. 79, no. 7, p. 075 407, Feb. 2009. DOI: [10.1103/PhysRevB.79.075407](https://doi.org/10.1103/PhysRevB.79.075407).
- [63] K. Ganapathi, Y. Yoon, M. Lundstrom, and S. Salahuddin, "Ballistic  $I_{\text{on}}/I_{\text{off}}$  Characteristics of Short-Channel Graphene Field-Effect Transistors: Analysis and Optimization for Analog", *IEEE Transactions on Electron Devices*, vol. 60, no. 3, pp. 958–964, Mar. 2013. DOI: [10.1109/TED.2013.2238236](https://doi.org/10.1109/TED.2013.2238236).
- [64] D. Mencarelli, T. Rozzi, and L. Pierantoni, "Scattering matrix approach to multichannel transport in many lead graphene nanoribbons.", *Nanotechnology*, vol. 21, no. 15, p. 155 701, Apr. 2010. DOI: [10.1088/0957-4484/21/15/155701](https://doi.org/10.1088/0957-4484/21/15/155701).
- [65] D. Mencarelli, L. Pierantoni, and T. Rozzi, "Graphene modeling by TLM approach", in *2012 IEEE/MTT-S International Microwave Symposium Digest*, IEEE, Jun. 2012, pp. 1–3. DOI: [10.1109/MWSYM.2012.6259782](https://doi.org/10.1109/MWSYM.2012.6259782).
- [66] X. Yang, G. Fiori, G. Iannaccone, and K. Mohanram, "Semi-analytical Model for Schottky-barrier Carbon Nanotube and Graphene Nanoribbon Transistors", in *Proceedings of the 20th symposium on Great lakes symposium on VLSI*, 2010, pp. 233–238.

- 
- [67] A. Rahman, S. Datta, and M. Lundstrom, “Theory of ballistic nanotransistors”, *IEEE Transactions on Electron Devices*, vol. 50, no. 9, pp. 1853–1864, Sep. 2003. DOI: [10.1109/TED.2003.815366](https://doi.org/10.1109/TED.2003.815366).
- [68] R. Landauer, “Spatial variation of currents and fields due to localized scatterers in metallic conduction”, *IBM Journal of Research and Development*, vol. 32, no. 3, pp. 306–316, May 1988. DOI: [10.1147/rd.323.0306](https://doi.org/10.1147/rd.323.0306).
- [69] K. Natori, “Ballistic metal-oxide-semiconductor field effect transistor”, *Journal of Applied Physics*, vol. 76, no. 8, p. 4879, 1994. DOI: [10.1063/1.357263](https://doi.org/10.1063/1.357263).
- [70] D. Jiménez, “A current-voltage model for Schottky-barrier graphene-based transistors.”, *Nanotechnology*, vol. 19, no. 34, p. 345 204, Aug. 2008. DOI: [10.1088/0957-4484/19/34/345204](https://doi.org/10.1088/0957-4484/19/34/345204).
- [71] G. S. Kliros, “Gate capacitance modeling and width-dependent performance of graphene nanoribbon transistors”, *Microelectronic Engineering*, Apr. 2013. DOI: [10.1016/j.mee.2013.04.011](https://doi.org/10.1016/j.mee.2013.04.011).
- [72] V. Ryzhii, M. Ryzhii, A. Satou, T. Otsuji, and V. Mitin, “Analytical device model for graphene bilayer field-effect transistors using weak nonlocality approximation”, *Journal of Applied Physics*, vol. 109, no. 6, p. 064508, 2011. DOI: [10.1063/1.3560921](https://doi.org/10.1063/1.3560921).
- [73] F. Schwierz, “Graphene transistors”, *Nature Nanotechnology*, vol. 5, no. 7, pp. 487–496, May 2010. DOI: [10.1038/nnano.2010.89](https://doi.org/10.1038/nnano.2010.89).
- [74] S. Thiele and F. Schwierz, “Modeling of the steady state characteristics of large-area graphene field-effect transistors”, *Journal of Applied Physics*, vol. 110, no. 3, p. 034506, 2011. DOI: [10.1063/1.3606583](https://doi.org/10.1063/1.3606583).
- [75] J. G. Champlain, “A first principles theoretical examination of graphene-based field effect transistors”, *Journal of Applied Physics*, vol. 109, no. 8, p. 084515, 2011. DOI: [10.1063/1.3573517](https://doi.org/10.1063/1.3573517).
- [76] V. Ryzhii, M. Ryzhii, A. Satou, T. Otsuji, and N. Kirova, “Device model for graphene bilayer field-effect transistor”, *Journal of Applied Physics*, vol. 105, no. 10, p. 104510, 2009. DOI: [10.1063/1.3131686](https://doi.org/10.1063/1.3131686).
- [77] G. I. Zebrev, A. A. Tselykovskiy, and V. O. Turin, “Physics-based compact modeling of double-gate graphene field-effect transistor operation”, in *2012 28th International Conference on Microelectronics Proceedings*, IEEE, May 2012, pp. 237–240. DOI: [10.1109/MIEL.2012.6222843](https://doi.org/10.1109/MIEL.2012.6222843). arXiv: [1110.6319](https://arxiv.org/abs/1110.6319).
- [78] I. Umoh and T. Kazmierski, “VHDL-AMS model of a dual gate graphene FET”, in *Specification and Design Languages (FDL), 2011 Forum on*, vol. 2, Oldenburg: IEEE, 2011, pp. 1–5.
- [79] I. J. Umoh, T. J. Kazmierski, and B. M. Al-Hashimi, “A Dual-Gate Graphene FET Model for Circuit Simulation—SPICE Implementation”, *IEEE Transactions on Nanotechnology*, vol. 12, no. 3, pp. 427–435, May 2013. DOI: [10.1109/TNANO.2013.2253490](https://doi.org/10.1109/TNANO.2013.2253490).
- [80] K. N. Parrish, M. E. Ramón, S. K. Banerjee, and D. Akinwande, “A Compact Model for Graphene FETs for Linear and Non-linear Circuits”, in *SISPAD 2012*, 2012, pp. 75–78.

- [81] W. Liu, *MOSFET Models for SPICE Simulation: Including BSIM3v3 and BSIM4*. Wiley-IEEE Press, 2011, ch. 1.3, p. 600.
- [82] K. N. Parrish and D. Akinwande, “Impact of contact resistance on the transconductance and linearity of graphene transistors”, *Applied Physics Letters*, vol. 98, no. 18, p. 183 505, 2011. DOI: [10.1063/1.3582613](https://doi.org/10.1063/1.3582613).
- [83] “International Technology Roadmap for Semiconductors - Emerging Research Materials”, International Roadmap Committee, Tech. Rep., 2011.
- [84] I. R. Committee, “International Technology Roadmap for Semiconductors - Interconnects”, Semiconductor Industry Association, Tech. Rep., 2011.
- [85] F. Xia, V. Perebeinos, Y.-m. Lin, Y. Wu, and P. Avouris, “The origins and limits of metal-graphene junction resistance.”, *Nature nanotechnology*, vol. 6, no. 3, pp. 179–84, Mar. 2011. DOI: [10.1038/nnano.2011.6](https://doi.org/10.1038/nnano.2011.6).
- [86] K. L. Grosse, M.-H. Bae, F. Lian, E. Pop, and W. P. King, “Nanoscale Joule heating, Peltier cooling and current crowding at graphene-metal contacts.”, *Nature nanotechnology*, vol. 6, no. 5, pp. 287–90, May 2011. DOI: [10.1038/nnano.2011.39](https://doi.org/10.1038/nnano.2011.39).
- [87] K. Nagashio, T. Nishimura, K. Kita, and A. Toriumi, “Contact resistivity and current flow path at metal/graphene contact”, *Applied Physics Letters*, vol. 97, no. 14, p. 143 514, 2010. DOI: [10.1063/1.3491804](https://doi.org/10.1063/1.3491804).
- [88] A. D. Franklin, S.-j. Han, A. A. Bol, and V. Perebeinos, “Double Contacts for Improved Performance of Graphene Transistors”, *IEEE Electron Device Letters*, pp. 4–6, 2011. DOI: [10.1109/LED.2011.2173154](https://doi.org/10.1109/LED.2011.2173154).
- [89] C. Malec and D. Davidović, “Electronic properties of Au-graphene contacts”, *Physical Review B*, vol. 84, no. 3, pp. 4–7, Jul. 2011. DOI: [10.1103/PhysRevB.84.033407](https://doi.org/10.1103/PhysRevB.84.033407).
- [90] J. S. Moon, M. Antcliffe, H. C. Seo, D. Curtis, S. Lin, A. Schmitz, I. Milosavljevic, A. A. Kiselev, R. S. Ross, D. K. Gaskill, P. M. Campbell, R. C. Fitch, K.-M. Lee, and P. Asbeck, “Ultra-low resistance ohmic contacts in graphene field effect transistors”, *Applied Physics Letters*, vol. 100, no. 20, p. 203 512, 2012. DOI: [10.1063/1.4719579](https://doi.org/10.1063/1.4719579).
- [91] J. T. Smith, A. D. Franklin, D. B. Farmer, and C. D. Dimitrakopoulos, “Reducing Contact Resistance in Graphene Devices through Contact Area Patterning.”, *ACS nano*, no. Xx, Mar. 2013. DOI: [10.1021/nn400671z](https://doi.org/10.1021/nn400671z).
- [92] C. Malec, B. Elkus, and D. Davidović, “Vacuum-annealed Cu contacts for graphene electronics”, *Solid State Communications*, vol. 151, no. 23, pp. 1791–1793, Dec. 2011. DOI: [10.1016/j.ssc.2011.08.025](https://doi.org/10.1016/j.ssc.2011.08.025).
- [93] B. Huard, N. Stander, J. Sulpizio, and D. Goldhaber-Gordon, “Evidence of the role of contacts on the observed electron-hole asymmetry in graphene”, *Physical Review B*, vol. 78, no. 12, Sep. 2008. DOI: [10.1103/PhysRevB.78.121402](https://doi.org/10.1103/PhysRevB.78.121402).
- [94] D. B. Farmer, R. Golizadeh-Mojarad, V. Perebeinos, Y.-M. Lin, G. S. Tulevski, J. C. Tsang, and P. Avouris, “Chemical doping and electron-hole conduction asymmetry in graphene devices.”, *Nano letters*, vol. 9, no. 1, pp. 388–92, Jan. 2009. DOI: [10.1021/nl803214a](https://doi.org/10.1021/nl803214a).

- 
- [95] T. Mueller, F. Xia, M. Freitag, J. Tsang, and P. Avouris, “Role of contacts in graphene transistors: A scanning photocurrent study”, *Physical Review B*, vol. 79, no. 24, p. 245 430, 2009. DOI: [10.1103/PhysRevB.79.245430](https://doi.org/10.1103/PhysRevB.79.245430).
- [96] B. Huard, J. Sulpizio, N. Stander, K. Todd, B. Yang, and D. Goldhaber-Gordon, “Transport Measurements Across a Tunable Potential Barrier in Graphene”, *Physical Review Letters*, vol. 98, no. 23, pp. 8–11, Jun. 2007. DOI: [10.1103/PhysRevLett.98.236803](https://doi.org/10.1103/PhysRevLett.98.236803).
- [97] G. Giovannetti, P. Khomyakov, G. Brocks, V. Karpan, J. Van Den Brink, and P. Kelly, “Doping graphene with metal contacts”, *Physical review letters*, vol. 101, no. 2, p. 26 803, 2008.
- [98] P. Khomyakov, G. Giovannetti, P. Rusu, G. Brocks, J. van Den Brink, and P. Kelly, “First-principles study of the interaction and charge transfer between graphene and metals”, *Physical Review B*, vol. 79, no. 19, p. 195 425, May 2009. DOI: [10.1103/PhysRevB.79.195425](https://doi.org/10.1103/PhysRevB.79.195425).
- [99] G. Kotliar, S. Savrasov, K. Haule, V. Oudovenko, O. Parcollet, and C. Marianetti, “Electronic structure calculations with dynamical mean-field theory”, *Reviews of Modern Physics*, vol. 78, no. 3, pp. 865–951, Aug. 2006. DOI: [10.1103/RevModPhys.78.865](https://doi.org/10.1103/RevModPhys.78.865).
- [100] C. Gong, G. Lee, B. Shan, E. M. Vogel, R. M. Wallace, and K. Cho, “First-principles study of metal–graphene interfaces”, *Journal of Applied Physics*, vol. 108, no. 12, p. 123 711, 2010. DOI: [10.1063/1.3524232](https://doi.org/10.1063/1.3524232).
- [101] J. Sławińska, P. Dabrowski, and I. Zasada, “Doping of graphene by a Au(111) substrate: Calculation strategy within the local density approximation and a semiempirical van der Waals approach”, *Physical Review B*, vol. 83, no. 24, p. 245 429, Jun. 2011. DOI: [10.1103/PhysRevB.83.245429](https://doi.org/10.1103/PhysRevB.83.245429).
- [102] J. Granatier, P. Lazar, M. Otyepka, and P. Hobza, “The Nature of the Binding of Au, Ag, and Pd to Benzene, Coronene, and Graphene: From Benchmark CCSD(T) Calculations to Plane-Wave DFT Calculations.”, *Journal of chemical theory and computation*, vol. 7, no. 11, pp. 3743–3755, Nov. 2011. DOI: [10.1021/ct200625h](https://doi.org/10.1021/ct200625h).
- [103] K. Nagashio and A. Toriumi, “Density-of-States Limited Contact Resistance in Graphene Field-Effect Transistors”, *Japanese Journal of Applied Physics*, vol. 50, no. 7, p. 070 108, Jul. 2011. DOI: [10.1143/JJAP.50.070108](https://doi.org/10.1143/JJAP.50.070108).
- [104] S. Barraza-Lopez, M. Vanević, M. Kindermann, and M. Y. Chou, “Effects of Metallic Contacts on Electron Transport through Graphene”, *Physical Review Letters*, vol. 104, no. 7, p. 076 807, Feb. 2010. DOI: [10.1103/PhysRevLett.104.076807](https://doi.org/10.1103/PhysRevLett.104.076807).
- [105] P. Khomyakov, A. Starikov, G. Brocks, and P. Kelly, “Nonlinear screening of charges induced in graphene by metal contacts”, *Physical Review B*, vol. 82, no. 11, p. 115 437, Sep. 2010. DOI: [10.1103/PhysRevB.82.115437](https://doi.org/10.1103/PhysRevB.82.115437).
- [106] R. Nouchi and K. Tanigaki, “Empirical Modeling of Metal-Contact Effects on Graphene Field-Effect Transistors”, *Japanese Journal of Applied Physics*, vol. 50, no. 7, p. 070 109, Jul. 2011. DOI: [10.1143/JJAP.50.070109](https://doi.org/10.1143/JJAP.50.070109).

- [107] Z. Chen and J. Appenzeller, “Gate modulation of graphene contacts – on the scaling of graphene FETs”, in *VLSI Technology, 2009 Symposium on*, Honolulu, HI, 2009, pp. 128–129.
- [108] D. Berdebes, T. Low, Y. Sui, J. Appenzeller, and M. S. Lundstrom, “Substrate Gating of Contact Resistance in Graphene Transistors”, *IEEE Transactions on Electron Devices*, vol. 58, no. 11, pp. 3925–3932, Nov. 2011. DOI: [10.1109/TED.2011.2163800](https://doi.org/10.1109/TED.2011.2163800).
- [109] A. D. Franklin, S.-j. Han, A. A. Bol, and W. Haensch, “Effects of Nanoscale Contacts to Graphene”, *IEEE Electron Device Letters*, vol. 32, no. 8, pp. 1035–1037, Aug. 2011. DOI: [10.1109/LED.2011.2158058](https://doi.org/10.1109/LED.2011.2158058).
- [110] H. Berger, “Models for contacts to planar devices”, *Solid-State Electronics*, vol. 15, no. 2, pp. 145–158, Feb. 1972. DOI: [10.1016/0038-1101\(72\)90048-2](https://doi.org/10.1016/0038-1101(72)90048-2).
- [111] D. Schroder, *Semiconductor material and device characterization*. John Wiley & Sons, 2006.
- [112] C. Lan, P. Srisungsitthisunti, P. B. Amama, T. S. Fisher, X. Xu, and R. G. Reifenberger, “Measurement of metal/carbon nanotube contact resistance by adjusting contact length using laser ablation.”, *Nanotechnology*, vol. 19, no. 12, p. 125703, Mar. 2008. DOI: [10.1088/0957-4484/19/12/125703](https://doi.org/10.1088/0957-4484/19/12/125703).
- [113] C. Lan, D. N. Zakharov, and R. G. Reifenberger, “Determining the optimal contact length for a metal/multiwalled carbon nanotube interconnect”, *Applied Physics Letters*, vol. 92, no. 21, p. 213112, 2008. DOI: [10.1063/1.2931081](https://doi.org/10.1063/1.2931081).
- [114] K. Nagashio, T. Moriyama, R. Ifuku, T. Yamashita, T. Nishimura, and A. Toriumi, “Is Graphene Contacting with Metal Still Graphene?”, in *International Electron Devices Meeting 2011*, vol. 5, 2011, pp. 27–30.
- [115] W. Shockley, A. Goetzberger, and R. Scarlett, “Research and Investigation of Inverse Epitaxial UHF Power Transistors”, Air Force Avionics Lab., Wright-Patterson Air Force Base, Tech. Rep., 1964, pages.
- [116] D. Janes and K. Webb, “Error analysis leading to design criteria for transmission line model characterization of ohmic contacts”, *IEEE Transactions on Electron Devices*, vol. 48, no. 4, pp. 758–766, Apr. 2001. DOI: [10.1109/16.915721](https://doi.org/10.1109/16.915721).
- [117] L. Gutai, “Statistical modeling of transmission line model test structures. I. The effect of inhomogeneities on the extracted contact parameters”, *IEEE Transactions on Electron Devices*, vol. 37, no. 11, pp. 2350–2360, 1990. DOI: [10.1109/16.62287](https://doi.org/10.1109/16.62287).
- [118] G. S. Marlow and M. B. Das, “The effects of contact size and non-zero metal resistance on the determination of specific contact resistance”, *Solid-State Electronics*, vol. 25, no. 2, pp. 91–94, Feb. 1982. DOI: [10.1016/0038-1101\(82\)90036-3](https://doi.org/10.1016/0038-1101(82)90036-3).
- [119] M. Dragoman, D. Dragoman, G. Deligiorgis, G. Konstantinidis, D. Neculoiu, A. Cismaru, and R. Plana, “Current oscillations in a wide graphene sheet”, *Journal of Applied Physics*, vol. 106, no. 4, p. 044312, 2009. DOI: [10.1063/1.3208061](https://doi.org/10.1063/1.3208061).
- [120] G. Deligeorgis, M. Dragoman, D. Neculoiu, D. Dragoman, G. Konstantinidis, A. Cismaru, and R. Plana, “Microwave propagation in graphene”, *Applied Physics Letters*, vol. 95, no. 7, p. 073107, 2009. DOI: [10.1063/1.3202413](https://doi.org/10.1063/1.3202413).

- 
- [121] S. Moon, K. Jung, K. Park, H. Jin Kim, C.-W. Lee, C.-W. Baik, and J. M. Kim, “Intrinsic high-frequency characteristics of graphene layers”, *New Journal of Physics*, vol. 12, no. 11, p. 113031, Nov. 2010. DOI: [10.1088/1367-2630/12/11/113031](https://doi.org/10.1088/1367-2630/12/11/113031).
- [122] S. C. Jun, X. M. H. Huang, S. Moon, H. J. Kim, J. Hone, Y. W. Jin, and J. M. Kim, “Passive electrical properties of multi-walled carbon nanotubes up to 0.1 THz”, *New Journal of Physics*, vol. 9, no. 8, pp. 265–265, Aug. 2007. DOI: [10.1088/1367-2630/9/8/265](https://doi.org/10.1088/1367-2630/9/8/265).
- [123] H. S. Skulason, H. V. Nguyen, a. Guermoune, V. Sridharan, M. Siaj, C. Caloz, and T. Szkopek, “110 GHz measurement of large-area graphene integrated in low-loss microwave structures”, *Applied Physics Letters*, vol. 99, no. 15, p. 153504, 2011. DOI: [10.1063/1.3650710](https://doi.org/10.1063/1.3650710).
- [124] H.-J. Lee, E. Kim, J.-G. Yook, and J. Jung, “Intrinsic characteristics of transmission line of graphenes at microwave frequencies”, *Applied Physics Letters*, vol. 100, no. 22, p. 223102, 2012. DOI: [10.1063/1.4722585](https://doi.org/10.1063/1.4722585).
- [125] N. Rouhi, D. Jain, S. Capdevila, L. Jofre, E. Brown, and P. J. Burke, “Broadband conductivity of graphene from DC to THz”, in *2011 11th IEEE International Conference on Nanotechnology*, IEEE, Aug. 2011, pp. 1205–1207. DOI: [10.1109/NANO.2011.6144485](https://doi.org/10.1109/NANO.2011.6144485).
- [126] J. S. Gómez-Díaz, J. Perruisseau-Carrier, P. Sharma, and A. Ionescu, “Non-contact characterization of graphene surface impedance at micro and millimeter waves”, *Journal of Applied Physics*, vol. 111, no. 11, p. 114908, 2012. DOI: [10.1063/1.4728183](https://doi.org/10.1063/1.4728183).
- [127] P. Sharma, J. Gomez-Diaz, A. Ionescu, and J. Perruisseau-Carrier, “Determination of minimum conductivity of graphene from contactless microwaves measurements”, in *Nanotechnology (IEEE-NANO), 2012 12th IEEE Conference on*, 2012, pp. 1–4. DOI: [10.1109/NANO.2012.6322060](https://doi.org/10.1109/NANO.2012.6322060).
- [128] D. L. Sounas, H. S. Skulason, H. V. Nguyen, A. Guermoune, M. Siaj, T. Szkopek, and C. Caloz, “Faraday rotation in magnetically biased graphene at microwave frequencies”, *Applied Physics Letters*, vol. 102, no. 19, p. 191901, 2013. DOI: [10.1063/1.4804437](https://doi.org/10.1063/1.4804437).





## Chapter 3

# Graphene DC model

In this chapter the work on the DC modeling of graphene active devices will be presented. The described model is based on the Top of the Barrier approach, which is a physical semi-analytical ballistic model [1].

### 3.1 Motivation

The great majority of models used today to simulate the I-V characteristics of graphene devices are based on the Drift-Diffusion (DD) transport mechanism, upon which the industrial-standard model for Si CMOS, the BSIM is founded as well. DD is based on the assumption that in the channel of the transistor (or any other conductor) a certain amount of scattering centers exists, and that the conductivity depends on how many charge carriers there are and how frequently they collide with a scatterer; the carrier drift velocity is a function of the longitudinal electric field (given by the drain bias) and of the mobility and saturation velocity parameters. Voltage and current are related through the Drude model. However, if scattering is absent, as in an ideal ballistic transistor, the velocity of carriers assumes its maximum value: it is not anymore directly related to the longitudinal electric field, but with the potential drop between source and drain instead. DD models can include empirically the increase in saturation current that comes from ballistic effects, for example through the Source End Limit Velocity model as done for Si in BSIM4v4.7 [2], but their validity in regimes near to ideal ballistic transport becomes questionable.

The peculiarity of graphene is to support a very limited amount of scattering even at room temperature, especially when the interaction with the substrate is reduced [3]. Moreover, at the same time that the quality of graphene samples improves, the

channel lengths are scaled down too; this means that increasingly larger parts of the electron conduction should rely on ballistic transport [4]. A ballistic model of graphene nanotransistors becomes appropriate, but on the other hand their validity is generally given only when ballistic transport is dominant [5].

Finally, many models fragment their operation in multiple segments or regimes, according to the shape of the  $I_D(V_{DS})$  curve (linear, quasi-saturation, second linear) or to the type of charges within the channel (either electrons or holes, or both of them). In this last context the word “ambipolar” is frequently used even if inappropriate [6]. The fragmentation of the operation can lead to discontinuities in the  $g_m$  or in its derivative.

## 3.2 Objectives of the study

This part of the work aims at finding a model that can correctly simulate both nanoscale ballistic devices and microscale conventional Field Effect Transistors. This model should rely on physical equations, with a minimal use of empirical parameters. Finally, its operation should not be fragmented in different regimes.

## 3.3 Model: Top of the Barrier

In this section the discussion will be limited at the case of zero temperature. In the rest of the chapter, room temperature will be taken into account. The Top of the Barrier is a model that computes the carrier population of the channel of a transistor observing the energy of the free carriers that it contains and the contacts. Considering a free carrier at the edge of a contact, the barrier is the difference between the carrier’s energy, i.e. its Fermi potential, and the closest-free-state energy in the channel. Carriers from source and drain contacts are injected into the channel in a number dependent on the barrier’s height towards each contact: in a condition of nonzero source-drain bias, each contact causes a different amount of channel population, creating an unbalance between carriers from the source and carriers from the drain. This non-equilibrium condition makes the carriers move from source to drain, from the contact that fills the channel to the one that depletes it, creating a current. If the free-state energy drops between the contact’s energies, source and drain will inject respectively electrons and holes, and deplete the opposite carrier type. Eventually the action of the gate electrode can be included by shifting in energy the free states of the channel with a sign related to the gate bias polarity, a magnitude non-linearly related to the gate voltage, the channel doping and the injected carrier population. In the following sections each of those mechanisms will be thoroughly detailed.

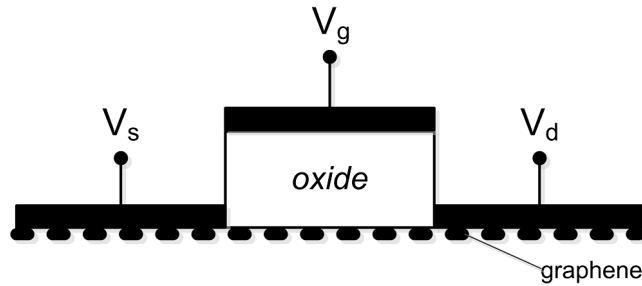


FIGURE 3.1: The cross-section of a graphene FET. Graphene is the black thick dotted line under contacts and gate oxide.

### 3.3.1 The Landauer Equation, carriers and contacts

In a top of the barrier framework either drift-diffusive (DD) or ballistic models can be used. Examples of DD applications are in [7], [8], and for ballistic models in [1]. The aim of this subsection is to describe the behavior of GNR-FET devices, in which small dimensions and characteristics make the ballistic transport dominant. A cross-section of the device is shown in Fig. 3.1. The Landauer equation will be used to quantify the current of ballistic electrons and holes. By separating between the electron and hole contributions, the drain current is given by [9]:

$$I_d = I_n - I_p, \quad (3.1)$$

where  $I_n$  and  $I_p$  correspond to electron and hole current respectively. A similar convention for all variables is followed throughout this chapter. The net current is given by the difference of the injected electron and hole currents. In a simplified ballistic regime, carriers are not subjected to recombination and are not exchanged between different conducting states, thus they can be considered as independent fluxes. Moreover, no energy relaxation into channel's statistics is assumed as scattering is neglected [10]. As opposed to DD, the Landauer equation allows for the computation of the current in a device without scattering. Free states (or modes) are responsible for transport, and each one of them is associated with a fixed conductivity  $q^2/h$ , where  $q$  is the electron charge and  $h$  is Planck's constant. Injected electrons from each contact through the barrier are described by the Fermi potential of their respective contact, and the injection unbalance is the difference of the two Fermi functions  $f_S$  and  $f_D$  times the density of states  $D_n(E)$ . After integrating over energy, the electron current is given by:

$$I_n = \frac{\bar{v}_x q}{2\hbar} \int_{-\infty}^{+\infty} D_n(E) (f_S - f_D) dE. \quad (3.2)$$

where  $\overline{v_x}$  is the averaged carrier velocity, which is calculated from the energy dispersion relation of the channel material. The dispersion relation is computed offline through a full-quantum model, generally Tight Binding (TB) solved through Non-Equilibrium Green's Functions (NEGF) as in [11] for the case of a GNR. The hole current is computed in a similar fashion. Differentiating the dispersion relation and averaging over all available subbands and  $k$ -space yields the band velocity:

$$\overline{v_x} = \frac{1}{2\pi} \int_{-\pi/a}^{+\pi/a} \frac{1}{N} \sum_{n=1}^N \left| \frac{1}{\hbar} \frac{d\epsilon_n(k)}{dk} \right| dk, \quad (3.3)$$

where  $k$  is the wavenumber,  $\epsilon_n(k)$  is the energy of the  $n$ -th sub-band of the nanoribbon and  $N$  is the number of unit cells. The averaging operation is a simplification with respect to [1] where the carrier velocity is expressed as a function of energy ( $v_x(E)$ ), but works around an intrinsic limit of the model. The geometry of the device is simplified and, as it will be clearer from the electrostatics section, the channel is represented dimensionlessly as a point. Carriers are injected at the top of the barrier, where their velocity is minimum and kept constant all along the channel, neglecting carrier acceleration (in a GNR, energy bands are parabolic as opposed to large area graphene where they show the double-cone shape). Tests have been conducted and this results in underestimation of the overall carrier velocity in the  $v_x(E)$  model, especially for high biasing conditions. Averaging its value over the entire  $k$ -space and all bands as in Eq. (3.3) can compensate for this error [9]. Therefore, constant carrier velocity formulation was chosen being both more accurate and simple compared to the energy-dependent expression. Finally, this method allows a more coherent and unified framework including the simulation of large-area graphene devices, which are in theory characterized by an energy independent carrier velocity.

The density of states  $D(E)$  is analytically derived from the bandstructure [12]. To account for impurities, the channel's Fermi energy is shifted by the Dirac voltage, here used as free parameter to describe the channel potential at zero bias. As the function relating the gate voltage and the channel potential is strongly non-linear, it's not possible to retrieve the channel potential from, say, an  $I_D - -V_{GS}$  measure of the conductivity at low drain bias; the lowest point in the V-shaped  $I_D - -V_{GS}$  indicates the gate voltage at which the channel potential crosses the Charge Neutrality Point (CNP), but the channel potential magnitude is generally smaller than the gate voltage. Its value must be found iteratively by computing the minimum conductivity point in a low-bias  $I_D(V_D)$  simulation [1].

Assuming the source contact potential is set as the reference, the drain potential is given by  $-qV_{ds}$ , where  $q$  is the electron charge and  $V_{ds}$  is the drain-source voltage difference.

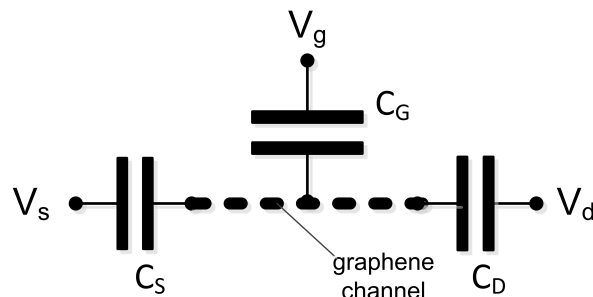


FIGURE 3.2: The lumped element model for the electrostatic part of the problem.

For this case, the expressions of the Fermi Dirac statistic  $f_S$  for the source and  $f_D$  for the drain become:

$$f_S(E) \equiv f_{\text{FD}}(E), \quad (3.4a)$$

$$f_D(E) \equiv f_{\text{FD}}(E - qV_{\text{ds}}), \quad (3.4b)$$

where  $f_{\text{FD}}$  is the Fermi-Dirac statistics equation.

### 3.3.2 Electrostatics

The amount of injection depends mainly from the barrier height towards the contacts; while the free states in the channel are located at energies which are characteristic of the material and its geometry, their absolute position can be moved by shifting the channel's Fermi potential with the gate electrode. A very convenient way to represent this shift is to replace the energy  $E$  with the difference  $E - U$ , where  $U$  is the electrostatic potential. Thus, the following quantities will be used:

- The density of states  $D_{(n,p)}(E - U)$ ;
- The contact Fermi statistics  $f_S(E - U)$  and  $f_D(E - U)$  in eqs. (3.4).

The potential  $U$  can in turn be expressed as the sum of two terms [13], namely the charge-less Laplace potential  $U_L$  and the mobile charge potential  $U_P$ :

$$U = U_L + U_P. \quad (3.5)$$

The Laplace potential  $U_L$  is the potential that would be present if the channel was a perfect insulator between the source electrode, grounded, and the gate electrode (for simplicity no bulk electrode is considered). The computation of its value at a precise point in the geometry is possible through a FEM simulator like COMSOL<sup>(TM)</sup>, solving

the Laplace equation for electrostatic potential. However, to obtain a value for the entire channel an average operation would be envisaged, but this is not possible: in an open neighborhood of either the source or drain electrodes the potential follows the electrode's one, rendering the average operation pointless. This puts a theoretical limit to the applicability of FEM for this task, other than the computational complexity added to each bias step. A more convenient way to treat this problem is to consider the channel as the central node of a capacitor network [1], as shown in Fig. 3.2, composed by the gate, source and drain capacitances towards the channel, called respectively  $C_G$ ,  $C_S$  and  $C_D$ . The gate term is just the capacitance across the gate oxide, to be computed only once through simple analytical formulas or FEM solution of a capacitor with metallic plates. The source and drain elements, equal in value, are instead left as fitting parameters as in [1]. In many works,  $C_G$  is thought as the series of the oxide capacitance  $C_{ox}$  and the quantum capacitance  $C_q$ . This latter is considered as a separate entity, a tool to obtain the channel potential, equal to the potential difference at its terminals. In addition, the dependence of  $C_q$  to the channel potential itself is sometimes neglected [14], even if it varies between a fraction of  $C_{ox}$  and many times its value. The top of the barrier model doesn't need  $C_q$ , as it computes directly the channel potential as a function of  $U_L$  and of  $U_P$ , in turn function of the channel carrier population. Taking into account that  $V_S = 0 V$ , the expression of the Laplace potential  $U_L$  becomes:

$$U_L = -q (C_G V_G + C_D V_D) . \quad (3.6)$$

$U_P$  is the sum of the potential increment from each charge added to the channel originally in equilibrium. It is calculated using a first-order linearized Poisson equation, where the potential is proportional to the charge unbalance in the channel. Taking into account both electrons and holes it is:

$$U_P = \frac{q^2}{C_\Sigma} (N - N_0 - P + P_0) , \quad (3.7)$$

where  $C_\Sigma$  is the sum of the three capacitors described above,  $N$  and  $N_0$  are the number of mobile and fixed electrons in the channel respectively,  $P$  and  $P_0$  are the respective number of holes.

### 3.3.3 The channel population: closing the loop

The number of fixed charges  $N_0$  and  $P_0$  are computed only once as the energy integral of  $D_{(n,p)}(E)$  times the Fermi statistic at equilibrium:

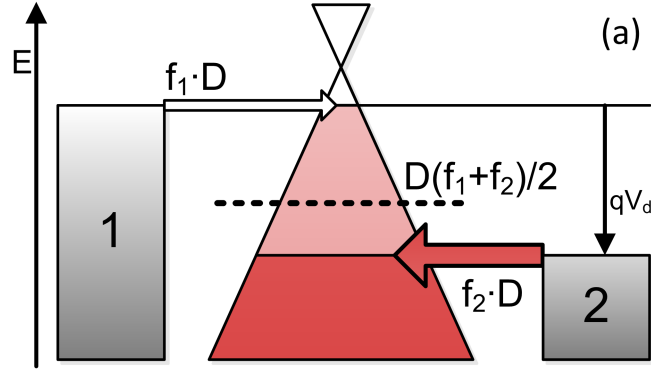


FIGURE 3.3: Injection of carriers into the channel. The double cone is the density of states of large-area graphene, whereas “1” and “2” respectively are the pseudo-Fermi levels of source and drain contacts. The black dashed line represents the population of carriers, according to the two contacts.

$$N_0 = \int_{-\infty}^{+\infty} D(E) f_{\text{FD}} dE. \quad (3.8)$$

The Fermi potential of the channel is slightly shifted by the Dirac voltage, generating a doping which reflects in the numbers  $N_0$  and  $P_0$ . The mobile charge in the channel is obtained averaging the Fermi potentials of the two contacts integrated in energy. The integral independent variable is shifted by the electrostatic potential  $U$  (not shown).

$$N = \int_{-\infty}^{+\infty} D(E) \cdot \left( \frac{f_{\text{S}} + f_{\text{D}}}{2} \right) dE. \quad (3.9)$$

A similar expression is used for holes. Fig. 3.3 depicts the channel under the injection of carriers from the source and the drain contact, whose pseudo-Fermi levels are labeled “1” and “2” respectively. The source injects carriers — in this case holes — which are described by the respective pseudo-Fermi potential and move to the right; similarly, the drain injects carriers moving to the left. With the simplified notation  $D(f_1 + f_2)/2$  the average of the two injected fluxes, i.e. the total number of out-of-equilibrium carriers in the channel, is indicated. Unfortunately, eqs. (3.5) and (3.9) cannot be easily put in a system and solved together because of the strong non-linear behavior of Fermi statistics; instead, those two expressions together with eq. (3.5) can be easily solved iteratively, with moderate computational cost, in a self-consistent loop. Finally equations (3.3) and (3.4) are used to compute the current for a given bias through equations (3.2) and (3.1).



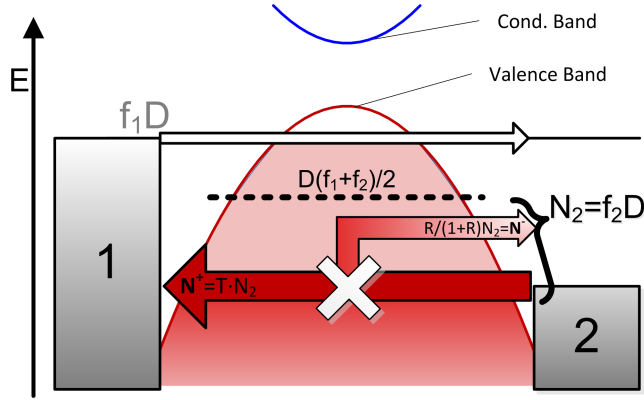


FIGURE 3.4: Quasi-ballistic injection into a nanoscale semiconductor, with parabolic subbands. Levels “1” and “2” respectively are the pseudo-Fermi levels of source and drain contacts. The grey dashed line represents the population of carriers, according to the two contacts.  $N_2$  is the total injected charge from contact “2”, sum of  $N^+$  and  $N^-$ .

### 3.4 Method: Extending the model to GFETs

The Top of the Barrier model has originally been developed for the simulation of nanoscale MOSFETs in silicon or III-V technologies. Their results have been compared against more complex simulations, such as those presented in [15], [16], and experimental data, as in [17], suggesting that nanoscale devices are likely to operate still quite far from the ideal ballistic case. This holds true for carbon devices too, where scattering mechanisms are very similar to semiconductor’s [18], [19], and that become effective already in the tens of nanometers scale [20]. The model described so far is inadequate for large channel lengths where diffusive transport becomes dominant. The modifications introduced for nanoscale MOSFETs (in which we note that the simultaneous electron and hole transport phenomenon is negligible compared to gapless graphene) allow for a qualitative understanding of the quasi-ballistic transport regime.

The ideal ballistic model builds a picture where all injected electrons are delivered at the opposite electrode, such as their transmission coefficient  $T \simeq 1$  and the corresponding back-scattering parameter  $(1 - T) = R \simeq 0$ . Carriers that originate from the source contact are all described by the source pseudo-Fermi potential. Assuming that the distribution of scatterers is nonzero but uniform across the channel, the increase in length of the channel affects the transmission of carriers and the value of  $T$  decreases approaching 0. Thus a fraction  $T = 1 - R$  of the total charge advances at its own pace towards the opposite electrode, and a fraction  $R$  of the injected charge suffers scattering. In Fig. 3.4 the total injected charge  $N_1$ , sum of those propagated and reflected, contribute to the electrostatic potential of the channel. In section 5.7 of ref. [21] it is proposed that

the current of the quasi-ballistic (QB) device should be expressed as a fraction of the ideal ballistic one:

$$I_{\text{QB}} = I_{\text{Bal}}T/(1 + R). \quad (3.10)$$

where  $I_{\text{QB}}$  is the QB current and  $I_{\text{Bal}}$  is the ideal one. From Eq. 3.10 it's possible to see how the effect of scattering is twofold: the current is reduced because only a fraction  $T$  of carriers traverses the channel, but also because for the same total charge (which is set by  $V_{\text{GS}}$ ) only a fraction  $1/(1 + R)$  of the carrier density is available to support transport in the positive (unreflected) direction. In this picture developed for semiconductors, a consistent amount of electrons are backscattered towards the source electrode and, at the same time, contribute for the electrostatic potential of the channel together with those moving in the positive direction. A distinction between elastic scattering (reflection without energy loss) and inelastic scattering (energetically non-conservative) processes is made. However, graphene is better described as a semimetal, and its equilibrium potential resides, unless of a residual doping captured by a small Dirac potential, at the CNP. Moreover, the distinction in terms of effects on the current between elastic and inelastic scattering processes can be perceived as purely academic if the first is always followed by the second as reported in [10], especially at room temperature. This causes scattered electrons (or holes) in graphene to be “removed” from the ensemble of injected electrons, resuming their path through thermalization, thus recovering the charge equilibrium state.

### 3.4.1 Scattering and channel population

To account for the effects on graphene's carrier population due to scattering, the Top of the barrier model has been modified in [9]. The central assumption is that the portion of carriers that ballistically traverse the channel decrease in number. Those that have scattered either by elastic or inelastic scattering regain the thermodynamic equilibrium and should finally be described by the channel Fermi level. The effect that this assumption has on the current is substantially different from that introduced by [22]: it cannot be described simply by a coefficient in the current of the device. As reported in ref. [16] after full-quantum Monte-Carlo simulations, the assumption of charge invariance made by [22] drops for devices where the Drain Induced Barrier Lowering (DIBL) effect is strong: indeed, graphene devices shows carrier type inversion (from electron to holes and vice versa) and eventually Negative Differential Resistance (NDR) behavior [23], [24] with increasing drain bias [14], so the injected charge is expected to vary strongly

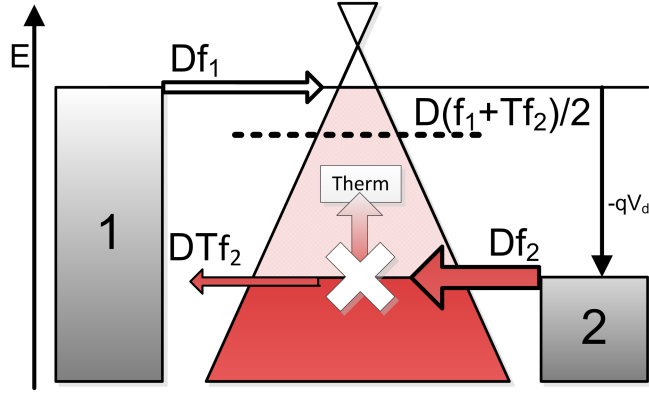


FIGURE 3.5: Quasi-ballistic injection in graphene. Levels “1” and “2” respectively are the pseudo-Fermi levels of source and drain contacts. The black dashed line represents the new population of carriers, according to the two injected charge amounts.  $Df_2$  is the total injected charge from contact “2”, while  $DTf_2$  alone traverses the channel and participate to the channel electrostatic potential.

with the amount of scattering. Hence, the entire electrostatic and electrodynamic problem is deeply affected by carrier thermalization, which should be included in the model starting from the self-consistent carrier density and potential computation step. Fig. 3.5 shows a simplified case in which a single scattering process divides the drain flux in two parts: a fraction  $T$  that is transmitted and a fraction  $(1 - T)$  that is scattered. To restore the apparent reduction of carriers introduced into the ballistic model by using the  $T$  factor, a modified, effective pseudo-Fermi potential  $\varphi$  is defined. As described in [10],  $\varphi$  is the weighted average of the contact pseudo-Fermi and the channel Fermi level. The weight factor depends on the transmission probability  $T$ . This way, all carriers originating from the drain contact are described by the effective level  $\varphi$ . A parameter  $\lambda$  related to the mean free path is introduced to describe the transmission factor  $T$ . The relation between  $T$  and the channel length coordinate  $x$  [10] is:

$$T = \frac{\lambda}{\lambda + x}. \quad (3.11)$$

In order to obtain an effective value for  $\varphi$ , the average of  $T$  over the entire length of the channel is used:

$$\begin{aligned} \varphi &= \left[ 1 - \frac{1}{L} \int_0^L \frac{x}{L} (1 - T) dx \right] qV_{ds} \\ &= (1 - k) qV_{ds}. \end{aligned} \quad (3.12)$$

Thus,  $\varphi$  represents the effective value of drain bias that will be used in the model. It depends linearly from the parameter  $\lambda$ , and scales inversely with the gate length.

TABLE 3.1: Structure dimensions

	FET1	FET2
$L$	15 nm	3000 nm
$W$	1.35 nm	2100 nm
$t_{\text{ox}}$	1 nm	15 nm
$\epsilon_r$	3.9	16
$V_0$	/	2.45 V
$V_{\text{bs}}$	/	-40 V

This modification to the Top-of-the-barrier models allows simulating GFETs with gate lengths larger than the mean free path, including the effect of carrier thermalization. In the case of channels much shorter than the mean free path, this model reduces to the ideally ballistic Top-of-the-barrier representation.

## 3.5 Results

The model proposed in [9] has been validated against two devices presented in the literature. A narrow channel graphene nanoribbon transistor described in [25] and a large area wide channel graphene FET described in [14]. The two devices are shortly presented in Table 3.1.

### 3.5.1 GNR FET

The first device simulated is a GNR nanotransistor [25] with gate length  $L=15$  nm, based upon a semiconducting nanoribbon. For clarity, the device cross-section is sketched in Fig. 3.1. The parameters used by the model are calculated using the procedure described in § 3.2. The best results are obtained for a  $\lambda$  value of 21 nm. The current flowing through the device for two distinct drain voltages is depicted in Fig. 3.6.

The quality of the agreement to the current-voltage characteristics calculated in [25] is excellent for the low drain bias curve, while it is underestimated for the high drain bias one. This discrepancy, also identified in the original purely ballistic model [1], is due to the fact that under high bias the assumption of constant 0 eV at the source contact breaks down. One possible solution to this issue is to empirically identify a reference potential for each bias point [1]. However, this procedure introduces several free parameters and thus was not adopted in this work. Further testing of the importance of the scattering in the current-voltage characteristics has shown that there is a minor

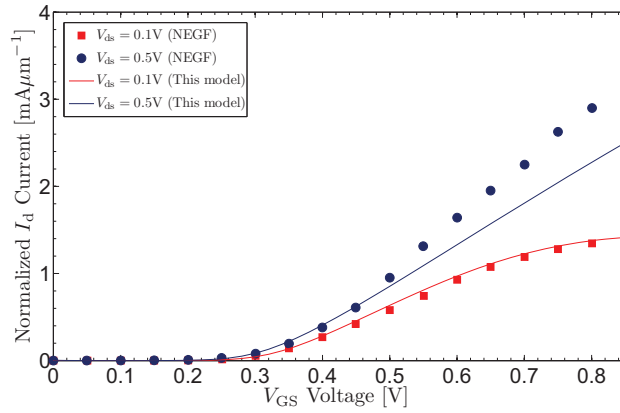


FIGURE 3.6: Transfer characteristic ( $I_d$ - $V_{gs}$ ) in linear scale for this model compared to NEGF from [25].

TABLE 3.2: Simulated transconductance  $g_m$  for FET1

$V_{ds}$	[25]	This model
V	$3.6 \text{ mS}\mu\text{m}^{-1}$	$3.55 \text{ mS}\mu\text{m}^{-1}$
0.5 V	$4.8 \text{ mS}\mu\text{m}^{-1}$	$4.81 \text{ mS}\mu\text{m}^{-1}$

effect originating from the introduced scattering parameter. Finally, Table 3.2 shows an excellent agreement of simulated  $g_m$  with that presented in [25].

### 3.5.2 GFET

The second device is a large-area graphene FET [14] with gate length  $L = 3 \mu\text{m}$  and width  $W = 2.1 \mu\text{m}$  (see Table 3.1). The structure of the FET (shown in Fig. 3.7) is slightly more complex because of the back-gate electrode. This can be taken into account by adding a backgate capacitance term in Eq. (3.6) which in turn becomes:

$$U_L = -q(C_B V_b + C_G V_g + C_D V_d). \quad (3.13)$$

where  $V_b$  is the potential of the back-gate electrode and  $V_g$  is the potential of the top-gate electrode. The values of the capacitors  $C_B$ ,  $C_G$  and  $C_D$  have been computed through a finite elements simulator. The use of large-area graphene also implies the use of the associated density of states equation, as described in [12].

The parameters of the large-area graphene model are the same of the GNR model, but the procedure to extract them is different. First, the Dirac voltage is empirically found by matching the position of the minimum conductivity point in the  $I_d(V_{gs})$  transfer characteristic. According to the discussion in reference [14], the gate voltage — which corresponds to minimum conduction — is  $V_{gs} = 2.38\text{V}$ ; the computed Dirac voltage has been found as  $V_{\text{Dirac}} = 0.213\text{V}$ .

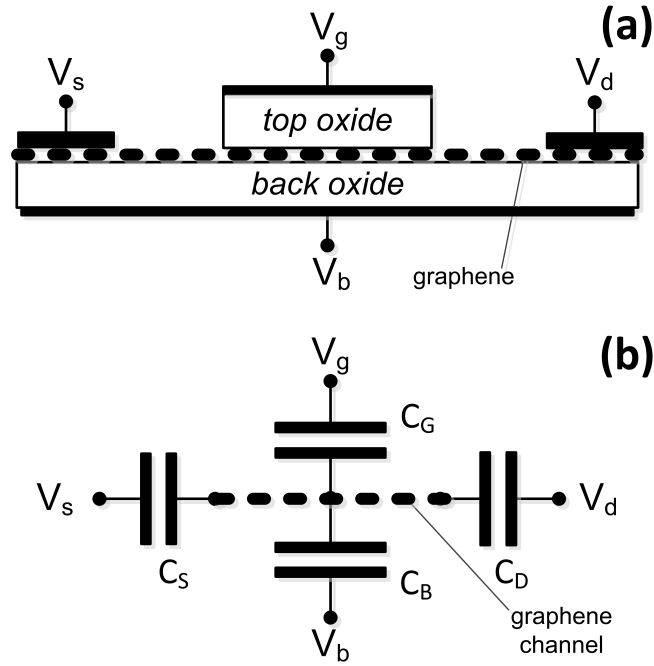


FIGURE 3.7: (a) The cross-section of the large-area graphene FET of [14]. Graphene is the black thick dotted line under contacts and top-gate oxide. A global back-gate electrode is shown under the back-gate oxide. (b) The lumped element model that accounts for the electrostatics of a large-area double-gate device.

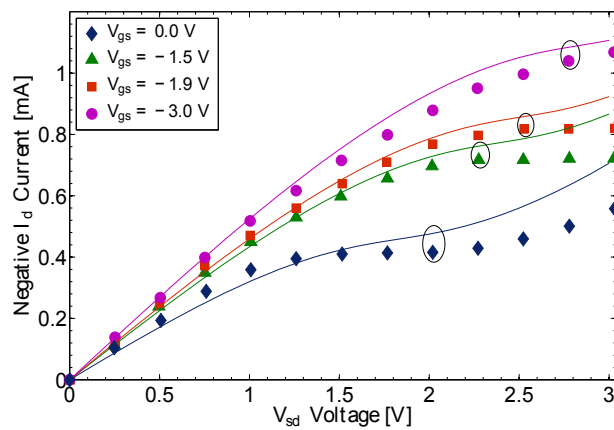


FIGURE 3.8: Simulated  $I_d(V_{sd})$  current for FET2 (solid lines) for Gate voltages from  $V_{gs} = 0$  V to  $-3$  V compared to measurement (markers only).

TABLE 3.3: Peak transconductance  $g_m$  for FET2

$V_{gs}$	[14]	This model
-1.5 V	211 $\mu\text{S}$	180 $\mu\text{S}$
-2.9 V	205 $\mu\text{S}$	186 $\mu\text{S}$

TABLE 3.4: Fit parameters for FET1 and FET2

Name	FET1	FET2
$\bar{v}_x$	Eq. (3.3)	$3.25 \times 10^4 \text{ ms}^{-1}$
$V_{\text{Dirac}}$	-0.062 V	0.213 V
$C_D$	$4.41 \times 10^{-20} \text{ F}$	$6.12 \times 10^{-17} \text{ F}$
$\lambda$	21 nm	380 nm

The  $\lambda$  parameter is calculated using the  $I_d(V_{ds})$  for low  $V_{ds}$ . In effect, the  $\lambda$  parameter will have a pronounced effect on the onset of the saturation effects in the  $I_d(V_{ds})$  curve. In this case the best value is  $\lambda = 380 \text{ nm}$  which is consistent with the value found in literature [20].

Finally, the value of the average carrier velocity is found empirically by matching simulations with the magnitude of the current. The best match was obtained at  $\bar{v}_x = 3.25 \cdot 10^4 \text{ ms}^{-1}$ . A direct comparison with literature is not possible, since drift-diffusion models use a saturation model for velocity, where drift velocity  $v_d$  is an empirical function of the longitudinal electric field [26]. The value of carrier velocity used in this model is however consistent with  $v_d$  that may be computed for similar structures in the literature [14], [27].

The output current  $I_d(V_{sd})$  is plotted in Fig. 3.8. The points correspond to DC current measurement taken from [14], whereas the group of solid lines are this model's predictions. It should be pointed out that although this is a compact model, unlike those described in [14], [27] and [28], it is able to correctly predict the presence of saturation effects in the current-voltage characteristics of the device. To our knowledge the only compact models presented so far with the ability to predict saturation and second linear characteristics of GFET's are based on different equations for each region [8], [29]. Unfortunately, the use of different set of equations for different regions may introduce artifacts in the continuity of the transconductance  $g_m$  or its derivative (see section 1.3 in [30]). Finally, Table 3.3 presents the peak measured and simulated  $g_m$  for two different gate biases. The agreement is not excellent but this could be attributed to the method used to compute  $g_m$  in [14] to remove the effects of the contacts.

In summary, the described model uses four parameters to fit the experimental results. Those are presented in Table 3.4, for the two simulated devices, with the exception of

TABLE 3.5: Model Comparison

	This work	DD	Tight Binding	BSIM 4.4 (CMOS)
Parameters	4	5 [28]	<10	>80
Dimensionality	0D	1D	1D to 3D	0D
CPU time/bias point	0.024 s	N/A	314 s	N/A
Operation regimes	1	1	1	4

the carrier velocity for FET1 which is analytically derived using (3.3).

### 3.6 Future work

The model presented so far has two issues that limit the quality of the simulation, respectively in the GNR-FET and GFET cases. The first one is the reference Fermi potential, which is set to the source potential that is considered fixed for the entire operation of the GNR-FET transistor. This is incorrect as has been demonstrated in ref. [1]; the same authors proposed a modification in the model involving a new free parameter to include for each operating point to be found in an empirical way. A better solution would be to obtain a relation between injected charge, current and the reference potential, which would be allowed to follow in some measure the channel's potential. Another point is the modeling of contact and access resistances to the channel, evolving the present model of the intrinsic transistor to a complete extrinsic model. Because the model does not include any invertible expression as opposed to, for example, the Ohm's law, a self-consistent iteration of applied external voltages and internal currents computed by the model is necessary.

### 3.7 Conclusions

In Table 3.5 a comparison between this work, Drift-Diffusion and NEGF research models and an industrial model (BSIM 4.4.0 for Silicon CMOS) is shown. Of particular relevance is the CPU time employed, on a 2007 Dell workstation, to compute the current of the 15nm GNR-FET for one bias point, for this model and for an in-house NEGF model. An improvement of more than 4 orders of magnitude is achieved.

In conclusion, a simple modification to the Top-of-the-barrier model that enables accurate simulation of a broad range of graphene based transistors was presented. The model retains the simplicity of a lumped element approach and is able to correctly describe the I-V characteristics of both ballistic and diffusive devices. Furthermore, it is able to correctly predict the behavior of both large-area as well as graphene nanoribbon based



field effect devices. Its simplicity compared to more complex model, like full-quantum NEGF, allow for its use in graphene-enabled circuit simulation tools.

## References

- [1] A. Rahman, S. Datta, and M. Lundstrom, “Theory of ballistic nanotransistors”, *IEEE Transactions on Electron Devices*, vol. 50, no. 9, pp. 1853–1864, Sep. 2003. DOI: [10.1109/TED.2003.815366](https://doi.org/10.1109/TED.2003.815366).
- [2] T. H. Morshed, D. D. Lu, W. ( Yang, V. M. Dunga, X. ( Xi, J. He, W. Liu, Kanyu, M. Cao, X. Jin, J. J. Ou, M. Chan, A. M. Niknejad, and C. Hu, “BSIM4v4.7 MOSFET Model”, Department of Electrical Engineering and Computer Sciences, University of California, Berkeley, Berkeley, Tech. Rep., 2011.
- [3] A. S. Mayorov, R. V. Gorbachev, S. V. Morozov, L. Britnell, R. Jalil, L. a. Ponomarenko, P. Blake, K. S. Novoselov, K. Watanabe, T. Taniguchi, and a. K. Geim, “Micrometer-scale ballistic transport in encapsulated graphene at room temperature.”, *Nano letters*, vol. 11, no. 6, pp. 2396–9, Jun. 2011. DOI: [10.1021/nl200758b](https://doi.org/10.1021/nl200758b).
- [4] Y. Wu, V. Perebeinos, Y.-m. Lin, T. Low, F. Xia, and P. Avouris, “Quantum behavior of graphene transistors near the scaling limit.”, *Nano letters*, vol. 12, no. 3, pp. 1417–23, Mar. 2012. DOI: [10.1021/nl204088b](https://doi.org/10.1021/nl204088b).
- [5] J. Chauhan, L. Liu, Y. Lu, and J. Guo, “A computational study of high-frequency behavior of graphene field-effect transistors”, *Journal of Applied Physics*, vol. 111, no. 9, p. 094313, 2012. DOI: [10.1063/1.4712323](https://doi.org/10.1063/1.4712323).
- [6] J. G. Champlain, “On the use of the term “ambipolar””, *Applied Physics Letters*, vol. 99, no. 12, p. 123502, 2011. DOI: [10.1063/1.3641898](https://doi.org/10.1063/1.3641898).
- [7] A. Khakifirooz, O. M. Nayfeh, and D. Antoniadis, “A Simple Semiempirical Short-Channel MOSFET Current–Voltage Model Continuous Across All Regions of Operation and Employing Only Physical Parameters”, *IEEE Transactions on Electron Devices*, vol. 56, no. 8, pp. 1674–1680, Aug. 2009. DOI: [10.1109/TED.2009.2024022](https://doi.org/10.1109/TED.2009.2024022).
- [8] H. Wang, A. Hsu, J. Kong, D. A. Antoniadis, and T. Palacios, “Compact Virtual-Source Current–Voltage Model for Top- and Back-Gated Graphene Field-Effect Transistors”, *IEEE Transactions on Electron Devices*, vol. 58, no. 5, pp. 1523–1533, May 2011. DOI: [10.1109/TED.2011.2118759](https://doi.org/10.1109/TED.2011.2118759).
- [9] G. Vincenzi, G. Deligeorgis, F. Coccetti, M. Dragoman, L. Pierantoni, D. Mencarelli, and R. Plana, “Extending ballistic graphene FET lumped element models to diffusive devices”, *Solid-State Electronics*, vol. 76, pp. 8–12, Oct. 2012. DOI: [10.1016/j.sse.2012.06.004](https://doi.org/10.1016/j.sse.2012.06.004).
- [10] S. Datta, *Electronic Transport in Mesoscopic Systems*. Cambridge University Press, 1995.
- [11] G. Liang, N. Neophytou, D. E. Nikonov, and M. S. Lundstrom, “Performance Projections for Ballistic Graphene Nanoribbon Field-Effect Transistors”, *IEEE Transactions on Electron Devices*, vol. 54, no. 4, pp. 677–682, Apr. 2007. DOI: [10.1109/TED.2007.891872](https://doi.org/10.1109/TED.2007.891872).

- 
- [12] T. Fang, A. Konar, H. Xing, and D. Jena, “Carrier statistics and quantum capacitance of graphene sheets and ribbons”, *Applied Physics Letters*, vol. 91, no. 9, p. 092 109, 2007. DOI: [10.1063/1.2776887](https://doi.org/10.1063/1.2776887). arXiv: [0707.2242v1](https://arxiv.org/abs/0707.2242v1).
- [13] S. Datta, *Quantum Transport: from Atom to Transistor*. Cambridge University Press, 2005.
- [14] I. Meric, M. Y. Han, A. F. Young, B. Ozyilmaz, P. Kim, and K. L. Shepard, “Current saturation in zero-bandgap, top-gated graphene field-effect transistors.”, *Nature nanotechnology*, vol. 3, no. 11, pp. 654–9, Nov. 2008. DOI: [10.1038/nnano.2008.268](https://doi.org/10.1038/nnano.2008.268).
- [15] J. Martin, A. Bournel, and P. Dollfus, “On the Ballistic Transport in Nanometer-Scaled DG MOSFETs”, *IEEE Transactions on Electron Devices*, vol. 51, no. 7, pp. 1148–1155, Jul. 2004. DOI: [10.1109/TED.2004.829904](https://doi.org/10.1109/TED.2004.829904).
- [16] P. Palestri, D. Esseni, S. Eminent, C. Fiegna, E. Sangiorgi, and L. Selmi, “Understanding Quasi-Ballistic Transport in Nano-MOSFETs: Part I—Scattering in the Channel and in the Drain”, *IEEE Transactions on Electron Devices*, vol. 52, no. 12, pp. 2727–2735, Dec. 2005. DOI: [10.1109/TED.2005.859593](https://doi.org/10.1109/TED.2005.859593).
- [17] A. Lochtefeld and D. Antoniadis, “On experimental determination of carrier velocity in deeply scaled NMOS: how close to the thermal limit?”, *IEEE Electron Device Letters*, vol. 22, no. 2, pp. 95–97, Feb. 2001. DOI: [10.1109/55.902843](https://doi.org/10.1109/55.902843).
- [18] M. I. Katsnelson and a. K. Geim, “Electron scattering on microscopic corrugations in graphene.”, *Philosophical transactions. Series A, Mathematical, physical, and engineering sciences*, vol. 366, no. 1863, pp. 195–204, Jan. 2008. DOI: [10.1098/rsta.2007.2157](https://doi.org/10.1098/rsta.2007.2157).
- [19] W. Zhu, V. Perebeinos, M. Freitag, and P. Avouris, “Carrier scattering, mobilities, and electrostatic potential in monolayer, bilayer, and trilayer graphene”, *Physical Review B*, vol. 80, no. 23, pp. 1–8, Dec. 2009. DOI: [10.1103/PhysRevB.80.235402](https://doi.org/10.1103/PhysRevB.80.235402).
- [20] Y.-W. Tan, Y. Zhang, K. Bolotin, Y. Zhao, S. Adam, E. H. Hwang, S. Das Sarma, H. L. Stormer, and P. Kim, “Measurement of Scattering Rate and Minimum Conductivity in Graphene”, *Physical Review Letters*, vol. 99, no. 24, p. 246 803, Dec. 2007. DOI: [10.1103/PhysRevLett.99.246803](https://doi.org/10.1103/PhysRevLett.99.246803).
- [21] D. Esseni, P. Palestri, and L. Selmi, *Nanoscale MOS Transistors*. Cambridge University Press, 2011, p. 488.
- [22] C. Jeong, D. A. Antoniadis, and M. S. Lundstrom, “On Backscattering and Mobility in Nanoscale Silicon MOSFETs”, *IEEE Transactions on Electron Devices*, vol. 56, no. 11, pp. 2762–2769, Nov. 2009. DOI: [10.1109/TED.2009.2030844](https://doi.org/10.1109/TED.2009.2030844).
- [23] Y. Wu, D. B. Farmer, W. Zhu, S.-J. Han, C. D. Dimitrakopoulos, A. a. Bol, P. Avouris, and Y.-M. Lin, “Three-terminal graphene negative differential resistance devices.”, *ACS nano*, vol. 6, no. 3, pp. 2610–6, Mar. 2012. DOI: [10.1021/nn205106z](https://doi.org/10.1021/nn205106z).
- [24] K. N. Parrish, M. E. Ramón, S. K. Banerjee, and D. Akinwande, “A Compact Model for Graphene FETs for Linear and Non-linear Circuits”, in *SISPAD 2012*, 2012, pp. 75–78.
- [25] G. Fiori and G. Iannaccone, “Simulation of Graphene Nanoribbon Field-Effect Transistors”, *IEEE Electron Device Letters*, vol. 28, no. 8, pp. 760–762, Aug. 2007. DOI: [10.1109/LED.2007.901680](https://doi.org/10.1109/LED.2007.901680).

- [26] C. Canali, G. Majni, R. Minder, and G. Ottaviani, “Electron and hole drift velocity measurements in silicon and their empirical relation to electric field and temperature”, *IEEE Transactions on Electron Devices*, vol. 22, no. 11, pp. 1045–1047, Nov. 1975. DOI: [10.1109/T-ED.1975.18267](https://doi.org/10.1109/T-ED.1975.18267).
- [27] S. A. Thiele, J. A. Schaefer, and F. Schwierz, “Modeling of graphene metal-oxide-semiconductor field-effect transistors with gapless large-area graphene channels”, *Journal of Applied Physics*, vol. 107, no. 9, p. 094505, 2010. DOI: [10.1063/1.3357398](https://doi.org/10.1063/1.3357398).
- [28] S. Thiele and F. Schwierz, “Modeling of the steady state characteristics of large-area graphene field-effect transistors”, *Journal of Applied Physics*, vol. 110, no. 3, p. 034506, 2011. DOI: [10.1063/1.3606583](https://doi.org/10.1063/1.3606583).
- [29] I. J. Umoh, T. J. Kazmierski, and B. M. Al-Hashimi, “A Dual-Gate Graphene FET Model for Circuit Simulation—SPICE Implementation”, *IEEE Transactions on Nanotechnology*, vol. 12, no. 3, pp. 427–435, May 2013. DOI: [10.1109/TNANO.2013.2253490](https://doi.org/10.1109/TNANO.2013.2253490).
- [30] W. Liu, *MOSFET Models for SPICE Simulation: Including BSIM3v3 and BSIM4*. Wiley-IEEE Press, 2011, ch. 1.3, p. 600.

## Chapter 4

# Graphene RF model

In this chapter the work on the DC and RF modeling of graphene passive devices will be presented. A lumped element model with frequency-independent parameters will be used to extract the material resistance and the contact impedance of the analyzed devices. This model will be used to project the expected performance from parameters found in literature.

### 4.1 Motivation

The parameters that have an influence on the high-frequency performance of the transistor, in particular the Figure of Merit (FOM) cut-off frequency  $f_T$  and maximum oscillation frequency  $f_{max}$ , are easily recognizable in the small signal model of the FET transistor, which for graphene-based devices maintains the same topology and components than the original one for semiconductors.

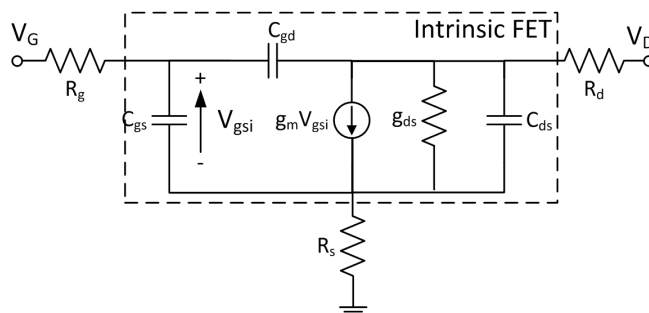


FIGURE 4.1: The small signal circuit of a typical FET device, showing the intrinsic device and its access and gate resistance parasitics, along with capacitive coupling between electrodes.

In Fig. 4.1 the encircled part of the circuit represents the intrinsic transistor, i.e. the ideal device without access parasitic impedances. Intrinsic values of FOM refer to the maximum theoretical performance that is obtained after de-embedding. However, despite the very high values of intrinsic  $f_T$  shown in some publications and the great attention given to those values in recent literature, their extrinsic values may give to the reader a more accurate idea of the actual performance and usefulness of a device. As an example, one of the highest reported intrinsic cut-off frequency in recent literature is equal to 350 GHz, while including parasitics the extrinsic  $f_T$  is thirty times less (10.5 GHz) [1]. The impact of the access resistance is central for the actual usability of graphene active and passive devices. Therefore its study on simplified structures like passive interconnects becomes crucial.

The access resistance is composed by the transition between metal and graphene (the contact resistance  $R_C$  and the contact capacitance  $C_C$ ) and the resistance of the ungated graphene between the source/drain electrode and the gate oxide/gate metal stack. If the channel potential has a different sign than the potential of the graphene physically in contact with the metal, a proper access resistance can account for the transport across the p-n transition that forms between the two. These phenomena are present in passive devices too, and they are profoundly influential on the total resistance of Interconnects.

The value of the contact resistance depends on many factors, including the quality and type of graphene, the metal stack, and the presence of lithographic residues. It can also depend on the length of the graphene strip that lies below the metal, if this is less than a few hundreds of nanometers. The Transmission Line Model (TLM) is the method commonly used by graphene and semiconductor device engineers to extract the value of  $R_C$ . It requires the fabrication of a dedicated test set of material strips of increasing length to allow the  $R_C$  extraction by linearization over contact separation (a recent and detailed example is found in [2]). The contact capacitance  $C_C$  is instead too often overlooked during the measurement and deembedding of active devices, and most of the times is incorporated in a parasitic pad capacitance. Nonetheless, this is a parameter whose presence is well established among fundamental studies of the graphene-metal contact [3], [4], and its exploration is tackled by a few studies on graphene passive devices [5].

## 4.2 Objectives of the study

This part of the work aims at finding an equivalent circuit model for passive graphene elements. This model should be suitable for the extraction of the contact impedance and the material resistivity by the DC and RF characterization of a single device. It should

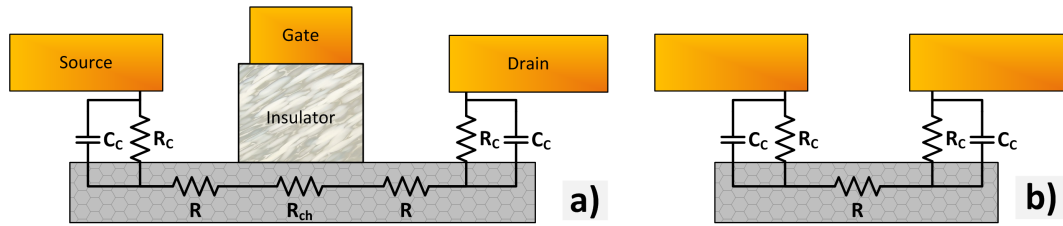


FIGURE 4.2: The equivalent circuit of a FET including access parasitics (a) and its simplified version for passive interconnects(b).

be composed by frequency-independent parameters and be valid in the whole spectrum of measurements (DC to 110 GHz).

### 4.3 Model

The equivalent circuit (EC) of a graphene interconnect is shown in Fig. 4.2(b) and includes only the resistance of the strip itself  $R$  (or its unitary equivalent, the sheet resistance  $R_{\square}$ ), the contact resistance  $R_C$  and the contact capacitance  $C_C$ . The sheet resistance of metals is much smaller than graphene's one because of the small carrier density in this latter, also for a small thickness: an 15 nm film of Cu has a sheet resistance of  $18.0 \Omega$  (including dimension-dependent scattering) [6], significantly lower than undoped graphene ( $R_{\square} = 6 k\Omega$ ) or even doped graphene ( $R_{\square} = 50 \Omega$ ) [7]. Typical values for pristine monolayer graphene gather around  $R_{\square} = 700 \Omega$ . This means that in the TLM contact model the current flows preferentially in the metal to follow the least resistance path, and enters graphene at the edge of the contact. The transfer length  $d_T$ , defined as the effective contact distance from the edge, is related to  $R_{\square}$  and the specific contact resistance per area  $\rho_{C\square}$ :

$$d_T = \sqrt{\frac{\rho_{C\square}}{R_{\square}}}, \quad (4.1)$$

and its value is generally well below one  $\mu\text{m}$ . Contact lengths larger than the transfer length make the current to crowd near the edge of the interface. Therefore,  $R_C$  is more simply related to the width of the contact alone (sometimes referred to as the *running length*), and accordingly expressed in  $[\Omega \cdot \text{mm}]$ , and not to its interface area. The contact capacitance  $C_C$  is also assumed to be by large more effective near the edge of the contact, but in present-day literature there are no experimental reports on the relationship between the contact reactance and the contact length. Theoretical studies instead relate this quantity to the interface area. In this work  $C_C$  will be related to the contact width and expressed in  $[F/\text{mm}]$ .

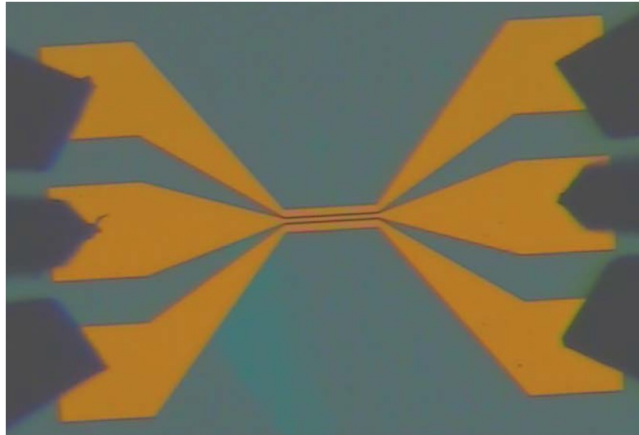


FIGURE 4.3: An optical micrograph of the CPW test bed and the on-wafer test probes for RF measurements.

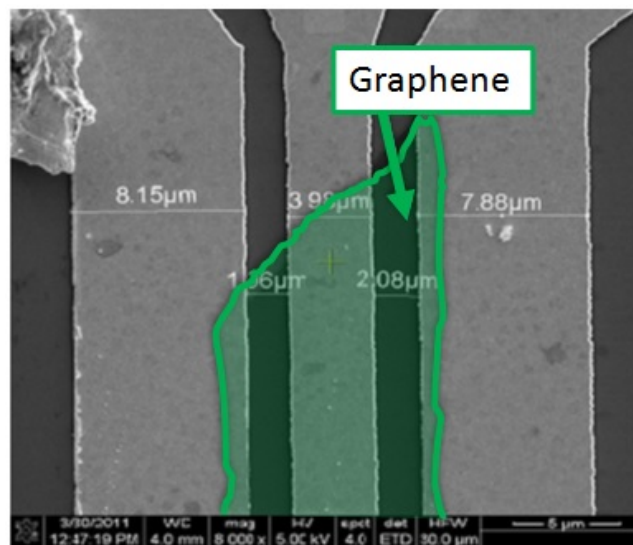


FIGURE 4.4: An SEM image of the CPW central electrode, the two Ground electrodes and of a part of the graphene flake shunting between them. The central line is  $4\ \mu\text{m}$  wide and the gaps between the lines are  $2\ \mu\text{m}$  wide.

## 4.4 Method

The EC has been used to reproduce the RF characteristics of a graphene device previously fabricated at FORTH (Heraklion, Greece) [8], [9] and measured in-house in both DC and RF. It consists of a metallic CPW line deposited over an exfoliated graphene monolayer flake acting as shunt load. Figures 4.3 and 4.4 show an optical micrograph of the device under test and a SEM of the same.

#### 4.4.1 Technology and design

The graphene monolayer flake was provided by Graphene Industries and deposited for optical identification on a 300 nm SiO<sub>2</sub>/n+ Si wafer, along with Raman spectrographic data to confirm the number of layers. The low-resistivity Si substrate was the only available from Graphene Industries at the time of the sample supply because of its versatility: it automatically provides a bottom-gate electrode for easy fabrication of graphene FETs. However, the presence of a lossy semiconductor below a microwave waveguide is detrimental for RF power, as the power on the signal line can capacitively couple to the substrate and to ground lines through the thin oxide. Another effect of the lossy substrate is to bend the electric field lines, altering the line capacitance of the structure and introducing mismatch losses.

A flake of monolayer graphene with dimensions about  $80 \times 20 \mu\text{m}$  was chosen and 2 nm Ti / 300 nm Au metal electrodes were successively deposited on top of it through an e-beam patterned lift-off process [8]. Owing to its reduced lateral dimension, a very narrow CPW was required to accommodate the central line and the inner edges of the ground lines on a continuous strip of graphene. The central line of the narrow CPW is 100  $\mu\text{m}$  long, 4  $\mu\text{m}$  wide and the gaps by the ground lines are 2  $\mu\text{m}$  wide. The small waveguide dimension was challenging for lithographic accuracy and originates significant ohmic losses: more than 35% of the power is lost at 20 GHz due to metal and substrate losses. This structure required tapered access lines to connect the 150  $\mu\text{m}$ -spaced RF landing pads. A Reference structure was also realized on the same Si substrate without graphene. Both CPW devices were measured at LAAS on a Karl-Suss on-wafer probe station with an Anritsu 37397C VNA with 110 GHz extension mixers connected to 110 GHz Picoprobe GSG probes at zero DC bias. The DC resistance between the signal electrode and one of the ground electrodes was measured at IMT (Bucharest, Romania) [9].

#### 4.4.2 EM model (MoM) and schematic

To model the RF behavior of the test bed a planar MoM simulator (Agilent ADS Momentum) has been used. It is adequately accurate on planar structures such as the CPW and can compute their S-parameters in a smaller time than full-wave 3D simulators like HFSS. As a first approach, a patch of a material with a given contact impedance was embedded in a MoM layout, but this proved to be a cumbersome task. The approach to model both structures has been simplified by putting the electromagnetic (EM) model into a SPICE-like circuit simulator (Agilent ADS Schematic). To do so, four open-loaded terminals have been added to the original EM model of the unloaded structure. Those



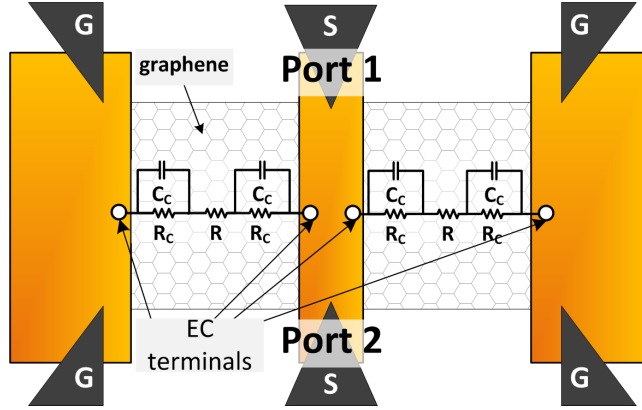


FIGURE 4.5: A simplified view of the layout of the test bed loaded with two parallel patches of graphene, and the EC of the same.

Material	Thickness [nm]	Conductivity [S/m]	Permittivity (real)	Loss tangent
Au	200	4.1e7	N.D.	N.D.
$SiO_2$	300	0	3.9	0.005
Si-n	(open boundary)	10	11.9	0

TABLE 4.1: List of materials used in the MoM simulation.

terminals, connected in the schematic circuit to two  $1\text{ M}\Omega$  loads (one for each branch of the CPW line) made the Reference model, whereas connecting the same to a pair of ECs shown in Fig. 4.2(b) allowed a good matching of the graphene-loaded structure's S-parameters. In Fig. 4.5 a simplified view of the layout connections is shown.

The material parameters for the EM simulation are summarized in Table 4.1. It should be noted that the thickness of the metallization has been fitted to match the low-frequency value of both  $|S_{11}|$  and  $|S_{21}|$ , keeping the  $\sigma$  of the metal constant. This allowed to match the series resistance of the central line measured with the VNA, finding a value slightly smaller than the nominal one used in fabrication. A number of issues during the fabrication could have caused this deviation: an smaller metal thickness, a certain degree of metal roughness or metal contamination; however, the correct isolation of each one of those issues is beyond the scope of this work; thus, an effective value of metal thickness of nominal conductivity is used.

As can be observed in Fig. 4.6, the simulated transmitted power  $S_{21}$  and total power losses of the Reference structure match well with measurements in both magnitude and phase, validating the quality of the EM model.

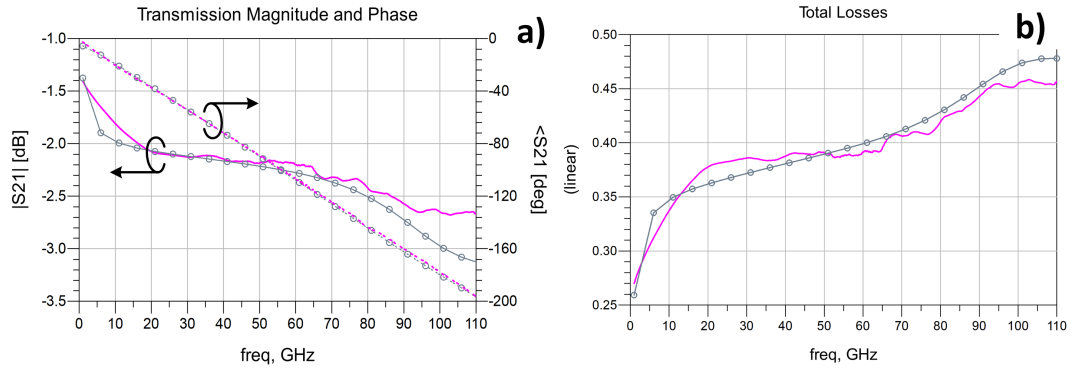


FIGURE 4.6: Measured S-parameters of the reference structure (pink line) vs. simulations (grey circles). (a) Transmission magnitude (left axis) and phase (right axis); (b) Total Losses ( $1 - |S_{11}|^2 - |S_{21}|^2$ ).

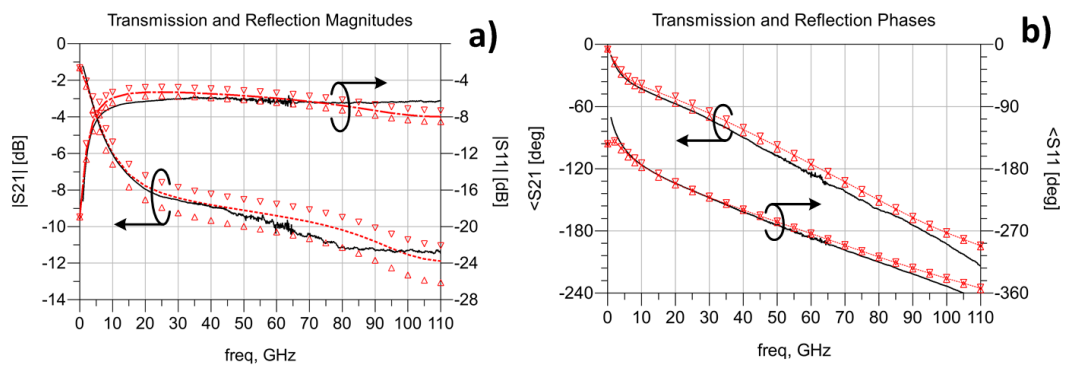


FIGURE 4.7: Measured S-parameters (black solid line) vs. simulations (red lines) of the graphene-loaded structure. The triangles indicate the maximum change against a variation of 10% of the circuit parameters. Transmission left Y-axis, Reflection right Y-axis; (a) Magnitude, (b) Phase.

## 4.5 Results

The embedded EC contains three parameters. From [9] the zero-bias DC value of the resistance of one patch of graphene has been taken, that is  $R_{dc} = 426 \text{ k}\Omega \cdot \mu\text{m}$ , constraining one parameter of the EC, as clarified by the following equation.

$$R_C = (R_{dc} - R) / 2, \quad (4.2)$$

This already allowed a perfect match with the lowest-frequency value of the S-parameters ( $f=40 \text{ MHz}$ , lower limit of the measurements). The matching on the rest of the spectrum was obtained by fitting the remaining two parameters,  $R$  and  $C_C$ . The agreement of simulated and measured Reflection and Transmission is shown in Fig. 4.7.

The extracted values of contact resistivity  $R_C$  and sheet resistivity  $R$  are summarized in the first row of Table 4.2, along with some values from literature.

Ref.	Year	Graphene Type	Metal Stack	$R_{\square}$ [ $\Omega$ ]	$R_C$ [ $\Omega \cdot mm$ ]
this work	2009	exfoliated	2 nm Ti/300 nm Au	1380	211.00
[10]	2010	exfoliated	Ti/Au	3800	5.00 $\div$ 60.00
[10]	2010	exfoliated	Ni	3800	0.50 $\div$ 4.00
[10]	2010	exfoliated	Cr/Au	3800	2.00 $\div$ 200.00
[11]	2011	CVD	20 nm Pd/30 nm Au	N.A.	0.60
[2]	2012	SiC	Ti/Pt/Au	236	0.07
[12]	2013	SiC	7 nm Pd/10 nm Au	N.A.	0.10

TABLE 4.2: Material and contact resistances from literature compared to those extracted by the model.

It must be noted that the  $R_C$  value of this device is the highest listed, worse than the ones reported in the same period and much worse than current state of the art. Moreover it is responsible for most of the resistance of the graphene patch ( ${}^2R_C/R_{dc} = 99\%$ ). This is probably because of a great amount of lithographic residues (PMMA) at the interface between graphene and metal, reducing the effective contact area. Annealing techniques to effectively remove residues [13], alternative support polymers such as Polycarbonate [14] and optimized metal stacks for the metal-graphene contact have since been discovered. Most of the advances on this subject have been the result of empirical studies, and the great attention devoted to it led to such performance improvement in small time. Today, to achieve low values of  $R_C$  metal stacks such as Ti/Pt/Au or Pd/Au are commonly used [2], [12]. The extracted value of the contact capacitance per unitary width is  $C_C = 9.38$  pF/mm, and its value per unitary surface is 4.68 fF/mm<sup>2</sup>. This value is compatible with the presence of a thin dielectric film at the metal/graphene interface (for PMMA with  $\epsilon_r = 2.6$ , a thickness  $d = 4.9$  nm is computed). However, the presence of a DC current across the metal/graphene interface suggests that graphene is, at least in some points, in physical contact with the metal, in a manner very similar to other studies based on the metal/metal contact [15]. Moreover, there is another contact phenomenon intrinsic in graphene: the interface charge accumulation, as foreseen by theoretical studies [16],[3]. It's not known yet if this acts as an actual capacitor, and it's not possible to divide the capacitance contribution across dielectric residues from the interface charge accumulation with this simple experiment.

#### 4.5.1 Performance projection with other graphene materials

Bulk and contact resistance values from various sources in literature, as well as those prospected for graphene in the Emerging Research Materials chapter of the ITRS 2011, have been used in the model described in § 4.4.2 to show the projected effects in the simulated passive RF device. In addition to those materials, state-of-art transparent graphene materials and indium tin oxide films have also been simulated. When not

Ref.	Year	Material	Metal Stack	$R_{\square}$ [ $\Omega$ ]	$R_C$ [ $\Omega \cdot mm$ ]
this work	2009	exf. graphene	TI/Au	1450	211.00
[2]	2012	SiC graphene	Ti/Pt/Au	236	0.07
[18]	2012	$FeCl_3$ intercalated gr.	N.A.	8.8	N.A. (0.07 used)
[19]	2001	ITO	N.A.	60	N.A. (0.07 used)
[17]	2011	graphene (ITRS-ERM'11)	N.A.	N.A.	1.0e-3

TABLE 4.3: Simulated performance comparison with alternative solutions.

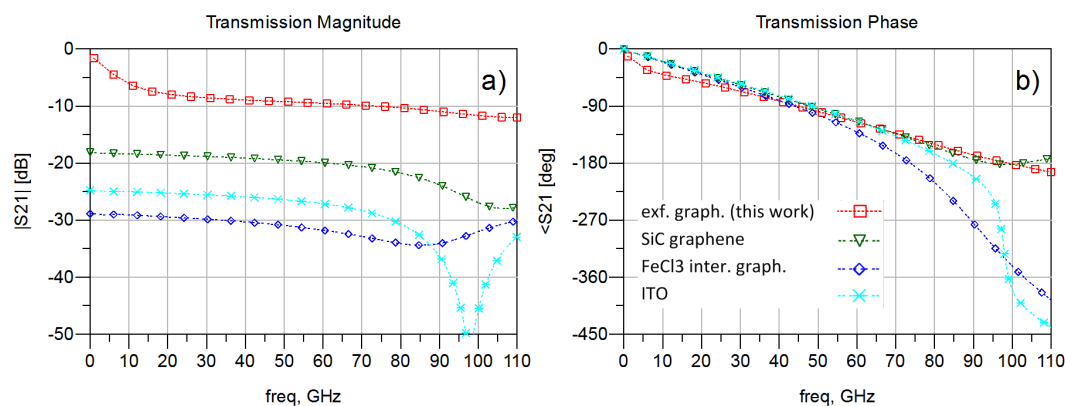


FIGURE 4.8: Simulated Transmission S-parameters for materials listed in Table 4.3); (a) Magnitude, (b) Phase.

available in literature, the value of  $R_C$  has been taken from [2], while the value of  $C_C$  used has been taken from this study. A summary of the parameters used in the simulation is found in the following table, and a comparison of magnitude and phase of  $S_{21}$  of the device is shown in Fig. 4.8. Being the target graphene sheet resistance not specified in the ITRS - Emerging Research Materials 2011 chapter [17], the simulation with this specific parameter set was not possible.

## 4.6 Chapter conclusions and future/ongoing work

In this chapter a wide band model describing the phenomena associated to the contact has been shown. This model allowed the extraction of resistive and capacitive parasites from DC and RF measurements of a single device, in the place of a dedicated set of devices as in the TLM method. Moreover, the parameters extracted here are frequency-independent, meaning that most of the physical phenomena involved are correctly addressed with the proper parameters, as opposed to other models showing resistances and capacitances whose values depend on frequency [20]. However, to complete the validation of the model an RF characterization of TLM-ordered structures is necessary. This kind of structures, like the one pictured in [3], are typically low-frequency only and do not support the transmission of a mm-wave RF signal without incurring serious mismatch losses and coupling, making it impossible to establish a relationship

between high-frequency impedance and geometrical dimensions. Moreover, the transfer length  $L_T$  has been studied only once and in DC only [21], and no models defining an equivalent quantity for the contact capacitance has been developed to date. A dedicated RF test structure with increasing graphene length and/or width must be fabricated and analyzed in order to compare the parameters extracted by the model shown here with those extracted by TLM. This topic will be addressed in the forthcoming chapter.

## References

- [1] Y. Wu, K. a. Jenkins, A. Valdes-Garcia, D. B. Farmer, Y. Zhu, A. a. Bol, C. Dimitrakopoulos, W. Zhu, F. Xia, P. Avouris, and Y.-M. Lin, “State-of-the-art graphene high-frequency electronics.”, *Nano letters*, vol. 12, no. 6, pp. 3062–7, Jun. 2012. DOI: [10.1021/nl300904k](https://doi.org/10.1021/nl300904k).
- [2] J. S. Moon, M. Antcliffe, H. C. Seo, D. Curtis, S. Lin, A. Schmitz, I. Milosavljevic, A. A. Kiselev, R. S. Ross, D. K. Gaskill, P. M. Campbell, R. C. Fitch, K.-M. Lee, and P. Asbeck, “Ultra-low resistance ohmic contacts in graphene field effect transistors” , *Applied Physics Letters*, vol. 100, no. 20, p. 203512, 2012. DOI: [10.1063/1.4719579](https://doi.org/10.1063/1.4719579).
- [3] F. Xia, V. Perebeinos, Y.-m. Lin, Y. Wu, and P. Avouris, “The origins and limits of metal-graphene junction resistance.”, *Nature nanotechnology*, vol. 6, no. 3, pp. 179–84, Mar. 2011. DOI: [10.1038/nnano.2011.6](https://doi.org/10.1038/nnano.2011.6).
- [4] D. Berdebes, T. Low, Y. Sui, J. Appenzeller, and M. S. Lundstrom, “Substrate Gating of Contact Resistance in Graphene Transistors” , *IEEE Transactions on Electron Devices*, vol. 58, no. 11, pp. 3925–3932, Nov. 2011. DOI: [10.1109/TED.2011.2163800](https://doi.org/10.1109/TED.2011.2163800).
- [5] S. Moon, K. Jung, K. Park, H. Jin Kim, C.-W. Lee, C.-W. Baik, and J. M. Kim, “Intrinsic high-frequency characteristics of graphene layers” , *New Journal of Physics*, vol. 12, no. 11, p. 113031, Nov. 2010. DOI: [10.1088/1367-2630/12/11/113031](https://doi.org/10.1088/1367-2630/12/11/113031).
- [6] “International Technology Roadmap for Semiconductors -Interconnects”, Tech. Rep., 2012.
- [7] P. Blake, P. D. Brimicombe, R. R. Nair, T. J. Booth, D. Jiang, F. Schedin, L. a. Ponomarenko, S. V. Morozov, H. F. Gleeson, E. W. Hill, A. K. Geim, and K. S. Novoselov, “Graphene-based liquid crystal device.”, *Nano letters*, vol. 8, no. 6, pp. 1704–8, Jun. 2008. DOI: [10.1021/nl080649i](https://doi.org/10.1021/nl080649i).
- [8] G. Deligeorgis, M. Dragoman, D. Neculoiu, D. Dragoman, G. Konstantinidis, A. Cismaru, and R. Plana, “Microwave propagation in graphene” , *Applied Physics Letters*, vol. 95, no. 7, p. 073107, 2009. DOI: [10.1063/1.3202413](https://doi.org/10.1063/1.3202413).
- [9] M. Dragoman, D. Dragoman, G. Deligiorgis, G. Konstantinidis, D. Neculoiu, A. Cismaru, and R. Plana, “Current oscillations in a wide graphene sheet” , *Journal of Applied Physics*, vol. 106, no. 4, p. 044312, 2009. DOI: [10.1063/1.3208061](https://doi.org/10.1063/1.3208061).
- [10] K. Nagashio, T. Nishimura, K. Kita, and A. Toriumi, “Contact resistivity and current flow path at metal/graphene contact” , *Applied Physics Letters*, vol. 97, no. 14, p. 143514, 2010. DOI: [10.1063/1.3491804](https://doi.org/10.1063/1.3491804).

- 
- [11] Y. Wu, Y.-m. Lin, A. a. Bol, K. a. Jenkins, F. Xia, D. B. Farmer, Y. Zhu, and P. Avouris, “High-frequency, scaled graphene transistors on diamond-like carbon.”, *Nature*, vol. 472, no. 7341, pp. 74–8, Apr. 2011. DOI: [10.1038/nature09979](https://doi.org/10.1038/nature09979).
- [12] Z. Guo, R. Dong, P. S. Chakraborty, N. Lourenco, J. Palmer, Y. Hu, M. Ruan, J. Hankinson, J. Kunc, J. D. Cressler, C. Berger, and W. a. de Heer, “Record maximum oscillation frequency in C-face epitaxial graphene transistors.”, *Nano letters*, vol. 13, no. 3, pp. 942–7, Mar. 2013. DOI: [10.1021/nl303587r](https://doi.org/10.1021/nl303587r).
- [13] A. Pirkle, J. Chan, A. Venugopal, D. Hinojos, C. W. Magnuson, S. McDonnell, L. Colombo, E. M. Vogel, R. S. Ruoff, and R. M. Wallace, “The effect of chemical residues on the physical and electrical properties of chemical vapor deposited graphene transferred to SiO<sub>2</sub>”, *Applied Physics Letters*, vol. 99, no. 12, p. 122 108, 2011. DOI: [10.1063/1.3643444](https://doi.org/10.1063/1.3643444).
- [14] Y.-C. Lin, C. Jin, J.-C. Lee, S.-F. Jen, K. Suenaga, and P.-W. Chiu, “Clean transfer of graphene for isolation and suspension.”, *ACS nano*, vol. 5, no. 3, pp. 2362–8, Mar. 2011. DOI: [10.1021/mn200105j](https://doi.org/10.1021/mn200105j).
- [15] C. Dervos and J. Michaelides, “The effect of contact capacitance on current-voltage characteristics of stationary metal contacts”, *IEEE Transactions on Components, Packaging, and Manufacturing Technology: Part A*, vol. 21, no. 4, pp. 530–540, 1998. DOI: [10.1109/95.740043](https://doi.org/10.1109/95.740043).
- [16] C. Gong, G. Lee, B. Shan, E. M. Vogel, R. M. Wallace, and K. Cho, “First-principles study of metal-graphene interfaces”, *Journal of Applied Physics*, vol. 108, no. 12, p. 123 711, 2010. DOI: [10.1063/1.3524232](https://doi.org/10.1063/1.3524232).
- [17] “International Technology Roadmap for Semiconductors - Emerging Research Materials”, International Roadmap Committee, Tech. Rep., 2011.
- [18] I. Khrapach, F. Withers, T. H. Bointon, D. K. Polyushkin, W. L. Barnes, S. Russo, and M. F. Craciun, “Novel highly conductive and transparent graphene-based conductors.”, *Advanced materials (Deerfield Beach, Fla.)*, vol. 24, no. 21, pp. 2844–9, Jun. 2012. DOI: [10.1002/adma.201200489](https://doi.org/10.1002/adma.201200489).
- [19] C. I. Bright, “Multilayer ITO Coatings with High Transparency and Low Sheet Resistance”, pp. 4–6, 2001.
- [20] H.-J. Lee, E. Kim, W.-J. Lee, and J. Jung, “RF transmission properties of graphene monolayers with width variation”, *physica status solidi (RRL) - Rapid Research Letters*, vol. 6, no. 1, pp. 19–21, Jan. 2012. DOI: [10.1002/pssr.201105378](https://doi.org/10.1002/pssr.201105378).
- [21] A. D. Franklin, S.-j. Han, A. A. Bol, and W. Haensch, “Effects of Nanoscale Contacts to Graphene”, *IEEE Electron Device Letters*, vol. 32, no. 8, pp. 1035–1037, Aug. 2011. DOI: [10.1109/LED.2011.2158058](https://doi.org/10.1109/LED.2011.2158058).



# Chapter 5

## Plastic test beds

In this chapter the design of a plastic test bed dedicated to the measurement of the sheet and contact impedance of various materials will be shown, along with expected values of the impedance characterization and performed measurements. A set of carbonaceous materials, including monolayer graphene, will be analyzed in DC and RF by the Transfer Length Method (TLM) and by the model presented in Chapter 4, showing a consistent validation of the same. Finally, the analysis of the RF impedance of contacts of reduced dimensions, named here Nanocontacts, will be shown.

### 5.1 Motivation

As discussed in § 4.1, the metal/graphene contact impedance is responsible for most of the performance degradation of the device. Other elements that seriously affect the performances are the structure and access lines connecting the RF probes to the actual device. Each unit Ohm of mismatch from  $50\Omega$  in the characteristic impedance introduces a reflection of around 4% of the input power, whereas a series resistance introduces mismatch and ohmic losses for about 4% per Ohm. Through careful design of RF access lines it's possible to minimize impedance mismatch and probes/device series resistance and maximize the signal delivered.

In some works there are microwave impedance tuning structures like inductors [1] or microstrip filters [2] fabricated on the same wafers of graphene amplifiers and mixers. These approaches are very effective to remove mismatch losses in common-source graphene FETs with a known, at least in some degree, high input impedance. Unfortunately in the case of an exploratory study when the input impedance is unknown it's not practical to design and fabricate an on-wafer tuning structure.



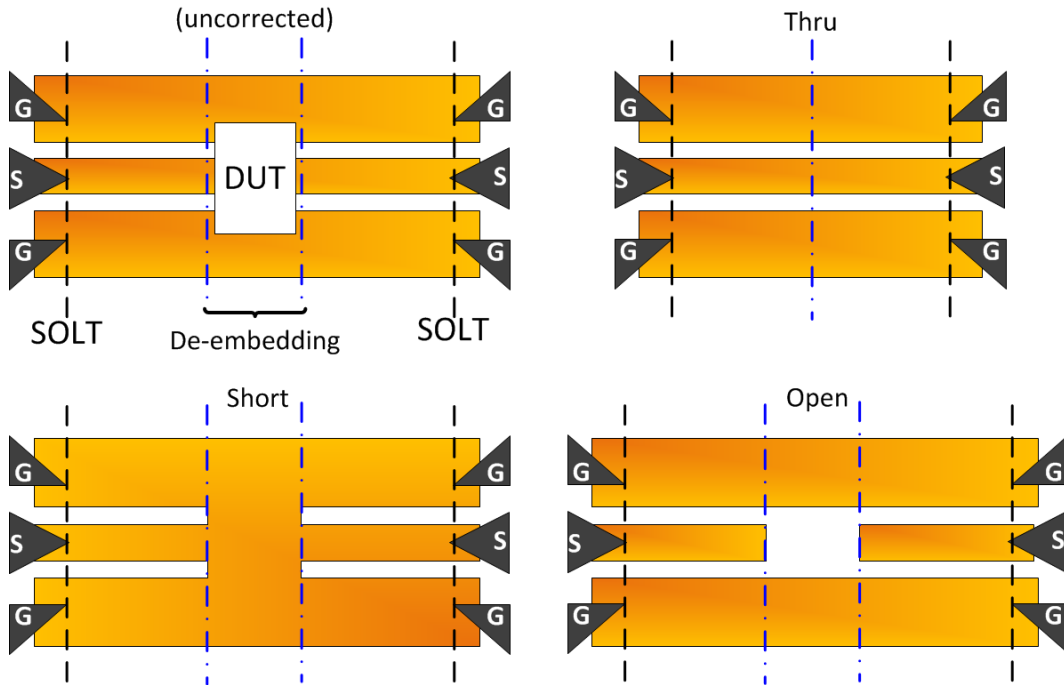


FIGURE 5.1: Standards used for some common de-embedding techniques. On the tips of the GSG probes are the SOLT reference planes (black dashed lines), while the de-embedding reference plane are defined by the standards (blue dash-dotted lines).

To overcome this limitation two strategies are typically applied at the same time: the fabrication of known deembedding standards on the same wafer of the device; and, as stated before, the design of well  $50\ \Omega$ -matched access lines. The former allows applying mathematical methods to shift the reference plane to a point closer to the Device Under Test (DUT), eliminating the phase delay and most, if not all, of the mismatch and ohmic losses associated to access lines; the latter supports a better handling of the dynamic range of the measurement instrument (typically, but not limited to, 50 dB for a VNA) and minimizes the impact of the error associated to the de-embedding of the DUT after the measurement of the standards.

In Fig. 5.1 a hypothetical DUT together with some de-embedding standards is shown. The vertical dashed lines correspond to the reference planes of the measurement according to the Short-Open-Load-Thru (SOLT) calibration, done with a separated calibration kit on alumina and widely adopted alone or as the first of a two-step calibration protocol: it allows removing the effects of the cables, probes and of the instrument itself. The vertical dash-dotted lines correspond to the de-embedding planes defined by the known standards. Various techniques exist, among which the most commonly adopted are the Open-Short and Thru-Reflect-Line (TRL, which includes a delay line standard not shown in the figure). After the de-embedding, the access lines are virtually removed from the DUT.

For mm- and sub-mm wave devices the *intrinsic* FOMs are often considered of greater impact than *extrinsic* FOMs and other design parameters like device footprint. Even though de-embedding procedures are extensively applied and refined, the graphene/metal contact parasitic can deeply affect not only the extrinsic but also the intrinsic FOMs if they are not correctly removed. The Open-Short de-embedding procedure is typically applied to semiconductor device measurements [3], but in recent literature on graphene devices it is not clear whether the graphene/metal contact resistance is removed from presented data. However, a study of its effect at high frequencies, where those devices operate, is in any case necessary.

## 5.2 Objectives of the study

The main objective of this chapter is the building of a low-loss test bed for the RF characterization of monolayer graphene and other thin films of carbonaceous materials. This substrate must provide a set of de-embedding standards and reference devices for the extraction and isolation of the test material's impedance. This test bed must support the following two experiments.

**High-Frequency TLM.** The extraction of the contact and bulk impedance of a test material, in particular monolayer graphene. A set of two-port RF access lines must be built, and the separation between the two central electrodes must be varied across the set. This should allow the linearization of the DC contact resistance over contact separation, and the simultaneous measurement of contact impedance  $Z_C(\omega)$  for each device.

**Nanocontacts.** The development of a model relating  $Z_C(\omega)$  with nanoscaled contact lengths. A set of two-port access lines with various sub-micrometric contact lengths must be built. The new model should provide the minimal contact length to achieve the saturation of  $Y_C(\omega)$  for a given frequency.

### 5.2.1 Design Specifications

The specifications for the test bed were defined as follows:

- G-S-G landing pads for coplanar RF probes; they should support probe pitches of 100 and 150  $\mu m$ ;
- the CPW lines should have a characteristic impedance of  $Z_0 = 50 \Omega$ ;
- the electrical length of the material under test should be less than  $\lambda/10$  up to 110 GHz;
- the reference de-embedding plane should be 50  $\mu m$  farther than the CPW taper, to allow the dissipation of higher-order modes excited by the geometrical discontinuity.

- the typical size of a flake of monolayer graphene is expected to be larger than  $10 \times 25 \mu\text{m}$ , and it should cover entirely the CPW line width;
- the minimum feature size of Contact Optical lithography is  $1 \mu\text{m}$ ;

## 5.3 Method

During the design of the test bed, a considerable effort was devoted to the selection of the substrate. In the structures of Chapter 4, a consistent amount of the losses originated from the silicon substrate. Doped Si-n+ offers a capacitively-coupled low-impedance path to ground for high-frequency signals. In addition to that, the Si/SiO<sub>2</sub> interface induces a layer of charges that can act in the same way, and generate substrate losses. In particular this phenomenon is only weakly related to the conductivity of the semiconductor, and High Resistivity Silicon (HRS) bears the same issue. A complete design on HRS was initially made, fulfilling the specifications contained in § 5.2.1; The layout of a  $100 \mu\text{m}$  is shown in Fig.5.2. This design was fabricated and measured as a reference, but was abandoned due to high RF losses. It will not be further described in this manuscript. However, before the design based on HRS was fabricated, the choice went for a plastic substrate. Benzocyclobutene (BCB) was selected for its interesting properties in RF: low  $\epsilon_r$  and low loss tangent [4], both resulting in low line losses. Then, another requirement was added: the reduction of graphene's contact resistance by preventing contamination of graphene, in particular of its face turned towards contact metals. One obvious source of contamination was the resins (among them, PMMA) used for the lithographic patterning of graphene and the lift-off processing of the CPW line metals. Those resins are normally removed with solvents, but due to their strong adhesion to graphene some residues are left, polluting the graphene/metal interface [5] and reducing the effective contact surface. Moreover, if the graphene is CVD grown, a prior step is necessary to transfer graphene to the target substrate: PMMA polymer is spun on top of graphene, the catalyst metal is etched (for Cu, ferric chloride is used), and the freed graphene/PMMA bilayer is transferred on the substrate of choice. Transfer PMMA is dissolved with solvents, but again some residues can be left on graphene. Recently, some advances have been made on graphene cleaning techniques, like vacuum annealing [6], or the use of sacrificial layers (aluminum oxide) on CVD graphene prior to PMMA spinning [7].

### 5.3.1 Technology

Silicon and plastic technologies are fabricated with very different processes and will be both detailed in this section.

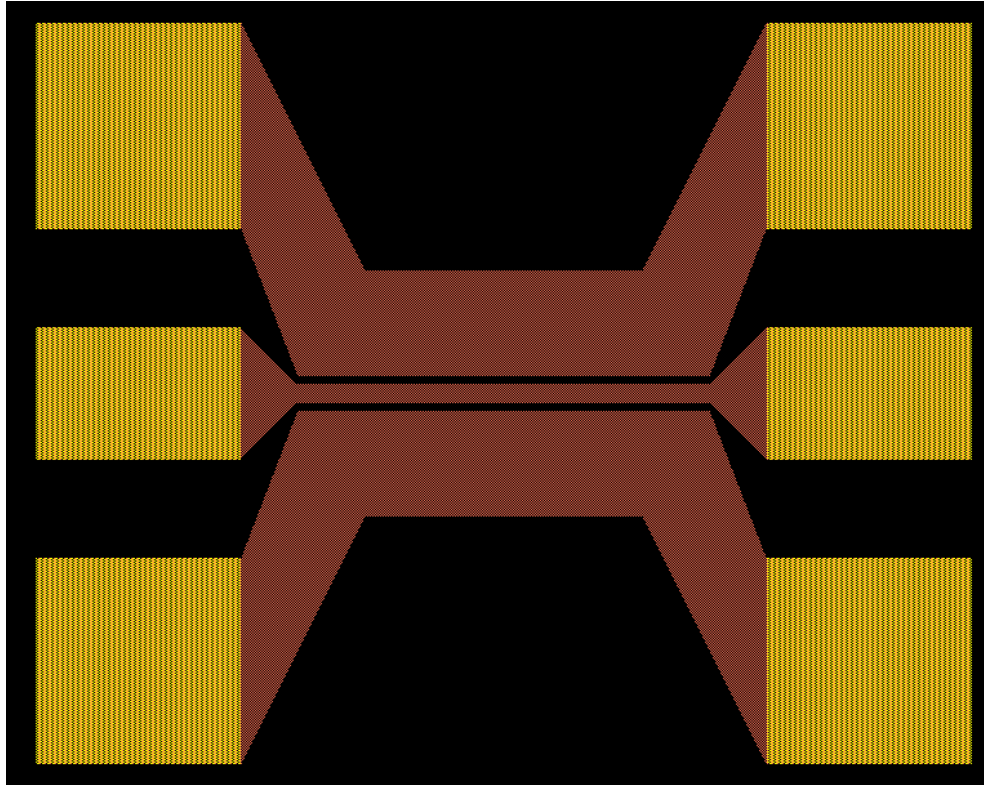


FIGURE 5.2: The layout of a  $100 \mu\text{m}$  line designed for High Resistivity Silicon. The dimensions of the inner CPW are  $S = 9 \mu\text{m}$  and  $G = 4 \mu\text{m}$ .

### 5.3.1.1 Fabrication of CPW on SiO<sub>2</sub>/HR Silicon

Optical lithography was used to pattern the Coplanar waveguide structures on SiO<sub>2</sub>/HR Silicon. The substrate was High resistivity and the SiO<sub>2</sub> thermally grown 290 nm (tuned to enhance the optical contrast of graphene layers). Metals were deposited by electron gun evaporation and were usually comprised of a thin ( $\sim 2\div 5$  nm) layer of adhesion metal (Chromium or Titanium) and then a thick ( $\sim 300$  nm) layer of Gold. Lift-off was used to remove the excess metal. In case nano sized patterns were necessary, E-beam lithography using positive resin (PMMA) was used to define the electrode shape and lift-off was used with a metal thickness of  $\sim 100$  nm to allow narrow patterns to be realized. In Fig. 5.3 this process is shown. The polymer residues interfere with the surface quality needed by metal contacts.

### 5.3.1.2 Fabrication of CPW on Polymeric substrates

This technology takes advantage of the solution proposed by Dr. Deligeorgis, substantially modifying the vertical stack order of metal contact and graphene. The second fabrication method used was as follows: Initially a temporary substrate (Silicon or preferably GaAs) was used to deposit the CPW as described above. Nanosized parts

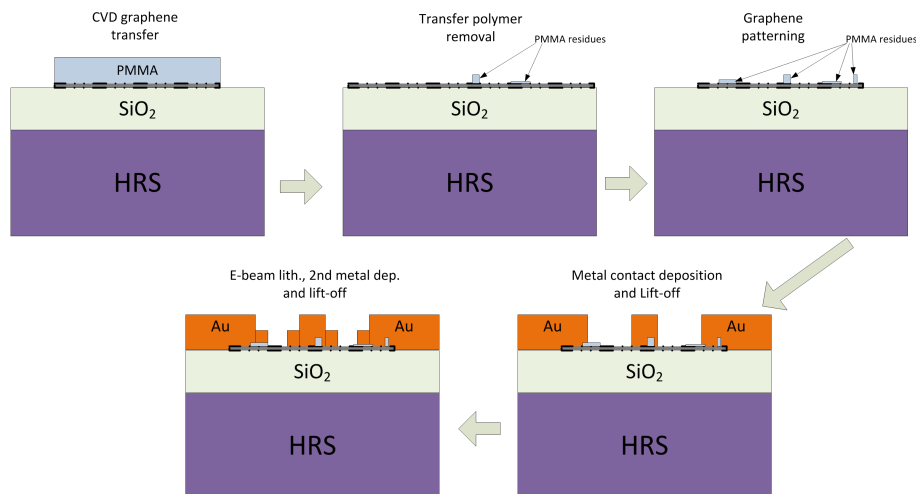


FIGURE 5.3: Graphene on HRS, process steps.

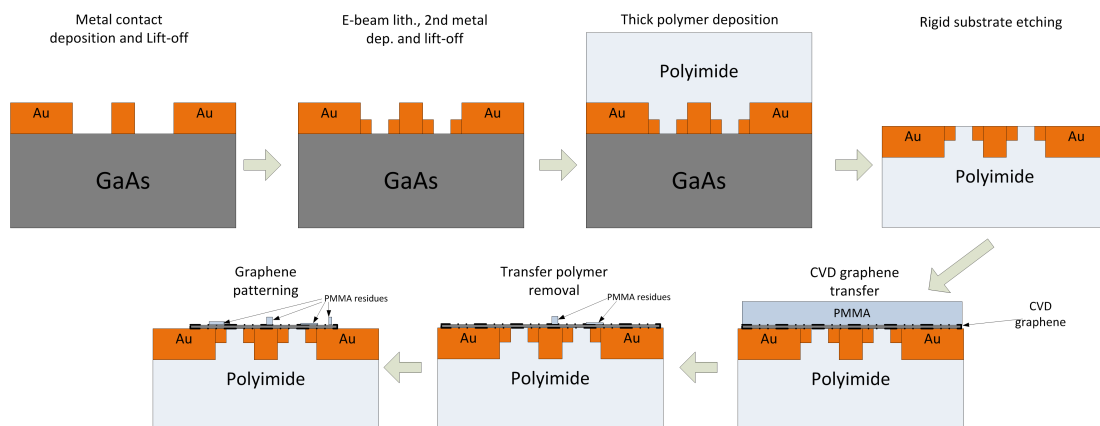


FIGURE 5.4: Graphene on Polyimide, process steps.

were added using electron beam lithography. It should be noted that the deposition was modified to contain an adhesion layer at the top side as well. So an example of the final deposition was: Cr/Au/Ti. The final layer was added to increase adhesion with the polymeric layer deposited afterwards. Following the completion of the CPW structure, a thick ( $\sim 100 \mu\text{m}$ ) polymeric layer (SU-8 or Polyimide) was spin coated on top of the structures. After polymerization by UV exposure and thermal treatment to stabilize the polymer layer, the rigid substrate was etched away. A Lapping step to reduce the substrate thickness from  $\sim 500 \mu\text{m}$  down to  $100\text{-}200 \mu\text{m}$  was initially used. Following that, plasma or wet etching for the Silicon and the GaAs case were used respectively. The resulting polymeric layer containing the CPW structures was used to deposit the carbon material. In the case of CVD graphene, this is deposited on pre-patterned metal lines, freed from the transfer polymer and then cut in the desired shape. The topmost surface of graphene is exposed to transfer and lithographic polymers, whereas the bottom one, which is in direct contact with metals, is left uncontaminated. In Fig. 5.4 the process is detailed. In Fig. 5.5 a photograph of the fabricated PI sample demonstrating

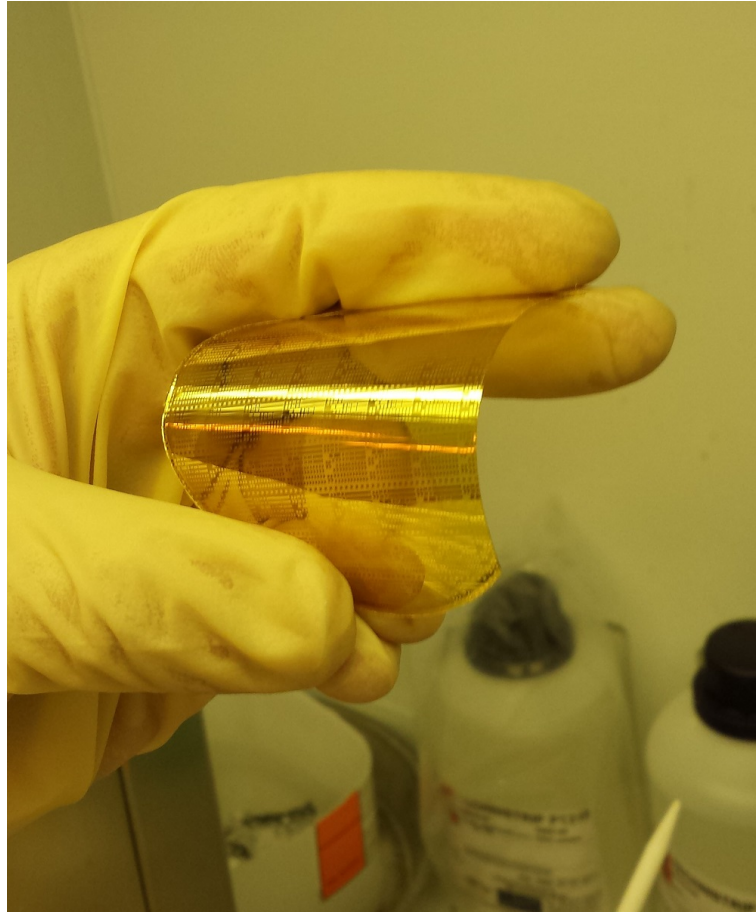


FIGURE 5.5: A photograph of the Polyimide (PI) sample demonstrating its mechanical flexibility.

its mechanical flexibility is shown.

### 5.3.2 Design

Apart from the specifications, some design choices were also outlined to improve the robustness of the design. For the High-Frequency TLM experiment, the circuit connections *series* (between the two signal lines) and *shunt* (between signal and ground, symmetrically) were considered. The matching of the lines to  $50\ \Omega$  was constrained by two parameters: the total CPW line width should be below  $25\ \mu\text{m}$ , and the lithographic resolution of  $1\ \mu\text{m}$ , very close to the gap that would be necessary. Deviations of fractions of micrometer are expected for contact optical lithography from the designed mask and fabrication. To comply with that, larger electrode separations are generally used, but this was not possible because of the CPW total width limit. Also, a preliminary test with lines with different electrode separations can be done, but it would have required an additional optical mask to be fabricated. Instead, two device sets, called G10 and G15, were designed with increased CPW total width: one with a specified gap of  $1\ \mu\text{m}$  and

Line [ $\mu m$ ]	f @ 20° [GHz]	f @ 160° [GHz]
4500	2.7	21.9
1500	8.2	65.7
500	24.6	197.2
300	41.1	328.7
100	123.2	986.0

TABLE 5.1: TRL Line standards and their frequency range.

another one with a  $1.5 \mu m$  gap, and the corresponding signal line width was calculated to have  $Z_0 = 50 \Omega$ .

For each CPW line set a TRL de-embedding standard has been designed. Seven standards, including one Short, one Thru and five lines of different lengths are implemented; all of them have the same access line geometry in common up to the reference plane, in the same fashion as shown in Fig. 5.1. In the TRL algorithm, each Line standard can provide a correct sample of the propagation constant  $\gamma$  when its phase delay is roughly between  $20^\circ$  and  $160^\circ$ . For a BCB substrate,  $\epsilon_r = 2.65$ , the five Line standards together with their lowest and highest frequency are presented in Table 5.1. For the Nanocontacts experiment, only the shunt topology has been chosen: five thin signal lines, having a length of  $6 \mu m$  and a width varying from 100 nm to 350 nm. Finally, Van der Pauw devices for Hall mobility measurement and two large CPW lines (700 and 1200  $\mu m$  long and a constant width of 80  $\mu m$ ) have been added to the design. In Fig. 5.6 the layout of the optical mask period, including all device groups, is shown.

### 5.3.2.1 Modeling

The EM modeling of the CPW was performed in two major steps: first the characteristic impedance of the CPW lines was matched to  $50 \Omega$  through a number of tools, namely quasi-static analysis, ADS Linecalc and HFSS; then the layout was defined through 2.5D MoM simulations in Agilent ADS Momentum.

The quasi-static analysis is based on the conformal mapping of the cross-section of the CPW into a simpler geometry (a parallel-plate capacitor), enabling the computation of the fringing electric fields between signal and ground electrodes and the  $Z_0$  of the line. It is based on a number of assumptions: the metallization has a zero thickness; the dielectric constant of the substrate is real, i.e. with zero DC conductivity and zero  $\tan\delta$ ; and finally the boundary between dielectric and air is a magnetic wall, so that the  $C_{air}$  and  $C_{diel}$  can be separated and the total capacitance is the sum of the two partial capacitances. In particular, the case for a double layer substrate, a stack of BCB (75  $\mu m$  thick,  $\epsilon_r = 2.65$  [4]) and glass (infinite thickness,  $\epsilon_r = 3.9$ ), has been implemented as

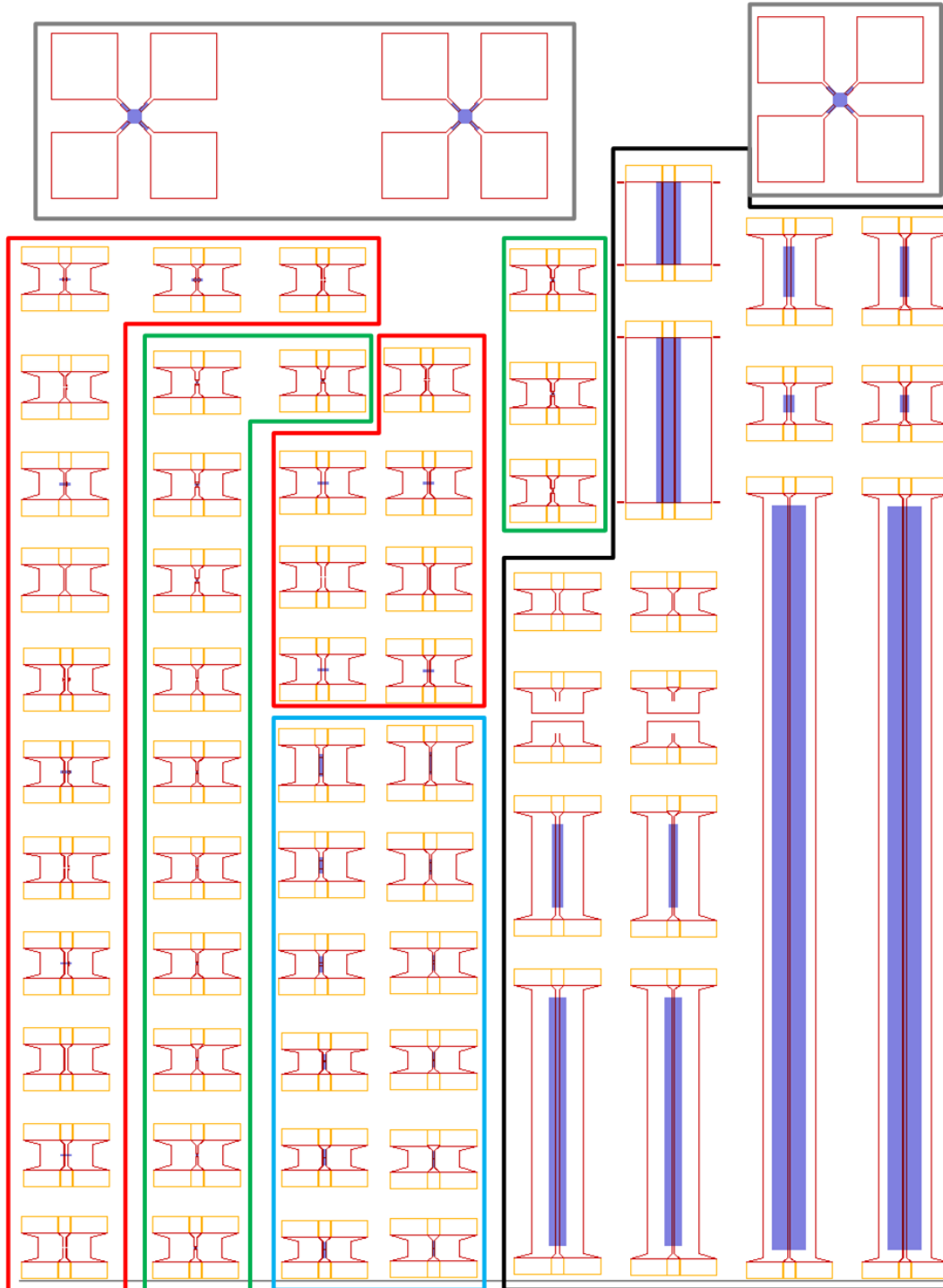


FIGURE 5.6: Layout of the full period. Outlined in black is the group of TRL and line standards; in grey are the Van der Pauw devices; in red are Shunt devices with their short-circuited references; in green are the Nanocontact devices and in light blue are the Series devices. The mask layout contains both G10 and G15 subgroups for every device group, with the exception of the Van der Pauw and two line standards.



Parameter	Analytical	LineCalc	HFSS
BCB $\epsilon_r$	2.65	2.65	2.65
BCB thickness [ $\mu\text{m}$ ]	75	1000	75
BCB $\tan\delta$	N.A.	0.0008	0.0008
SiO <sub>2</sub> $\epsilon_r$	3.90	N.A.	3.90
SiO <sub>2</sub> thickness [ $\mu\text{m}$ ]	inf.	N.A.	1000
SiO <sub>2</sub> $\tan\delta$	N.A.	N.A.	0.0050
Au thickness [nm]	N.A.	300	300

TABLE 5.2: List of material parameters for the computation of  $Z_0$ .

Set	G	Analytical	Linecalc	HFSS	Final design
G10	1.0	16.25	12.15	14.00	14
G15	1.5	24.52	20.90	21.50	22
Pads	4.5	70.81	75.84	69.50	71

TABLE 5.3: Signal widths  $S$  obtained from the three tools used, expressed in  $\mu\text{m}$ , and their averaged value used in the design.

in § 2.2.6 of [8] in a Matlab script. Unfortunately, this analysis lacks the effect of the dispersion over frequency of the quasi-TEM mode and, in addition to that, for ratios of signal width over separation  $S/G \gg 5$  this computation is less accurate. Finally, when the thickness of the metals is comparable to the gap, the assumption of infinitely thin metals can underestimate the line capacitance and overestimate the  $Z_0$ .

The second tool used was ADS Linecalc, which is a commercial tool based on conformal mapping. It includes a Svensson/Djordjevic Model to take into account the loss tangent of the dielectric [9], but it doesn't support multi-dielectric substrates. A simpler model with a single material substrate has been selected with this tool. Finally, the  $Z_0$  was also computed in HFSS, a full-wave 3D finite elements EM simulator. As opposed to the analytical computation, HFSS takes into account the dispersion of the line and the resulting  $Z_0$  is thus a function of the frequency. In Table 5.2 a list of the parameters used in each tool is shown. These are the nominal values of thickness and dielectric properties for the process described in § 5.3.1. The signal width  $S$  for the two sets G10 and G15 that resulted in  $Z_0 = 50 \Omega$  for each tool are presented in Table 5.3, together with the  $S$  and  $G$  for the larger probe-landing section of the CPW. The final design values are obtained as an average of those proposed by the three tools, rounded to one micrometer precision.

The preliminary layout based on the specifications in § 5.2.1 has been drawn and simulated in ADS Momentum. The taper connecting the landing pads to the narrower line was found to contribute significantly to the signal reflection. The taper should not provide impedance adaptation, since the  $Z_0$  of both its ends is  $50 \Omega$ , so a smooth width adaptation would be expected to give the lowest signal reflection. However, the best

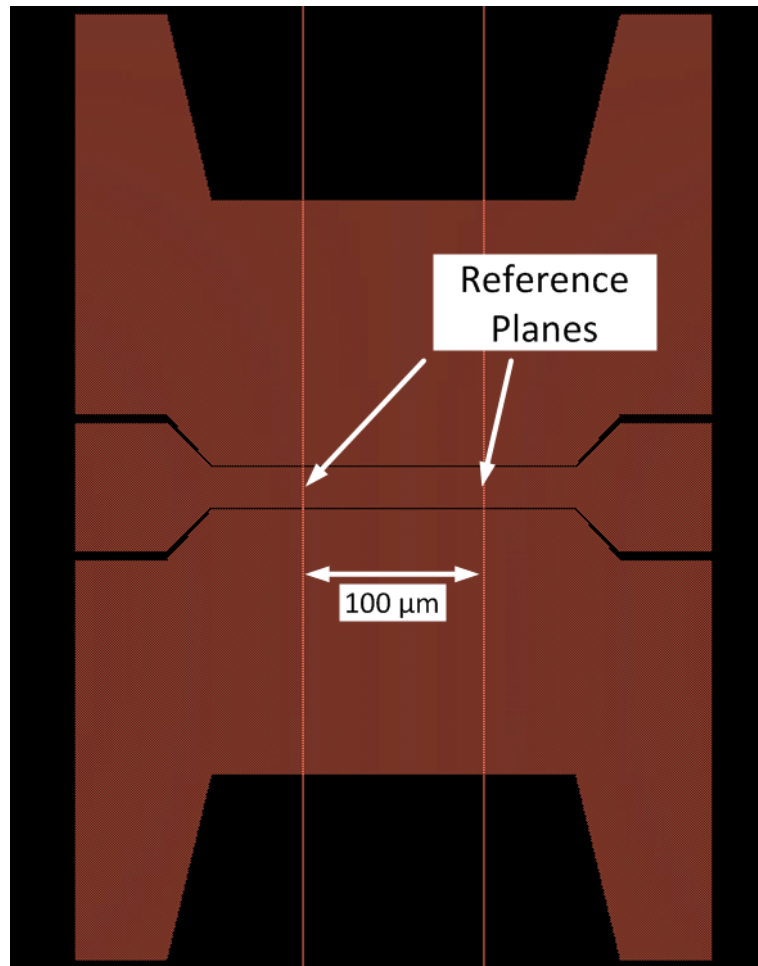


FIGURE 5.7: An example of the final layout made in Agilent ADS, showing the  $100\ \mu\text{m}$  line standard for the G15 set. The landing pads and access lines are identical for every device in the G15 set. The device comprised between the two vertical lines is the intrinsic DUT.

performance was obtained with a  $45^\circ$  connection, which is also beneficial to keep both the size of the access lines and related ohmic losses small. The reference plane was finally designed to be  $50\ \mu\text{m}$  farther than the taper to allow the dissipation of higher-order modes excited by the line discontinuity. The  $100\ \mu\text{m}$  line standard is shown in Fig.

The simulated S-parameters for the  $100\ \mu\text{m}$  line, from both G10 and G15 sets, is shown in Fig. 5.8. Higher ohmic losses are expected for the G10 set because of the narrower signal line width ( $14\ \mu\text{m}$ ) compared to the G15 set ( $22\ \mu\text{m}$ ).

The dynamic range of test impedances that resulted from these test beds was also studied. Each test device of the High-Frequency TRL experiment has two reference devices: an Open without graphene, and a Short with all electrodes contacted together. Line standards are also available from the TRL kit. The DC resistance of access lines is  $0.612\ \Omega$  for  $22\ \mu\text{m}$  wide and  $300\ \text{nm}$  thick signal lines. This should sum up with about  $2\ \Omega$  of DC resistance for cables, probes and contact. In the case of high resistances this

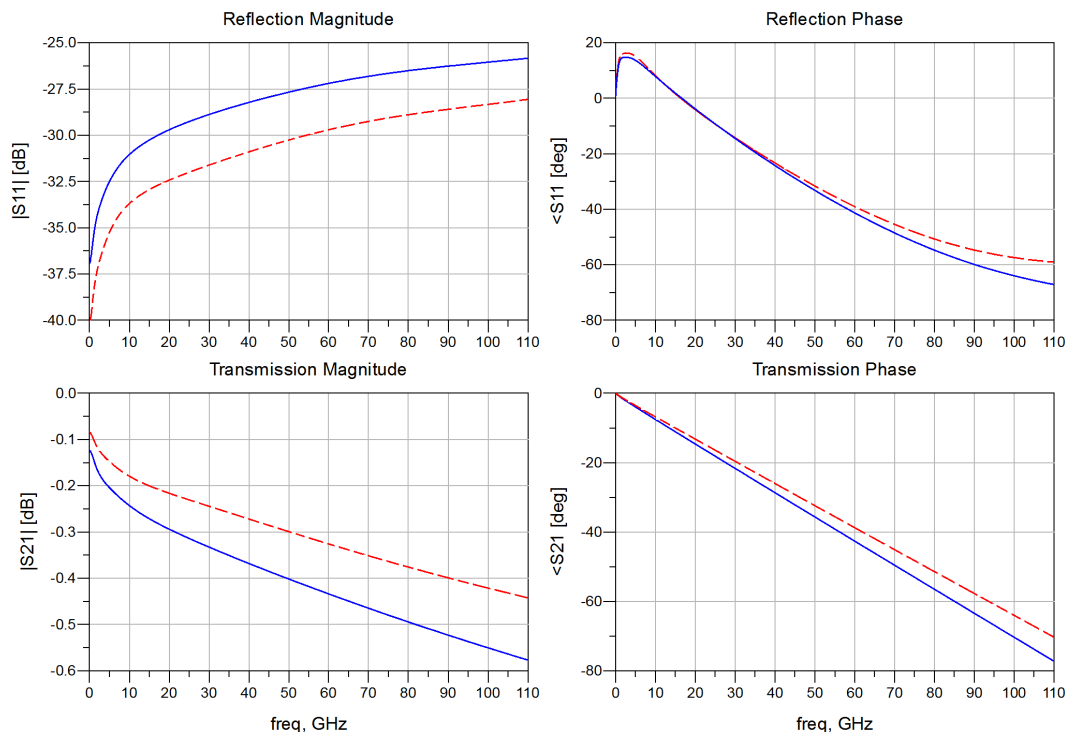


FIGURE 5.8: The 100  $\mu\text{m}$  line in Fig. 5.7 (red line) and its equivalent in the G10 set (blue line) simulated in MoM (ADS Momentum). The transmission magnitude is lower for the G10 device because of the smaller CPW line width and signal line width (14  $\mu\text{m}$ ).

quantity can be neglected, while for low resistances a multimeter with precision, for example, of 5.5-digits would allow to measure resistances of the order of 10 m $\Omega$ . However, contact repeatability would represent the highest obstacle in the low-R scenario.

In RF, well matched and well designed access lines give very high ratios between the transmission (and the reflection) of the Open and Short references. In Fig.5.9 the  $|S_{21}|$  ratio between the Open and Short reference is plotted in blue for a 1  $\mu\text{m}$  Shunt gap, and the  $|S_{21}|$  ratio for the Open and the Line references of a 100  $\mu\text{m}$  Series gap is plotted in red; values higher than 30 dB on the whole bandwidth suggest that a wide dynamic range of test impedances can be read.

### 5.3.3 Fabricated structures

The fabrication of the devices was fulfilled by Dr. Deligeorgis. A number of issues arose during the development of the technology. The ones whose correction affected the final design are listed here. The BCB plastic substrate demonstrated very low adhesion to both the supporting SiO<sub>2</sub> and metal lines. This made the landing pads mechanically unstable and very prone to scratching, piercing and detachment by the action of RF probes (in some cases the entire signal line was seen to raise from the

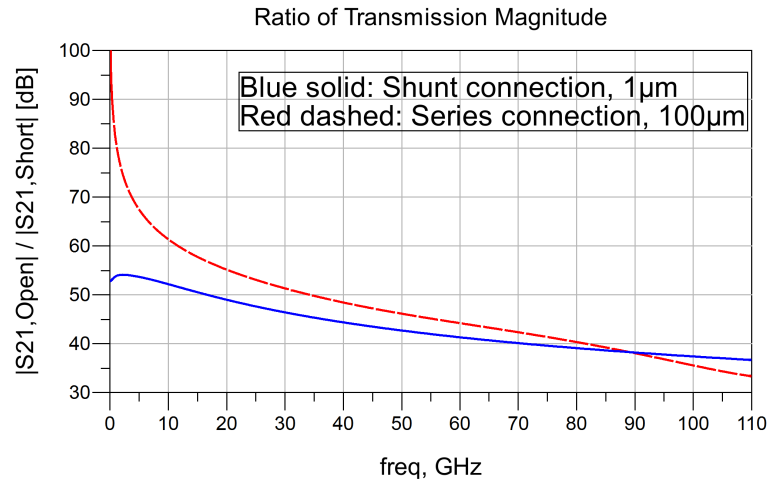


FIGURE 5.9: The ratio between Open and Short transmission for the Shunt device (blue line, calculated as  $\text{dB}(\text{Open}) - \text{dB}(\text{Short})$ ) and between the Open and Line transmission for the Series device (red line, calculated as  $\text{dB}(\text{Line}) - \text{dB}(\text{Open})$ ), simulated in MoM (ADS Momentum). The electrode separation is respectively 1 and 100  $\mu\text{m}$ .

substrate and eventually detach). The BCB polymer was then replaced with SU8, which has much better adhesion but unfortunately has higher RF losses ( $\tan\delta$  around 0.04 instead of 0.005) and a different dielectric constant (estimated as  $\epsilon_r = 2.85$  in both this work and [10]). This implicates a considerable mismatch of the lines from the designed characteristic impedance, increasing the line capacitance by 7.5% and lowering the  $Z_0$  by  $1.7\Omega$ .

On the other hand, the SU8 substrate was found to constrict slightly after the baking step, with a difference to nominal dimensions of below 0.5%. This had practically no consequences on the electrode separation, but prevented the correct alignment of optical masks on the 4" wafer. Patterning of graphene, which in this technology is the last step, had a very low yield. SU8 was then replaced with Polyimide (PI) which gave lower constriction than SU8. The dielectric constant of PI is even higher than SU8: a value of  $\epsilon_r = 3.3$  was given in [11], and a value of  $\epsilon_r = 3.4$  was estimated by MoM simulations in Fig. 5.14. This resulted in a parallel-plate component of the line capacitance 25% higher than BCB, and a  $Z_0$  estimated  $4.0\Omega$  lower than BCB.

The accuracy of the lithography was also a concern of difficult evaluation. The most influent features as the Signal-Ground separation, the Signal-Signal gap of Series devices and the width of the signal lines in the Nanocontacts experiment cannot be measured with optical microscope because they all are of the same order or smaller than the optical wavelength. Moreover, the top profile is perfectly flat and topography with AFM would give no appreciable data. Finally the substrate is insulating and, during SEM imaging, electrons cause the metallic lines to charge up, deviating further incoming electrons and making the image blurry and oscillating. Sample preparation with gold pulverization

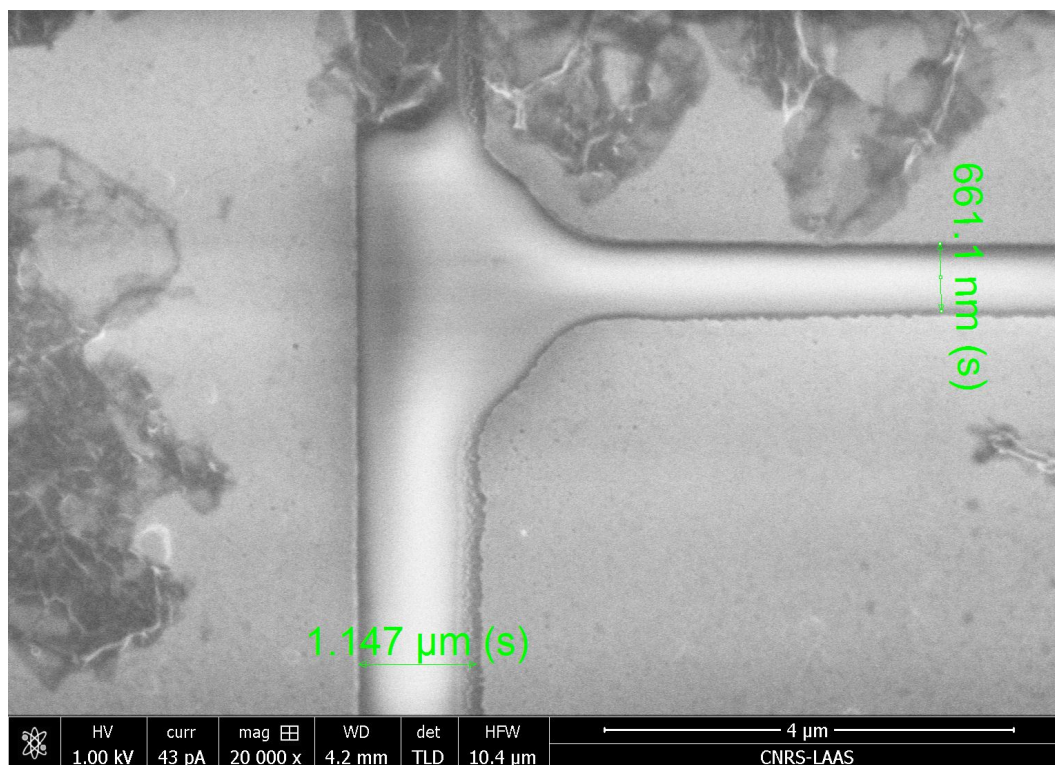


FIGURE 5.10: Low-voltage SEM scan of the electrode separation as fabricated in SU8 sample. The image represents a series capacitance with a nominal signal-to-signal gap of  $1\ \mu\text{m}$  ( $0.66\ \mu\text{m}$  measured) and a signal-ground gap of  $1.5\ \mu\text{m}$  ( $1.15\ \mu\text{m}$  measured).

would than made the material underneath unrecognizable and again no information would have been retrieved by the flat topography.

The measure of these small but important features was not possible until August 2013, when the newly available dual beam microscope FEI Helios 600i allowed scans with voltages lower than 1 kV. This, together with a reduced time of scan and software image stabilization, limited the charge accumulation and the image blurring. The measure in these conditions showed evidence of a resin development issue during the lift-off of the CPW access lines on the SU8 sample: the nominal electrode separations are reduced of  $350 \pm 50\ \text{nm}$ , as can be seen by the SEM scan in Fig. 5.10.

The PI sample was also analyzed at low-voltage SEM. The electrode separation for that run is in average reduced of  $170 \pm 60\ \text{nm}$ , as shown in Fig. 5.11. This increases the parallel-plate component of the signal-ground capacitance up to the 54% for the SU8 sample and 25% for the PI one. The consequent reduction on  $Z_0$  can be evaluated as, at worst,  $6.1\ \Omega$  for SU8 and  $2.7\ \Omega$  for PI.

Finally, the nominal thickness of the metal has been increased from the initial value of 300 nm for two reasons: for better resilience against scratches from the RF probes, and for improved ohmic losses. The adhesion layer between the metal and the plastic was

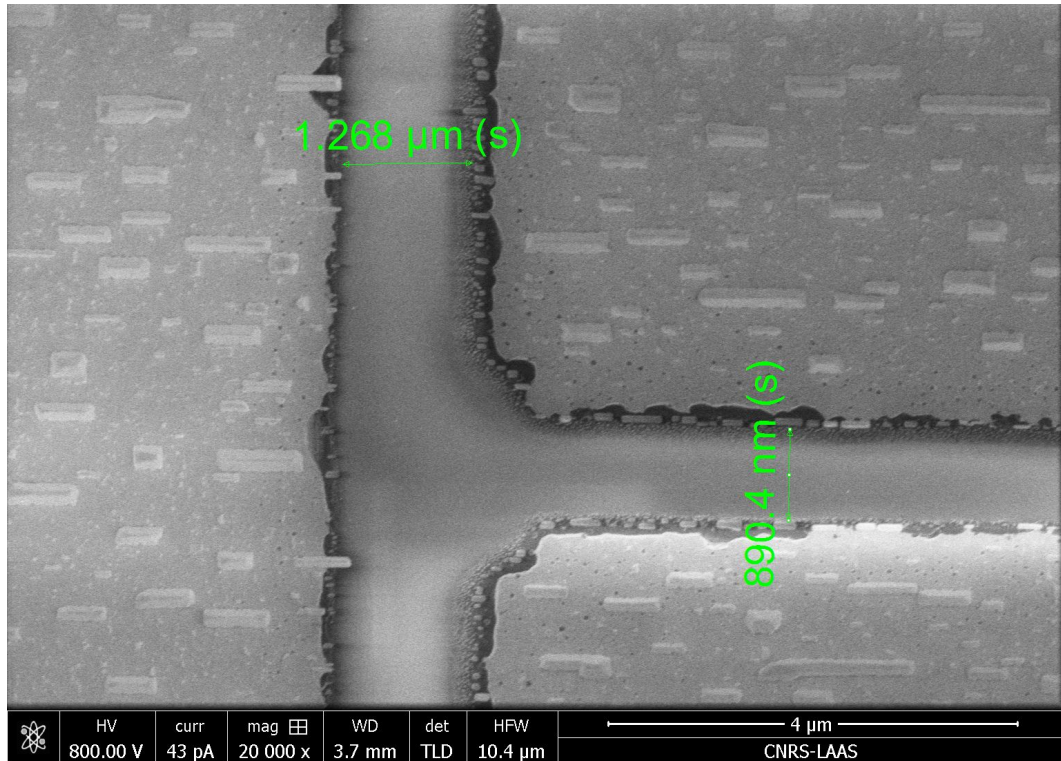


FIGURE 5.11: Low-voltage SEM scan of the electrode separation as fabricated in Polyimide sample. The image represents a series capacitance with a nominal signal-to-signal gap of  $1 \mu\text{m}$  ( $0.89 \mu\text{m}$  measured) and a signal-ground gap of  $1.5 \mu\text{m}$  ( $1.27 \mu\text{m}$  measured).

also improved, which made the landing pads much more robust. A final value of  $330 \text{ nm}$  for the SU8 run was extracted: 2-point DC measurement of lines of different length were subtracted together to de-embed the effect of DC probes and contacts. Although 4-points measurements would have given a more accurate value, they were not used in order to avoid excessive damage on the reference structures. A side-effect of higher metal thickness is the increase in the parallel-plate component of the line capacitance;  $30 \text{ nm}$  thicker metal lowers the simulated  $Z_0$  of  $0.31 \Omega$ . For the Polyimide run, the DC measurements gave a thickness of  $120 \text{ nm}$ , while RF simulations suggested a value of  $140 \text{ nm}$ . This was highly detrimental for losses (shown in Fig. 5.12), which increased to 5% at low frequency and to 11–13% at high frequency. However, the thickness reduction compensated for the many factors that lowered the  $Z_0$ : an improvement of  $1.56 \Omega$  has been computed for this effect.

The cumulated effect on  $Z_0$  cannot be simply derived algebraically, it must be calculated. The final computed values of the  $Z_0$  are  $42.63 \Omega$  in set G10 and  $45.43 \Omega$  in set G15.

All the reference devices without graphene were measured in RF with an Anritsu 37397C VNA with 110 GHz extension mixers, with the exclusion of the HRS sample, measured up to 67 GHz with an Agilent PNA-X VNA. In Fig. 5.13 a comparison between measurements and simulation is done for a  $100 \mu\text{m}$ ,  $300 \mu\text{m}$  and  $500 \mu\text{m}$  lines for the SU8 sample.

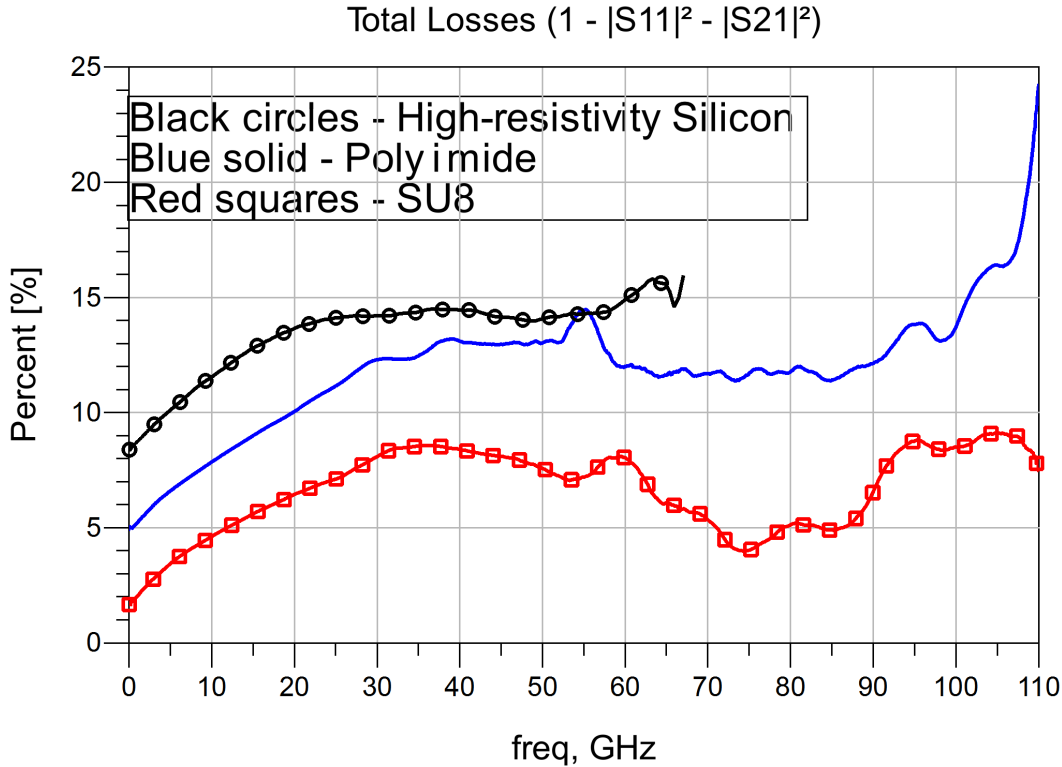


FIGURE 5.12: Total Losses ( $1 - |S_{11}|^2 - |S_{21}|^2$ ) measured for a  $100\mu\text{m}$  line (plus access fixtures) made on HRS (black circles), SU8 (red squares) and Polyimide (blue solid). The peak after 100 GHz for PI is due to inadequate calibration. The lines were designed to be matched on a HRS technology in the first case, and on a BCB technology in the remaining two.

The close fitting of  $|S_{11}|$  and of the phase of  $\angle S_{21}$  to measurements suggested that the permittivity of SU8 should be  $\epsilon_{r,SU8} = 2.85$ , as also reported in [10] for in-house SU8 technology. The fitting of the low-frequency value of both  $|S_{11}|$  and  $|S_{21}|$  resulted in a metal thickness of 330 nm, consistent with DC measurements as stated before. The largest contribution to RF losses was then given by the metals with an attenuation constant of  $\alpha_c = 1.04$  dB/mm at 40 GHz, without access lines and probes. A fitted value of the loss tangent of  $\tan\delta = 0.04$  was also found, consistent with [10].

In Fig.5.14 the same comparison as above is done for the Polyimide sample. The extracted dielectric constant  $\epsilon_{r,PI} = 3.4$  is close to the data provided by the manufacturer ( $\epsilon_r = 3.3$ , [11]), while the loss tangent therein was measured at 2 kHz, a frequency that lies in a range not considered in this study (RF measurements were performed starting from 40 MHz). The extracted value, fitting the RF losses, was  $\tan\delta = 0.035$ . The computed value of  $Z_0$  are  $45.16\Omega$  in set G10 and  $46.52\Omega$  in set G15.

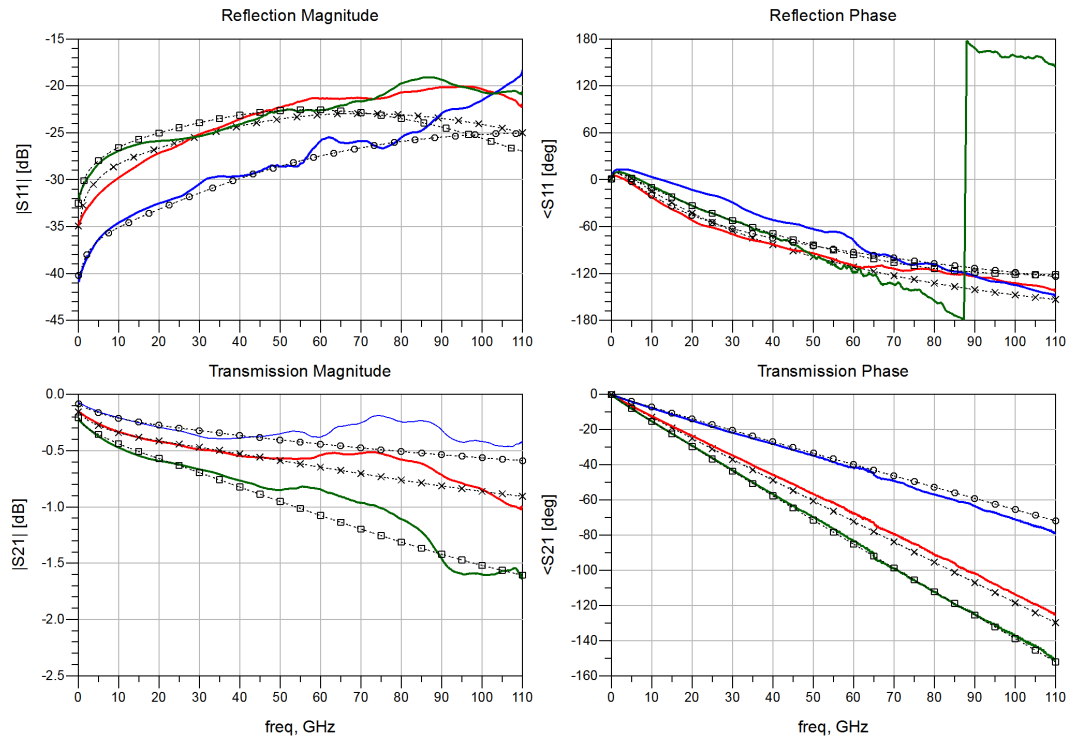


FIGURE 5.13: Measured S-parameters for the G15 set in SU8: the 100  $\mu\text{m}$  line (blue solid), the 300  $\mu\text{m}$  (red solid) and 500  $\mu\text{m}$  (green solid). Simulated S-param for the same structures (respectively, circles, crosses and squares).

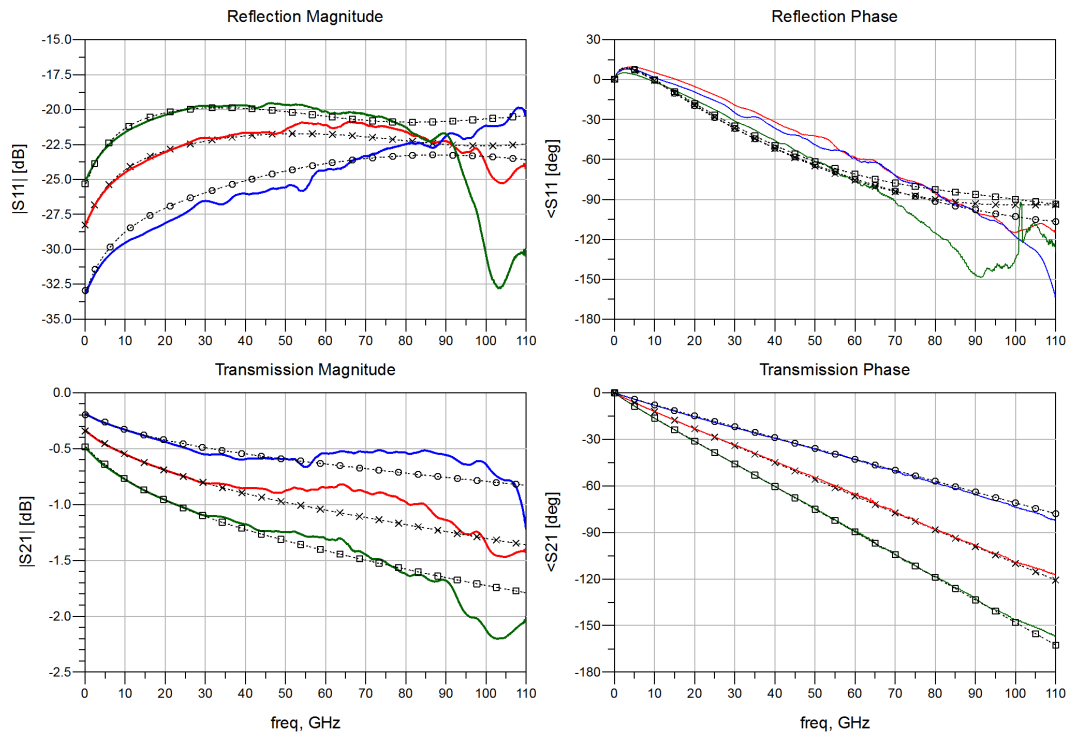


FIGURE 5.14: Measured S-parameters for the G15 set in Polyimide: the 100  $\mu\text{m}$  line (blue solid), the 300  $\mu\text{m}$  (red solid) and 500  $\mu\text{m}$  (green solid). Simulated S-param for the same structures (respectively, circles, crosses and squares).



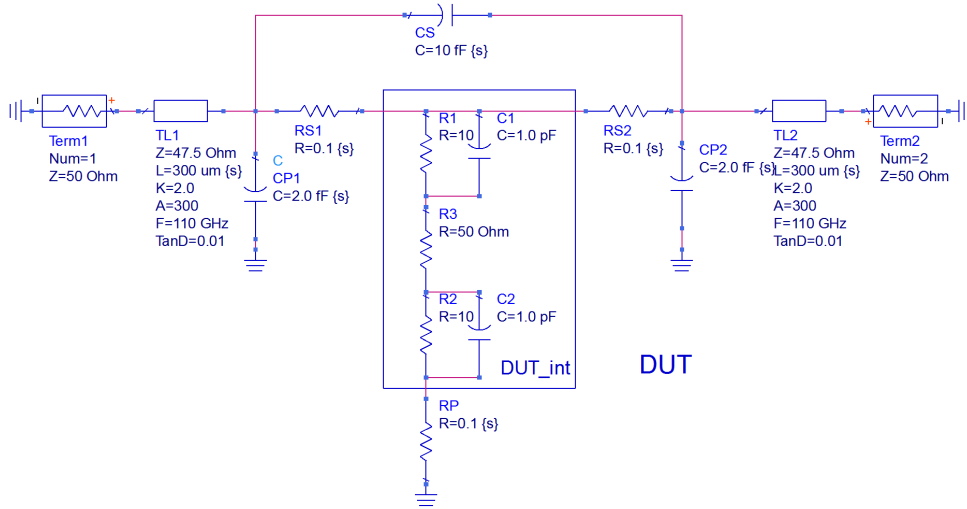


FIGURE 5.15: Test DUT circuit. The framed section of the circuit is the intrinsic device,  $DUT_{int}$ .

### 5.3.3.1 De-embedding

The SOLT (Short-Open-Load-Thru) is one of the standard procedures used for the calibration of VNA. It relies on three known connection standards and a broadband matched load on an Alumina calibration kit, and allows the shift of the reference plane up to the tips of the RF probes. However, to further push the reference plane up to the DUT, a de-embedding procedure is necessary. Many different methods exist, and many of them rely on the fabrication of a high-precision and broadband matched load, which is a complicated process. Other methods do not rely on matched loads, and three of them have been explored and compared: Through-Reflect-Line (TRL), Open-Short and Cascade-Thru.

The test device is a circuitual model drawn in ADS Schematic. A "raw" DUT to be deembedded is shown in Fig. 5.15, containing an internal section  $DUT_{int}$  that is the target of the de-embedding procedure, two slightly mismatched lossy transmission lines at the inputs, and parasitic capacitances and resistances  $C_S$ ,  $C_{P1}$ ,  $C_{P2}$ ,  $R_{S1}$ ,  $R_{S2}$  and  $R_P$ . The Short and the Open standards are built according to the specifications in [3], and the Thru contains all the elements with the exception of the shorting resistor  $R_P$ . The Line standard contains a  $857 \mu\text{m}$  line element with  $\kappa_{eff} = 2.0$ , which has a  $160^\circ$  phase delay at 110 GHz.

The TRL de-embedding procedure is based on the measurement of three connections: a reflection standard, typically a Short, a Thru and Line standards. It allows the extraction of the propagation constant  $\gamma$  of the access line, followed by the reflection parameter  $\Gamma$  [12]. The standards must be perfectly identical up to the reference plane. In addition,

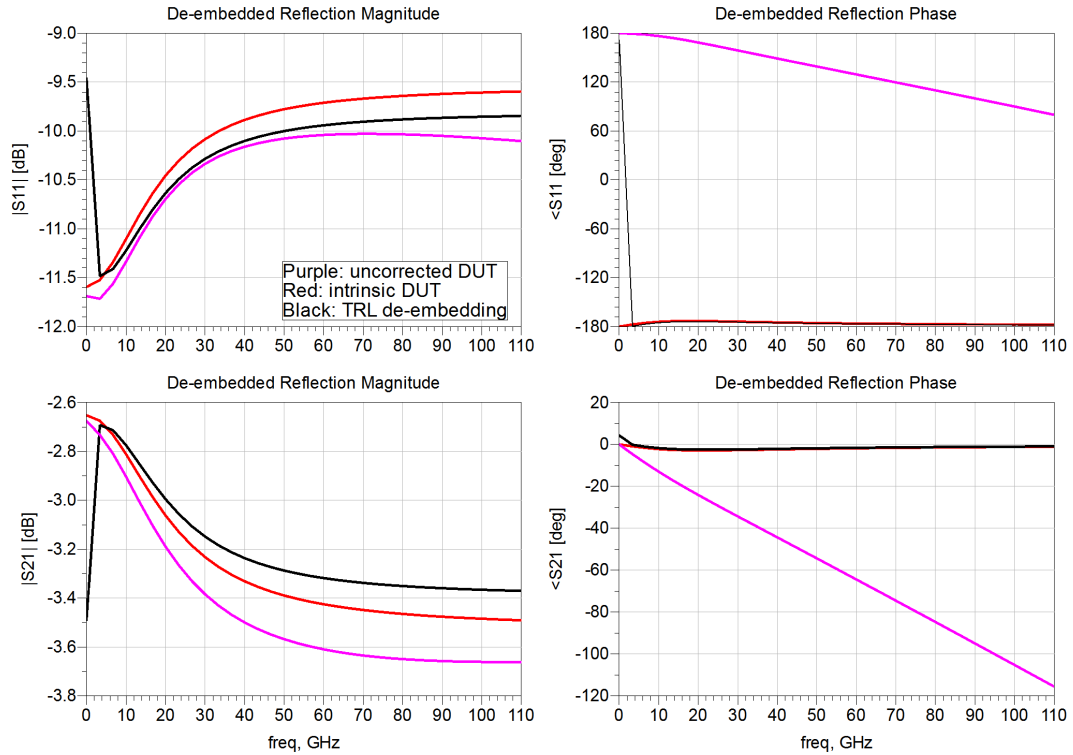


FIGURE 5.16: Comparison between intrinsic model (red), uncorrected data (purple) and TRL de-embedded data (black). S-parameters are shown, Reflection (above) and Transmission (below).

the  $50\ \Omega$  Line standard must have a phase delay between  $20^\circ$  and  $160^\circ$ , as also stated in § 5.3.2. The single-line TRL procedure was implemented in a Matlab script. In Fig. 5.16 the uncorrected and TRL de-embedded data are presented along with the internal model. The lowest frequency point (50 MHz) of TRL corrected data falls beyond the  $20^\circ \div 160^\circ$  phase delay requirement for the Line standard and is not valid.

The Open-Short de-embedding procedure is extensively used in state-of-art graphene device research [13], [14]. The measurements of two standards are needed: the Open, i.e. the DUT without graphene, and the Short, i.e. with all electrodes connected together. In Eq. 5.1 the equation of the Open-Short de-embedding is shown [3].

$$\mathbf{Y}_{\text{int}} = [(\mathbf{Y}_{\text{DUT}} - \mathbf{Y}_{\text{Open}})^{-1} - (\mathbf{Y}_{\text{Short}} - \mathbf{Y}_{\text{Open}})^{-1}]^{-1}, \quad (5.1)$$

where in bold are the Y-matrices of the de-embedded data, the raw data, the Open standard and the Short standard respectively. The effect of this method will be shown in Fig. 5.17.

A variant of the Cascade-Thru de-embedding procedure was also developed. In this method, the device is thought as the chain of a left fixture, the DUT to be deembedded,

and the right fixture. The ABCD parameters of the Thru of each device (its metal-shortened version) are measured, square-rooted, inverted and left- and right-multiplied to the ABCD parameters of the DUT, as clearly described in the next formula.

$$\mathbf{D}_{\text{int}} = \left(\sqrt{\mathbf{T}}\right)^{-1} \mathbf{D}_{\text{raw}} \left(\sqrt{\mathbf{T}}\right)^{-1}, \quad (5.2)$$

where  $\mathbf{D}_{\text{raw}}$  are the measured ABCD parameters of the DUT,  $\mathbf{T}$  those of its reference Thru structure and  $\mathbf{D}_{\text{int}}$  are the de-embedded parameters. The square-root  $\mathbf{R}$  of a matrix  $\mathbf{M} = \begin{pmatrix} a & b \\ c & d \end{pmatrix}$  is instead computed as follows:

$$\mathbf{R} = \frac{1}{t} \begin{pmatrix} a + s & b \\ c & d + s \end{pmatrix} \quad (5.3)$$

with

$$s = \pm\sqrt{\delta} \quad \text{and} \quad t = \pm\sqrt{\tau - 2s}, \quad (5.4)$$

and  $\tau$  and  $\delta$  are respectively the trace and the determinant of  $\mathbf{M}$ . Two solutions exist for the square root of the matrix of a generic delay line (other two are identical to the first pair). However, one of them is unphysical because gives anti-symmetric delays in forward and reverse transmission ( $\angle S_{21}$  and  $\angle S_{12}$  are rotated of  $\pi$  in Smith chart representation).

A general requirement of the Cascade-Thru is that the Thru device has to be reciprocal and symmetrical, which is not always the case because of some small yet unavoidable calibration errors after the SOLT step. This requirement in S-parameter notation translates in a bi-symmetrical matrix, i.e. simultaneously symmetrical around the main diagonal ( $S_{21} = S_{12}$ , reciprocal device) and the secondary one ( $S_{11} = S_{22}$ , symmetrical device). However, every matrix can easily be separated in a symmetrical and anti-symmetrical component with simple average and difference operations. The small imperfections left by the SOLT calibration can be subtracted away and incorporated in the de-embedding error, and the modified Thru reference structure can be assumed as the chain of its square roots. Hence, the  $\mathbf{T}$  matrix in Eq. 5.2 must be the ABCD transform of the bi-symmetrized S-parameters of the Thru. This procedure, although intuitive, has not yet been found in literature in this exact formulation to date. Single-standard Thru-based De-embedding techniques generally decompose the Thru matrix in  $\pi$ - or T-shaped networks and derive the values of their components. The use of Eq. 5.2 is not yet reported, thus it will be soon described in a technical paper.

In Table 5.4 the average errors between de-embedded data and the intrinsic model are presented. The lowest error is found for the Cascade-Thru technique. The Open-Short and the Cascade-Thru broadband methods were also compared with a random variation

TRL	Open-Short	Cascade-Thru
0.021	0.205	0.012

TABLE 5.4: Average errors on the magnitude of S-parameters (linear) for various de-embedding techniques.

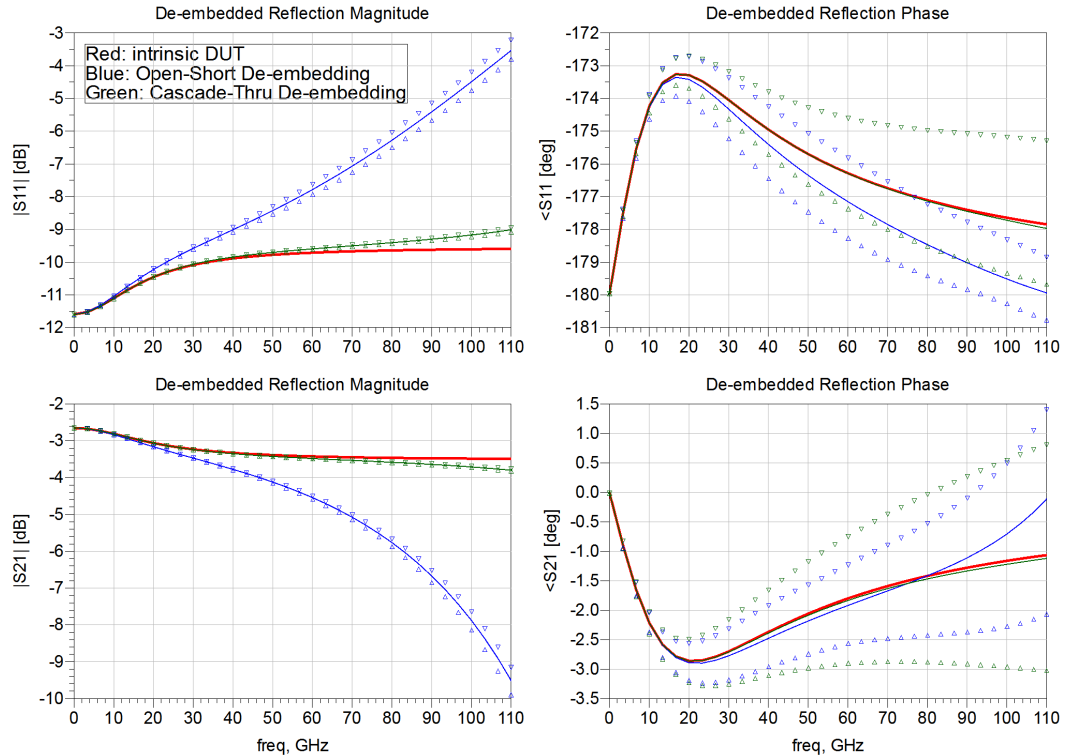


FIGURE 5.17: Comparison between Open-Short (blue solid line and blue up and down triangles), Cascade-Thru (green solid line and triangles) and the target  $DUT_{int}$  (solid red line). S-parameters are shown, Reflection (above) and Transmission (below).

TABLE 5.5: Open-Short and Cascade-Thru de-embedding errors compared at 110 GHz.

Method	$ S_{11}  [dB]$	$ S_{21}  [dB]$	$\angle S_{11} [deg]$	$\angle S_{21} [deg]$
Open-Short	$6.06 \pm 0.32$	$6.02 \pm 0.39$	$2.10 \pm 0.88$	$0.95 \pm 1.96$
Cascade-Thru	$0.59 \pm 0.07$	$0.31 \pm 0.04$	$0.13 \pm 2.67$	$0.06 \pm 1.93$

on the circuit parameters in the standards and in the uncorrected DUT. The variation is described by a Gaussian distribution with 5% of std. dev. amplitude, and a Monte-Carlo analysis has been performed. The resulting S-parameters are shown in Fig.5.17. The output variation of each method is comprised between the top and bottom triangles of the respective color. The maximum errors of Open-Short and Cascade-Thru techniques are listed in Table 5.5. Cascade-Thru performs generally better, although it also gives a larger variation in the phase error compared to Open-Short.

In conclusion, the Cascade-Thru method has been proven as more accurate than both TRL and OS, and more robust against variations in the known standards as far as the

TABLE 5.6: Measured DC resistance values for devices of various separations.

Device	Separation [ $\mu\text{m}$ ]	$R_{dc}$ [ $\Omega$ ]
Srs001	0.85	$272.6 \pm 5.6$
Srs002	1.85	$239.7 \pm 6.7$
Srs020	20.0	$421.4 \pm 4.5$

TABLE 5.7: Extracted contact and sheet resistances .

Device	$R_{dc}$ [ $\Omega$ ]	$R_{\square}$ [ $\Omega$ ]	$R_C$ [ $\Omega \cdot \text{mm}$ ]	$C_C$ [pF/mm]
Srs001	273	2933	1.70	3.73
Srs002	240	1021	1.64	6.40
Srs020	421	251	2.02	0.78

magnitude of S-parameters are concerned.

## 5.4 Results: Graphene monolayer, CVD

CVD monolayer Graphene provided by Graphene Supermarket has been deposited on the Polyimide substrate as shown in Fig. 5.4. Similarly to SU-8, the PI too suffered some constriction after the curing step, estimated as  $< 0.4\%$ . This prevented the correct alignment of the graphene patterning shapes during the optical lithography step. Furthermore, in some spots graphene was missing. Three devices were correctly patterned and working, all of which of the Series kind and with electrode separations respectively of 1, 2 and 20  $\mu\text{m}$ .

S-parameter measurements were performed with an Agilent PNA-X up to 67 GHz and with a Keithley 2410 SMU connected on the DC feeds of the VNA. In order to avoid any non-linear effects of the graphene conductivity versus DC bias and RF power, both measurements were conducted at low power. The VNA was calibrated in power to -20 dBm at the tip of the cable, while the DC sweeps were performed between 1 and 100  $\mu\text{A}$ . The DC resistance was then extracted with a first-order polynomial fit to cancel out zero-crossing errors. The overall resistance was linear with DC bias. The values of the DC resistance  $R_{dc}$  are resumed in Table 5.6.

The RF measurements were de-embedded using the Cascade-Thru procedure. The circuit shown in Chapter 4, reported in Fig. 5.18 for convenience, has been adapted to the data. De-embedded and modeled data are shown in Fig. 5.19. The extracted values of contact resistance  $R_C$ , sheet resistance  $R_{\square}$  and contact capacitance  $C_C$  are listed in Table 5.7. The  $R_C$  values for the three devices are very similar, while a larger discrepancy can be found for  $R_{\square}$  and  $C_C$ .

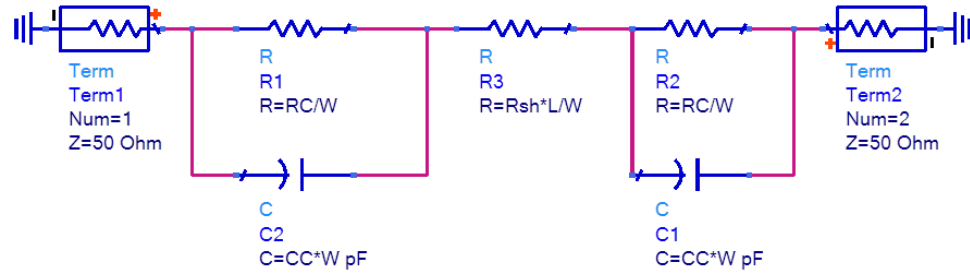
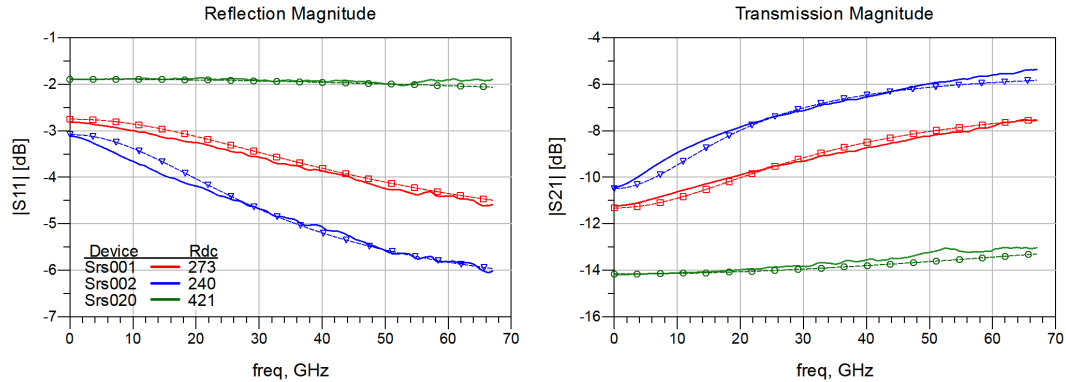


FIGURE 5.18: Equivalent circuit used for measurements matching.

FIGURE 5.19: Graphene devices measurements (solid lines) and simulations (symbols, dashed) for three electrode separations:  $0.85 \mu\text{m}$  (red squares),  $1.85 \mu\text{m}$  (blue triangles) and  $20 \mu\text{m}$  (green circles).

## 5.5 Future work

The test bed, and in particular the CPW line dimensions, must be adjusted to the final substrate as soon as the technology is optimized. During the time allowed for this study it was not possible to perform any characterization of the Nanocontacts set, which would have given the first measurement of the interfacial contact impedance in RF for graphene and Au. In addition to the experiments described in this work, a number of different test materials, thin films, not only carbonaceous, can be analyzed on this test bed and compared. The Cascade-Thru de-embedding technique should be expanded to 4-ports systems and verified on active devices in order to be a valid candidate for high-frequency semiconductor industry and research. Finally, a new optical mask that takes into account the substrate constriction should be fabricated, obtaining a much higher yield of graphene devices and allowing for the measurement of statistically meaningful data.

## 5.6 Conclusions

In conclusion, a test bed for the RF characterization of the contact impedance and its verification against the TLM method in DC has been developed, simulated and measured. A single-standard variant of the Cascade-Thru de-embedding technique has been developed, outperforming existing de-embedding methods that are commonly used in the semiconductor industry. The graphene contact parasitic and sheet resistance have been extracted from a reduced subset of the devices in the experiments. The similarity of their values suggests that the procedure used here is valid.

## References

- [1] Y.-M. Lin, A. Valdes-Garcia, S.-J. Han, D. B. Farmer, I. Meric, Y. Sun, Y. Wu, C. Dimitrakopoulos, A. Grill, P. Avouris, and K. a. Jenkins, “Wafer-scale graphene integrated circuit.”, *Science (New York, N.Y.)*, vol. 332, no. 6035, pp. 1294–7, Jun. 2011. DOI: [10.1126/science.1204428](https://doi.org/10.1126/science.1204428).
- [2] O. Habibpour, J. Vukusic, and J. Stake, “A 30-GHz Integrated Subharmonic Mixer Based on a Multichannel Graphene FET”, *IEEE Transactions on Microwave Theory and Techniques*, vol. 61, no. 2, pp. 841–847, Feb. 2013. DOI: [10.1109/TMTT.2012.2236434](https://doi.org/10.1109/TMTT.2012.2236434).
- [3] Y. Cheng, M. Deen, and C.-h. Chen, “MOSFET Modeling for RF IC Design”, *IEEE Transactions on Electron Devices*, vol. 52, no. 7, pp. 1286–1303, Jul. 2005. DOI: [10.1109/TED.2005.850656](https://doi.org/10.1109/TED.2005.850656).
- [4] M. E. Mills, P. Townsend, D. Castillo, S. Martin, and A. Achen, “Benzocyclobutene (DVS-BCB) polymer as an interlayer dielectric (ILD) material”, *Microelectronic Engineering*, vol. 33, no. 1-4, pp. 327–334, Jan. 1997. DOI: [10.1016/S0167-9317\(96\)00061-5](https://doi.org/10.1016/S0167-9317(96)00061-5).
- [5] Y.-C. Lin, C. Jin, J.-C. Lee, S.-F. Jen, K. Suenaga, and P.-W. Chiu, “Clean transfer of graphene for isolation and suspension.”, *ACS nano*, vol. 5, no. 3, pp. 2362–8, Mar. 2011. DOI: [10.1021/mn200105j](https://doi.org/10.1021/mn200105j).
- [6] C. Malec, B. Elkus, and D. Davidović, “Vacuum-annealed Cu contacts for graphene electronics”, *Solid State Communications*, vol. 151, no. 23, pp. 1791–1793, Dec. 2011. DOI: [10.1016/j.ssc.2011.08.025](https://doi.org/10.1016/j.ssc.2011.08.025).
- [7] A. Hsu, H. Wang, K. K. Kim, J. Kong, and T. Palacios, “Impact of Graphene Interface Quality on Contact Resistance and RF Device Performance”, *IEEE Electron Device Letters*, vol. 32, no. 8, pp. 1008–1010, Aug. 2011. DOI: [10.1109/LED.2011.2155024](https://doi.org/10.1109/LED.2011.2155024).
- [8] R. N. Simons, *Coplanar Waveguide Circuits, Components, and Systems*. Wiley-IEEE Press, 2001, p. 464.
- [9] A. Djordjevic, V. Likar-Smiljanic, and T. Sarkar, “Wideband frequency-domain characterization of FR-4 and time-domain causality”, *IEEE Transactions on Electromagnetic Compatibility*, vol. 43, no. 4, pp. 662–667, Nov. 2001. DOI: [10.1109/15.974647](https://doi.org/10.1109/15.974647).

- 
- [10] A. Ghannam, C. Viallon, D. Bourrier, and T. Parra, “Caracterisation Micro-onde de la resine epaisse SU8”, in *Journées de Caractérisation Microondes et Matériaux*, Brest, 2010.
- [11] HD MicroSystems, “Product Bulletin - Pi 2525, PI 2555 & PI 2574”, HD MicroSystems, Tech. Rep. November, 2012.
- [12] G. Engen and C. Hoer, “Thru-reflect-line: An improved technique for calibrating the dual six-port automatic network analyzer”, *Microwave Theory and Techniques, IEEE Transactions on*, vol. 27, no. 12, pp. 987–993, 2002. DOI: [10.1109/TMTT.1979.1129778](https://doi.org/10.1109/TMTT.1979.1129778).
- [13] R. Cheng, J. Bai, L. Liao, H. Zhou, Y. Chen, L. Liu, Y.-c. Lin, S. Jiang, Y. Huang, and X. Duan, “High-frequency self-aligned graphene transistors with transferred gate stacks.”, *Proceedings of the National Academy of Sciences of the United States of America*, vol. 109, no. 29, pp. 11 588–92, Jul. 2012. DOI: [10.1073/pnas.1205696109](https://doi.org/10.1073/pnas.1205696109).
- [14] Y. Wu, K. a. Jenkins, A. Valdes-Garcia, D. B. Farmer, Y. Zhu, A. a. Bol, C. Dimitrakopoulos, W. Zhu, F. Xia, P. Avouris, and Y.-M. Lin, “State-of-the-art graphene high-frequency electronics.”, *Nano letters*, vol. 12, no. 6, pp. 3062–7, Jun. 2012. DOI: [10.1021/nl300904k](https://doi.org/10.1021/nl300904k).





## Chapter 6

# Conclusions

Three keywords emerge from the most recent researches on graphene devices, and they are downscaling, ballistic transport and contact parasitics minimization. In this work they have been addressed in two topics: the mixed diffusive and ballistic transport in sub-micrometric graphene FETs, and the RF behavior of contact parasitics.

Chapter 3 addresses the first topic. A purely ballistic model has been enriched with a mean-free-path dependent scattering and thermalization effect, thus extending the validity of the model from a few nanometers to the micrometric scale. This simple modification to the *top of the barrier* model enables accurate simulation of a broad range of graphene based transistors. It is able to correctly describe the I–V characteristics of both ballistic and diffusive devices. Furthermore, it is able to correctly predict the behavior of both large-area and graphene nanoribbon based field effect devices. Its simplicity compared to more complex model, like full-quantum NEGF, allow for its use in graphene-enabled circuit simulation tools.

Chapter 4 addresses the RF modeling of graphene. A wide-band model describing the phenomena associated to the contact has been shown. This model allowed the extraction of resistive and capacitive parasites from DC and RF measurements of a single device, in the place of a dedicated set of devices as in the TLM method. Moreover, the parameters extracted here are frequency-independent, meaning that most of the physical phenomena involved are correctly addressed with the proper parameters.

Chapter 5 addresses the second topic: the RF behavior of contact parasitics. A dedicated test bed for the RF characterization of the contact impedance and its verification against the TLM method in DC has been developed, simulated and measured. A single-standard variant of the Cascade-Thru de-embedding technique has been developed, outperforming existing de-embedding methods that are commonly used in the semiconductor industry.

The metal/graphene contact impedance has been analyzed through the dedicated plastic test bed up to 67 GHz. The graphene contact parasitic and sheet resistance have been extracted from a reduced subset of the devices in the experiments.

## 6.1 Future work

The model of Chapter 3 will be expanded in order to include the *source starving* effect, namely the dependence of the Fermi reference potential to injected charge, thus the current. To achieve that, a mathematical relation relating the Fermi reference potential and the channel potential, independently from the operating regime, will be found. The model will be further expanded to include contact and access resistances.

The test bed of Chapter 5 will be updated with respect to the technology that has been finally used. The Nanocontacts set will be characterized, resulting in the first measurement of the interfacial contact impedance in RF for graphene and Au. This will allow for the evaluation of the occupied surface needed for sub-micrometric high-frequency FETs. More carbonaceous materials and other thin films will be deposited on this test bed and analyzed. Finally, Cascade-Thru de-embedding technique will include the Open standard (becoming a robust and high-precision variation of the Open-Thru method) and will be verified on active devices, in order to be a valid candidate for high-frequency semiconductor industry and research.

A finer description of the metal/graphene coupling mechanisms, incorporated into the quasi-ballistic model, will enable a thorough analysis of sub-micrometric high-frequency FETs in a unique framework.

# **Graphene: FET and metal contact modeling**

## **Graphène : modélisation du FET et du contact métallique**

Giancarlo Vincenzi

### **Abstract en Français**

Neuf ans sont passés depuis la découverte du graphène, tous très dense de travaux de recherche et publications que, petit à petit, ont mieux illuminé les propriétés de ce matériau extraordinaire. Avec une meilleure compréhension de ses meilleures qualités, une idée plus précise des applications que mieux pourront profiter de son use ont été défini. Dispositifs à haute fréquence, comme mélangeurs et amplificateurs de puissance, et l'électronique Flexible et Transparent sont les domaines les plus prometteurs.

Dans ces domaines une grande attention est dévouée à deux sujets : la réduction des dimensions des transistors à base de graphène, pour réduire le temps de propagation des porteurs de charge et atteindre des pourcentages de transport balistique toujours plus élevés ; et l'optimisation des parasites de contact. Tout les deux sont très bénéfiques pou la maximisation des figures de mérite du dispositif.

En cette thèse, deux modèles ont été développés pour aborder ces sujets : le premier est dédié aux transistors quasi-balistiques de graphène de grande surface comme aussi aux transistors graphène nano-ruban. Ceci démontre la corrélation entre le transport balistique et diffusive et la longueur du dispositif, et extrait les courants DC grand signal et les transconductances. Le second reproduit la conduction à haute fréquence à

travers le graphène et son impédance parasite de contact. Le dernier modèle a aussi motivé la conception et fabrication d'un test bed RF sur une technologie dédié sur plastique, fait qui permet la caractérisation RF de l'impédance de contact et de l'impédance spécifique d'interface avec du graphène monocouche accru par CVD.

# Résumé de la thèse en Français

---

## Chapitre 1 – Introduction

Le graphène, dans sa définition la plus simple, est une feuille d'un seul atome isolé du graphite. En chacun de ces feuilles, les atomes de carbone occupent les vertex des hexagones de ce qu'est parfois appelé le réseau à nid d'abeille. Ils forment des liens de type  $\sigma$  très fort avec les trois atomes adjacents à travers l'hybridation de type  $sp^2$ . L'orbitale qui reste est finalement disponible pour former un lien de type  $\pi$  avec les atomes adjacents. Le système étendu d'électrons de type  $\pi$  permet donc la conduction électrique dans le graphène et permet ses propriétés électriques et optiques [1]. La force de ses liens  $sp^2$  et sa résultante stabilité électronique sont la base de ses excellentes propriétés mécaniques : un module de Young de 1 TPa [2], qui est plus que le double de celui du carbure de silicium [3], et une force de rupture virtuellement 100 fois plus grande que pour une couche d'acier de la même épaisseur.

Les propriétés électriques du graphène ne sont pas moins étonnantes : des mobilités électroniques plus grandes que  $2.5 \times 10^5 \text{cm}^{-2}\text{V}^{-1}\text{s}^{-1}$  ont été trouvées à température ambiante, quatre fois plus grande de celle de l'état de l'art des semi-conducteurs III-V [4] et 200 fois celle du silicium, grâce à une réduite interaction électron-phonon [5] lorsque le substrat est choisi attentivement [6] ou éliminé à travers la technologie suspendue [7]. Ces valeurs très élevées sont associées à des très longues distances entre des événements de scattering pour des électrons en voyage : des mean free paths plus grands de  $1 \mu\text{m}$  ont été reportés [6], fait qui permet l'exploration de l'électronique balistique à température ambiante avec des capacités technologiques qu'on possède aujourd'hui. Des valeurs plus élevées de mobilités ont été obtenues pour le graphène suspendu à la température de l'hélium liquide (plus que  $1.0 \times 10^6 \text{cm}^{-2}\text{V}^{-1}\text{s}^{-1}$  [8]), mais non autant bonne que les alliages de semi-conducteurs ( $35.0 \times 10^6 \text{cm}^{-2}\text{V}^{-1}\text{s}^{-1}$  a été obtenu [9]), fait qui soutient et limite l'intérêt de la recherche dans l'opération à température ambiante.

Le graphène a été montré pour être vraiment un matériau unique, avec de nombreuses excellentes propriétés qui ne peuvent pas être trouvés tout à fait dans un matériau seul. Toutefois, les valeurs insatisfaisantes d'autres propriétés essentielles entravent son application comme un remplacement pour chaque technologie électronique développée à jour : Dans l'électronique haute fréquence, le graphène ne remplacera probablement Si ou semi-conducteurs III-V à court terme. Le domaine de l'électronique flexible et transparent est plutôt rapidement de l'ampleur, puisque la matière la plus utilisée aujourd'hui, Indium-Tin Oxide, est de plus en plus cher et difficile à trouver. Le graphène, avec ses propriétés mécaniques et optiques supérieures a déjà attiré l'attention de l'électronique grand public : géants comme Samsung et Sony [10]. Tant haute fréquence et flexibles domaines de l'électronique ont besoin d'une étude précise des parasites de contact de graphène. Enfin, il ya un domaine entièrement nouveau qui peut être exploré et qui peut ouvrir la voie à ondes millimétriques et THz électronique, et qui est à température ambiante électronique balistique [11]. Cette thèse examinera les effets du transport balistique et les parasites de contact, respectivement sur les effets des transistors et des interconnexions

### **Structure de la thèse**

Le Chapitre 2 introduira un ensemble de concepts fondamentaux sur la physique du graphène. Ceux-ci vont être utilisés pour comprendre l'état de l'art sur le modeling du graphène. Deux aspects principaux vont être discutés : d'abord une enquête du modeling de transistors à effet de champ en DC sera faite. Dans une deuxième partie, le modeling des structures passives en graphène sera passé en revue. Le contact métallique et la propagation électronique dans le graphène sont considérés comme deux aspects du même sujet intimement connectés, et leur analyse sera développée en DC comme en RF.

Dans le Chapitre 3 le modèle DC d'un FET de nanoruban de graphène sera présenté, avec les modifications nécessaires pour sa extension à dispositifs de graphène grand surface.

Dans le Chapitre 4 une structure RF, une ligne CPW chargée avec du graphène, sera analysée à travers d'un circuit équivalent pour le graphène et du modeling électromagnétique de la ligne. Ceci permettra l'extraction de l'impédance de contact métal/graphène.

Dans le chapitre 5 la conception d'une structure de RF améliorée avec un ensemble de normes de-embedding sera montré, avec des mesures, l'analyse des données EM et rétro-résultats de simulations. Cela fournira un montage d'accès à faibles pertes pour la caractérisation RF de graphène et de-embedding de données. La feuille de graphène et l'impédance de contact seront mesurées et analysées en fréquence à la fois faible et élevée.

Dans le chapitre des conclusions les innovations par rapport à l'état de l'art contenues dans ce manuscrit seront reprises, et de nouvelles orientations possibles de travail seront présentées.

[1] P. Wallace, "The Band Theory of Graphite", *Physical Review*, vol. 71, no. 9, pp. 622-634, May 1947. doi: 10.1103/PhysRev.71.622.

[2] C. Lee, X. Wei, J. W. Kysar, and J. Hone, "Measurement of the elastic properties and intrinsic strength of monolayer graphene.", *Science (New York, N.Y.)*, vol. 321, no. 5887, pp. 385-388, Jul. 2008. doi: 10.1126/science.1157996.

[3] L. Tong, M. Mehregany, and L. G. Matus, "Mechanical properties of 3C silicon carbide", *Applied Physics Letters*, vol. 60, no. 24, p. 2992, 1992. doi: 10.1063/1.106786.

[4] K. Nakayama, K. Nakatani, S. Khamseh, M. Mori, and K. Maezawa, "Step Hall Measurement of InSb Films Grown on Si(111) Substrate Using InSb Bilayer", *Japanese Journal of Applied Physics*, vol. 50, 01BF01, Jan. 2011. doi: 10.1143/JJAP.50.01BF01.



- [5] S. Morozov, K. Novoselov, M. Katsnelson, F. Schedin, D. Elias, J. Jaszczak, and A. Geim, "Giant Intrinsic Carrier Mobilities in Graphene and Its Bilayer", *Physical Review Letters*, vol. 100, no. 1, pp. 11{14, Jan. 2008. doi: 10.1103/PhysRevLett.100.016602.
- [6] A. S. Mayorov, R. V. Gorbachev, S. V. Morozov, L. Britnell, R. Jalil, L. a. Ponomarenko, P. Blake, K. S. Novoselov, K. Watanabe, T. Taniguchi, and a. K. Geim, "Micrometerscale ballistic transport in encapsulated graphene at room temperature.", *Nano letters*, vol. 11, no. 6, pp. 2396{9, Jun. 2011. doi: 10.1021/nl200758b.
- [7] K. Bolotin, K. Sikes, Z. Jiang, M. Klima, G. Fudenberg, J. Hone, P. Kim, and H. Stormer, "Ultrahigh electron mobility in suspended graphene", *Solid State Communications*, vol. 146, no. 9-10, pp. 351{355, 2008.
- [8] E. V. Castro, H. Ochoa, M. I. Katsnelson, R. V. Gorbachev, D. C. Elias, K. S. Novoselov, a. K. Geim, and F. Guinea, "Limits on Charge Carrier Mobility in Suspended Graphene due to Flexural Phonons", *Physical Review Letters*, vol. 105, no. 26, p. 266 601, Dec. 2010. doi: 10.1103/PhysRevLett.105.266601.
- [9] V. Umansky, M. Heiblum, Y. Levinson, J. Smet, J. N ubler, and M. Dolev, "MBE growth of ultra-low disorder 2DEG with mobility exceeding  $35 \times 10^6 \text{cm}^2/\text{Vs}$ ", *Journal of Crystal Growth*, vol. 311, no. 7, pp. 1658{1661, Mar. 2009. doi: 10.1016/j.jcrysgro.2008.09. 151.
- [10] T. Kobayashi, M. Bando, N. Kimura, K. Shimizu, K. Kadono, N. Umez, K. Miyahara, S. Hayazaki, S. Nagai, Y. Mizuguchi, Y. Murakami, and D. Hobara, "Production of a 100-m-long high-quality graphene transparent conductive film by roll-to-roll chemical vapor deposition and transfer process", *Applied Physics Letters*, vol. 102, no. 2, p. 023 112, 2013. doi: 10.1063/1.4776707.
- [11] G. Moddel, Z. Zhu, S. Grover, and S. Joshi, "Ultrahigh speed graphene diode with reversible polarity", *Solid State Communications*, vol. 152, no. 19, pp. 1842{1845, Oct. 2012. doi: 10.1016/j.ssc.2012.06.013.

## Chapitre 2 – Etat de l’art

L'étude du contact métal/graphène et de la propagation à haute fréquence est traitée très différemment entre les divers domaines d'études. Ils doivent être considérés comme des aspects d'une même chose, plus grand, problème. Cependant, les examens de contact sont effectués uniquement à la fréquence zéro. Quelques études empiriques considèrent ces deux aspects, mais parfois avec des modèles trop simplifiés.

D'autre part, dans la modélisation de la FET parasite de contact est prise en compte. Ses effets sur la Figures de Mérite à haute fréquence sont profondément évalués en raison de l'impact sévère sur le courant de transconductance et de sortie. Performances à haute fréquence sont la cible principale de ces expériences et modèles, soulignant l'importance de l'échelle sub-micrométrique pour atteindre des performances encore plus élevées. Et pourtant, les parasites de contact sont généralement représentés par une simple résistance, évaluée en continu et indépendante de la fréquence.

En conclusion, la nécessité d'un modèle universel reliant l'investigation plus fine de la physique impliquée dans les dispositifs FET sous- micrométriques et la propagation haute fréquence prend une importance croissante. Ce travail vise à rapprocher ces deux domaines, en mettant à la base de leur intégration dans un seul domaine d'étude.

## Chapitre 3 – Modèle DC

Dans ce chapitre, le travail sur la modélisation de dispositifs actifs DC graphène sera présenté. Le modèle décrit est basé sur l'approche Top-of-the-barrier, qui est un modèle balistique physique semi-analytique [1].

### Motivation

La grande majorité des modèles utilisés aujourd'hui pour simuler les caractéristiques IV des dispositifs de graphène sont basées sur le mécanisme de transport de dérive-diffusion (DD), sur lequel le modèle industriel standard pour Si CMOS, le BSIM est fondée ainsi. DD est basé sur l'hypothèse que dans le canal du transistor (ou tout autre conducteur) une certaine quantité de centres de diffusion existe, et que la conductivité dépend du nombre de porteurs chargés il existe et à quelle fréquence elles entrent en collision avec un diffuseur, le support vitesse de dérive est une fonction du champ électrique longitudinal (donnée par la polarisation de drain) et des paramètres de la mobilité et de la vitesse de saturation. Tension et le courant sont liés par le modèle de Drude. Toutefois, si la dispersion est absent, comme dans un transistor balistique idéal, la vitesse des transporteurs prend sa valeur maximale, ce n'est plus directement reliée au champ électrique longitudinal, mais avec la chute de potentiel entre la source et le drain à la place. DD modèles peuvent inclure empiriquement l'augmentation du courant de saturation qui vient des effets balistiques, par exemple à travers le modèle de limite de vitesse Fin Source comme cela se fait pour Si dans BSIM4v4.7 [2], mais leur validité dans les régimes à proximité de transport balistique idéal devient discutable.

La particularité de graphène est de soutenir un nombre très limité de la diffusion, même à température ambiante, en particulier lorsque l'interaction avec le substrat est réduite [3]. Par ailleurs, en même temps que la qualité des échantillons de graphène s'améliore, les longueurs de canal sont trop réduites, ce qui signifie que de plus en plus grandes parties de la conduction des électrons doivent compter sur le transport balistique [4]. Un modèle balistique de nano-transistors de graphène devient

approprié, mais d'autre part, leur validité est généralement donnée que lorsque le transport balistique est dominant [5].

Enfin, de nombreux modèles se fragmentent leur fonctionnement dans plusieurs segments ou des régimes, en fonction de la forme de la courbe  $I_D(V_{DS})$  (linéaire, quasi-saturation, deuxième linéaire) ou le type de charges à l'intérieur du canal (soit des électrons ou des trous, ou des deux d'entre eux). Dans ce dernier contexte, le mot "ambipolaire" est souvent utilisée même si inapproprié [6]. La fragmentation de l'opération peut conduire à des discontinuités dans la transconductance  $g_m$  ou de sa dérivée.

### **Objectives de l'étude**

Cette partie du travail vise à trouver un modèle qui peut simuler correctement les deux transistors à effet de champ à l'échelle nanométrique balistique comme à celle microscopique conventionnelle. Ce modèle devrait s'appuyer sur des équations physiques, avec une utilisation minimale des paramètres empiriques. Enfin, son fonctionnement ne doit pas être fragmenté en différents régimes.

### **Résultats**

Le modèle proposé dans [7] a été validée par rapport à deux dispositifs présentés dans la littérature. Un transistor de graphène nano-ruban de canal étroit décrit dans [8] et un grand espace large FET canal de graphène décrit dans [9].

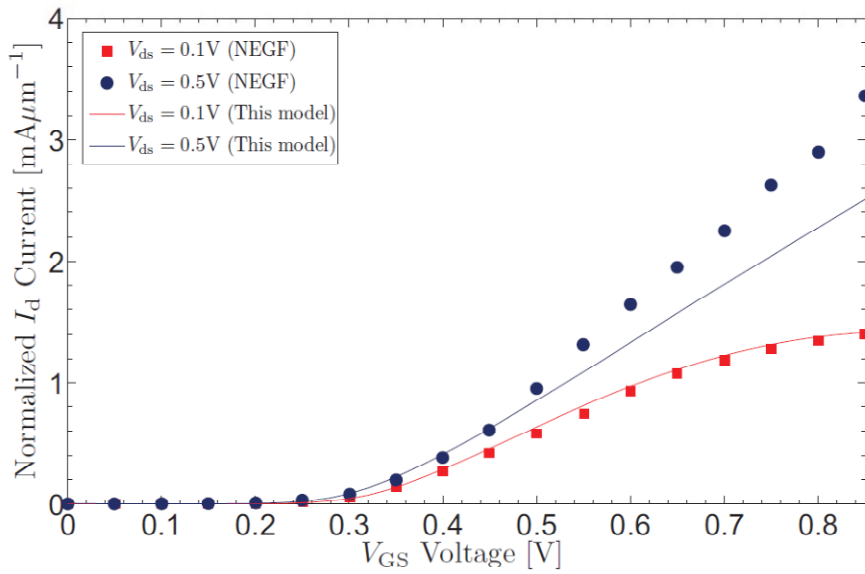


Figure 1 - Caractéristique de transfer ( $I_d$ - $V_{GS}$ ) in échelle linéaire de ce modèle comparé a celui de type NEGF en [8].

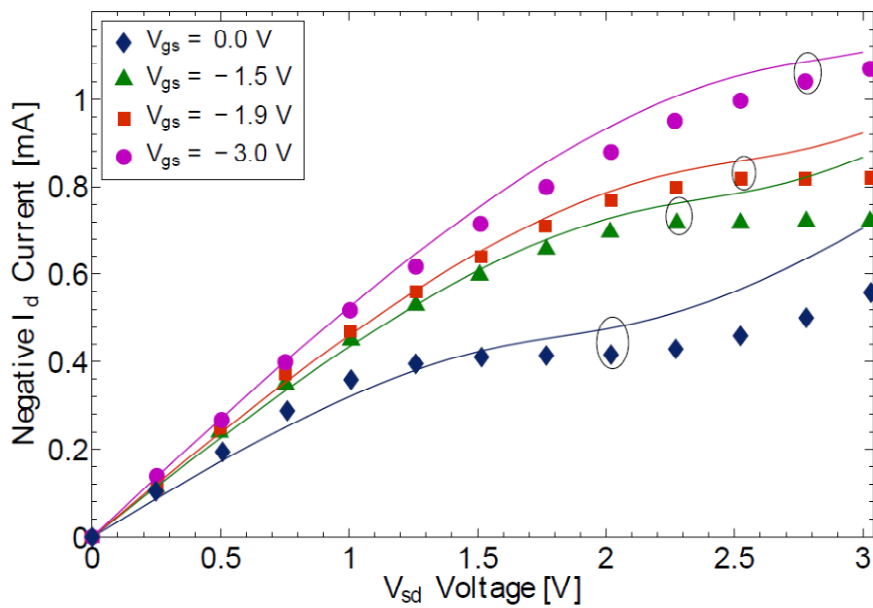


Figure 2 - Courante  $I_d$ ( $V_{sd}$ ) pour le deuxième FET (ligne pleine) pour tensions de grille entre  $V_{gs}=0V$  et  $-3V$  comparée à les mesures (symboles)

En résumé, le modèle décrit utilise quatre paramètres pour ajuster les résultats expérimentaux.

## Travaux Futures

Le modèle présenté a jusqu'ici deux problèmes qui limitent la qualité de la simulation, respectivement dans les cas GNR-FET et GFET. Le premier est le potentiel de Fermi de référence, qui est réglé sur le potentiel de source qui est considérée fixe pour l'ensemble du fonctionnement du transistor GNR-FET. Ceci est incorrect, les mêmes auteurs ont proposé une modification dans le modèle impliquant un nouveau paramètre libre à inclure pour chaque point et qui se trouve de façon empirique. Une meilleure solution serait d'obtenir une relation entre la charge injectée, le courant et le potentiel de référence, qui serait autorisé à suivre dans une certaine mesure le potentiel de la chaîne.

Un autre point est la modélisation de contact et d'accès résistances à la chaîne, l'évolution du modèle actuel du transistor intrinsèque à un modèle extrinsèque complète. Étant donné que le modèle ne comporte aucune expression inversible, par opposition à, par exemple, la loi d'Ohm, une itération de l'auto-cohérent de tensions externes appliquées et les courants internes calculées par le modèle est nécessaire.

## Conclusions

Une simple modification du modèle Top-of-the-barrier qui permet une simulation précise d'un large éventail de transistors à base de graphène a été présentée. Le modèle conserve la simplicité d'une approche élément localisé et est en mesure de décrire correctement les caractéristiques I-V des deux dispositifs balistiques et de diffusion. En outre, il est capable de prédire correctement le comportement de dispositifs à effet de champ à la fois de grande surface ainsi que de graphène nanoruban. Sa simplicité par rapport à des modèles plus complexes, comme le full-quantum NEGF, permet sa utilisation dans des outils de simulation de circuit graphène permis.

[1] A. Rahman, S. Datta, and M. Lundstrom, "Theory of ballistic nanotransistors", IEEE Transactions on Electron Devices, vol. 50, no. 9, pp. 1853-1864, Sep. 2003. doi: 10.1109/TED.2003.815366.

- [2] T. H. Morshed, D. D. Lu, W. ( Yang, V. M. Dunga, X. ( Xi, J. He, W. Liu, Kanyu, M. Cao, X. Jin, J. J. Ou, M. Chan, A. M. Niknejad, and C. Hu, \BSIM4v4.7 MOSFET Model", Department of Electrical Engineering and Computer Sciences, University of California, Berkeley, Berkeley, Tech. Rep., 2011.
- [3] A. S. Mayorov, R. V. Gorbachev, S. V. Morozov, L. Britnell, R. Jalil, L. a. Ponomarenko, P. Blake, K. S. Novoselov, K. Watanabe, T. Taniguchi, and a. K. Geim, \Micrometerscale ballistic transport in encapsulated graphene at room temperature.", *Nano letters*, vol. 11, no. 6, pp. 2396{9, Jun. 2011. doi: 10.1021/nl200758b.
- [4] Y. Wu, V. Perebeinos, Y.-m. Lin, T. Low, F. Xia, and P. Avouris, \Quantum behavior of graphene transistors near the scaling limit.", *Nano letters*, vol. 12, no. 3, pp. 1417{23, Mar. 2012. doi: 10.1021/nl204088b.
- [5] J. Chauhan, L. Liu, Y. Lu, and J. Guo, \A computational study of high-frequency behavior of graphene field-effect transistors", *Journal of Applied Physics*, vol. 111, no. 9, p. 094 313, 2012. doi: 10.1063/1.4712323.
- [6] J. G. Champlain, \On the use of the term \ambipolar"", *Applied Physics Letters*, vol. 99, no. 12, p. 123 502, 2011. doi: 10.1063/1.3641898.
- [7] G. Vincenzi, G. Deligeorgis, F. Coccetti, M. Dragoman, L. Pierantoni, D. Mencarelli, and R. Plana, \Extending ballistic graphene FET lumped element models to di usive devices", *Solid-State Electronics*, vol. 76, pp. 8{12, Oct. 2012. doi: 10.1016/j.sse. 2012.06.004.
- [8] G. Fiori and G. Iannaccone, \Simulation of Graphene Nanoribbon Field-E ect Transistors", *IEEE Electron Device Letters*, vol. 28, no. 8, pp. 760{762, Aug. 2007. doi:10.1109/LED.2007.901680.
- [9] I. Meric, M. Y. Han, A. F. Young, B. Ozyilmaz, P. Kim, and K. L. Shepard, \Current Saturation in zero-bandgap, top-gated graphene field-effect transistors.", *Nature Nanotechnology*, vol. 3, no. 11, pp. 654{9, Nov. 2008. doi: 10.1038/nnano.2008.268.

## Chapitre 4

Dans ce chapitre, le travail sur la modélisation DC et RF de dispositifs passifs graphène sera présenté. Un modèle d'éléments à constantes localisées avec les paramètres indépendants de la fréquence sera utilisé pour extraire la résistance du matériau et de l'impédance des dispositifs de contact analysés. Ce modèle sera utilisé pour projeter la performance attendue à partir des paramètres de la littérature.

### Motivation

Les paramètres qui ont une influence sur les performances à haute fréquence du transistor, en particulier la figure de mérite (FOM) de fréquence de coupure et la fréquence d'oscillation maximale, sont facilement reconnaissables dans le petit modèle de signal du transistor FET, qui pour le graphène à base de dispositifs maintient la même topologie et composants que celui d'origine pour les semi-conducteurs.

### Objectives de l'étude

Cette partie du travail vise à trouver un modèle de circuit équivalent pour les éléments de graphène passifs. Ce modèle doit être adapté à l'extraction de l'impédance de contact et la résistivité de la matière par la caractérisation DC et RF d'un dispositif unique. Il devrait être composé par des paramètres indépendants de la fréquence et est valable dans l'ensemble du spectre de mesures (DC à 110 GHz).

### Résultats

L'accord entre modèle et figure est montré en Fig. 3.



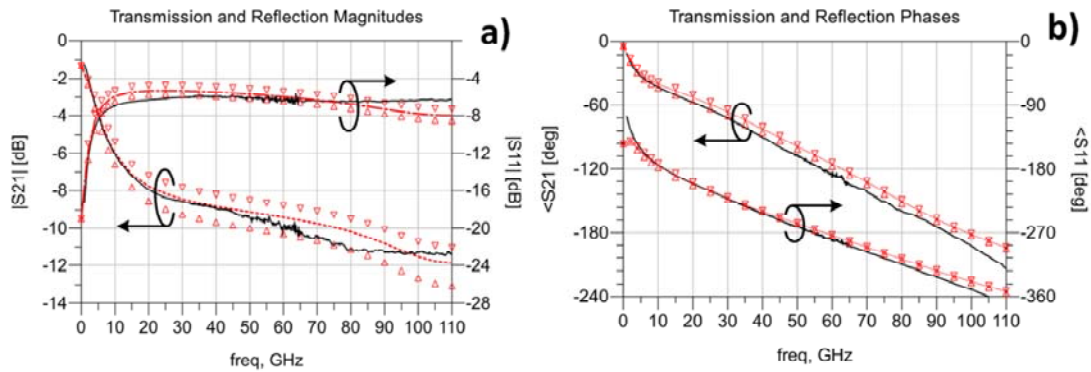


Figure 3 - Paramètres S mesurés (ligne pleine noire) et simulations (ligne rouge) pour la structure CPW chargée en graphène. Les triangles indiquent le changement maximal par rapport à une variation du 10% des paramètres de circuit. (a) Module, (b) Phase.

## Conclusions et travaux futurs

Dans ce chapitre, un modèle de bande large décrivant des phénomènes associés à l'un contact a été établi. Ce modèle a permis l'extraction de résistifs et capacitifs parasites de DC et des mesures RF d'un seul dispositif, à la place d'un ensemble dédié de dispositifs que dans la méthode TLM. De plus, les paramètres extraits sont ici indépendante de la fréquence, ce qui signifie que la plupart des phénomènes physiques mis en jeu sont correctement adressées avec les paramètres appropriés, par opposition à d'autres modèles présentant des résistances et des condensateurs dont les valeurs dépendent de la fréquence. Toutefois, afin de compléter la validation du modèle, une caractérisation des RF de structures de type TLM est nécessaire. Ce genre de structures sont généralement basse fréquence seulement et ne prend pas en charge la transmission d'un signal RF ondes millimétriques sans encourir de pertes de désadaptation graves et le couplage, ce qui rend impossible d'établir une relation entre l'impédance à haute fréquence et les dimensions géométriques. De plus, la longueur de transfert a été étudiée qu'une seule fois et en un courant continu, et aucun modèle définissant une quantité équivalente à la capacitance de contact a été mis au point à ce jour. Une structure de test RF dédié avec la longueur et la largeur de graphène doit être fabriqué et analysé afin de comparer les paramètres extraits par le

modèle présenté ici avec celles extraites par TLM. Ce sujet sera abordé dans le prochain chapitre.

## Chapitre 5

Dans ce chapitre, la conception d'un banc d'essai en plastique dédié à la mesure de l'impédance de surface et de contact de différents matériaux sera montrée, avec les valeurs attendues de la caractérisation d'impédance et a effectué des mesures. Un ensemble de matières carbonées, y compris monocouche de graphène, sera analysé in DC et RF par la méthode TLM et par le modèle présenté dans le chapitre 4, montrant une validation uniforme du même. Enfin, l'analyse de l'impédance RF de contacts de dimensions réduites, nommés ici nano-contacts, sera montrée.

### Motivation

L'impédance d'un contact métal / de graphène est responsable de la majeure partie de la dégradation des performances du dispositif. D'autres éléments qui affectent gravement les performances sont les lignes de structure et d'accès reliant les sondes RF à l'appareil réel. Chaque unité Ohm de l'inadéquation de 50Ohm dans l'impédance caractéristique introduit une réflexion de près de 4 % de la puissance d'entrée, alors une résistance série introduit mismatch et pertes ohmiques pour environ 4% par Ohm. Grâce à une conception soignée de lignes d'accès RF, il est possible de minimiser désadaptation d'impédance et la résistance des sondes / de série de l'appareil et de maximiser le signal délivré.

Dans certaines œuvres, des structures de réglage d'impédance sont présents comme inducteurs [1] ou micro filtres [2] fabriqués sur les mêmes wafers des amplificateurs et des mélangeurs en graphène. Ces approches sont très efficaces pour éliminer les pertes de désadaptation en commun source FET de graphène avec une au moins dans une certaine mesure, l'impédance d'entrée connue, élevé. Malheureusement, dans le cas d'une étude exploratoire lorsque l'impédance d'entrée est inconnue, il n'est pas pratique de concevoir et de fabriquer une structure d'accord sur la plaquette.

Pour surmonter cette limitation deux stratégies sont généralement appliqués en même temps : la fabrication des standards de de-embedding connus sur le même

wafer du dispositif, et, comme indiqué précédemment, la conception de lignes d'accès bien à 50 Ohm. La première permet d'appliquer les méthodes mathématiques de déplacer le plan de référence à un point plus proche de l'objet à tester (DUT), l'élimination du retard de phase et la plupart, sinon la totalité, du mismatching et des pertes ohmiques associé à des lignes d'accès, celui-ci prend en charge une meilleure manipulation de la gamme dynamique de l'instrument de mesure (typiquement, mais sans être limité, de 50 dB pour un VNA) et réduit au minimum l'impact de l'erreur associée à la de-embedding de l'objet sous test après la mesure de ces normes.

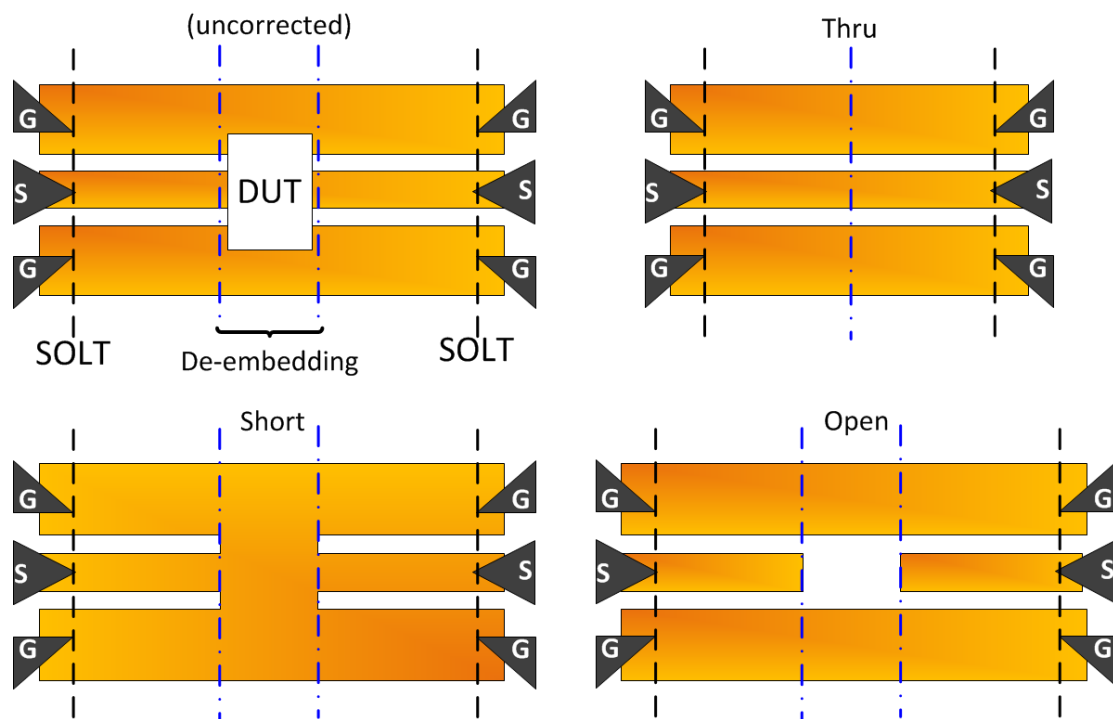


Figure 4 - Standards utilisés pour des techniques de de-embedding.

Dans la Fig. 4 un DUT hypothétique avec certaines normes de de-embedding est affiché. Les lignes verticales en pointillé correspondent à des plans de référence de la mesure en fonction du calibrage de SOLT, fait avec un kit de calibrage séparées sur de l'alumine et largement adoptée, seul ou en tant que le premier d'un protocole d'étalonnage en deux étapes : il permet de retirer les effets de câbles, des sondes et de l'instrument lui-même. Les lignes en traits pointillés verticaux correspondent aux plans

de de-embedding définies par les normes connues. Différentes techniques existent, parmi lesquelles la plus communément adoptée sont l'Open-Short et Thru-Reflect-Line (TRL, qui comprend une série de lignes à retard non représenté sur la figure). Après la de-embedding, les lignes d'accès sont pratiquement supprimées de l'objet sous test.

Pour les dispositifs à ondes mm et sous-mm, les FOM intrinsèques sont souvent considérés comme de plus grand impact que les FOM extrinsèques et d'autres paramètres de conception tels que l'empreinte de l'appareil. Même si les procédures de-embedding sont largement appliquées et raffiné, le parasite de contact graphène/métal peut profondément affecter non seulement les extrinsèques mais aussi les FOM intrinsèques si ceci n'est pas correctement éliminés. La procédure de de-embedding Open-Short est généralement appliquée aux mesures de dispositif semi-conducteur, mais dans la littérature récente sur les dispositifs de graphène il n'est pas clair si la résistance de contact graphène/métal est retirée de données présentées. Cependant, une étude de son effet à des fréquences élevées, où ces appareils fonctionnent, est en tout cas nécessaire.

### Objectives de l'étude

L'objectif principal de ce chapitre est la construction d'un banc d'essai à faible perte pour la caractérisation RF de graphène monocouche et autres couches minces de matériaux carbonés. Ce substrat doit fournir un ensemble de normes de de-embedding et de dispositifs de référence pour l'extraction et l'isolement de l'impédance du matériau de test. Ce banc d'essai doit prendre en charge les deux expériences suivantes.

1. **TLM à Haute Fréquence** : L'extraction de l'impédance de contact et de surface d'un matériau en essai, en particulier graphène monocouche. Un ensemble de lignes d'accès RF à deux ports doit être construit, et la séparation entre les deux électrodes centrales doit être modifiée dans l'ensemble. Cela devrait permettre

la linéarisation de la résistance de contact DC sur la séparation des contacts, et la mesure simultanée de l'impédance de contact  $Z_c(\omega)$  pour chaque dispositif.

2. **Nano-contacts** : Le développement d'un modèle reliant  $Z_c(\omega)$  avec des longueurs de contact à l'échelle nanométrique. Un ensemble de lignes d'accès à deux ports avec différentes longueurs de contact sous-micrométriques doit être construit. Le nouveau modèle devrait fournir la longueur de contact minimal pour atteindre la saturation de  $Y_c(\omega)$  pour une fréquence donnée.

## Résultats

CVD monocouche graphène fourni par Graphene Supermarket a été déposé sur le substrat polyimide comme le montre la figure 5. De même pour SU-8, le PI trop subi quelques constriction après l'étape de durcissement, estimée à  $<0,4\%$ . Ceci a empêché l'alignement correct des formes de mise en forme graphène pendant l'étape de lithographie optique. En outre, dans certains endroits graphène manquait. Trois dispositifs ont été correctement fabriqués, tous de type Série et avec des séparations d'électrodes respectivement de 1, 2 et 20  $\mu\text{m}$ .

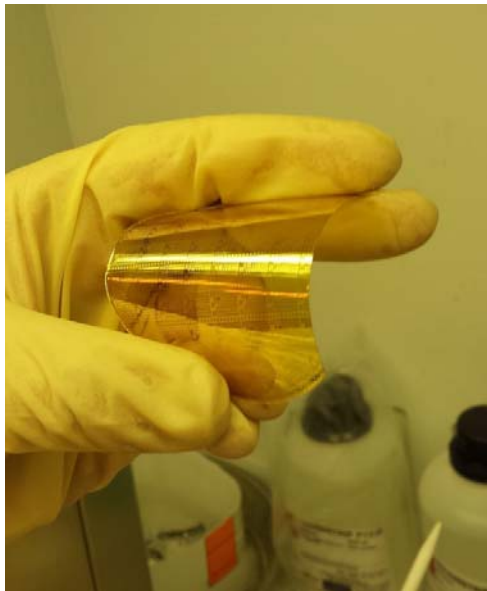


Figure 5 - Substrat en Polyimide avec dispositifs intégrés.

Mesures de paramètres S ont été réalisées avec un Agilent PNA-X jusqu'à 67 GHz et avec un Keithley 2410 SMU connecté sur le feed DC du VNA. Afin d'éviter les effets non linéaires de la conductivité en fonction de graphène polarisation en courant continu et de la puissance RF, deux mesures ont été effectuées à faible puissance. Le VNA a été calibré en puissance à -20 dBm à l'extrémité du câble, tandis que les balayages ont été effectués à courant continu entre 1 et 100  $\mu$ A. La résistance DC est ensuite extraite avec un ajustement polynomial de premier ordre à annuler les erreurs de passage à zéro.

Les mesures RF ont été dé-intégrée en utilisant la procédure Cascade-Thru. Le circuit représenté sur la figure 6 a été adapté pour les données. Les données modélisées et mesurés après de-embedding sont présentées dans la figure 7. Les valeurs extraites de la résistance de contact  $R_c$ , feuille résistance  $R_{\square}$  et contacts capacité  $C_c$  sont listés dans le Tableau 1. Les valeurs de  $R_c$  pour les trois dispositifs sont très similaires, alors qu'une plus grande différence peut être trouvée pour  $R_{\square}$  et  $C_c$ .

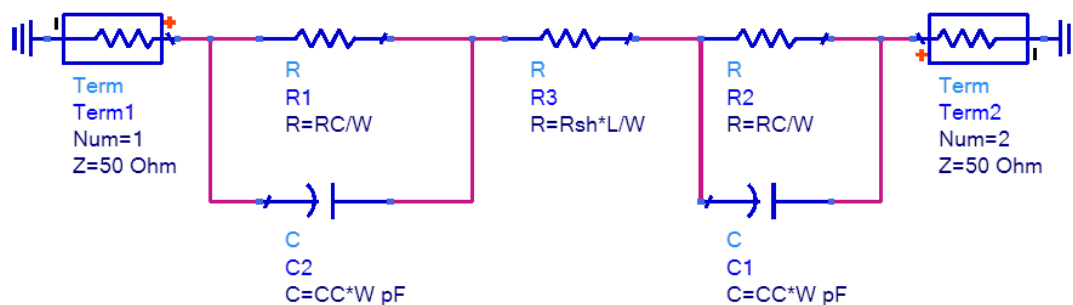


Figure 6 - Circuit equivalent utilisé pour le matching des mesures.

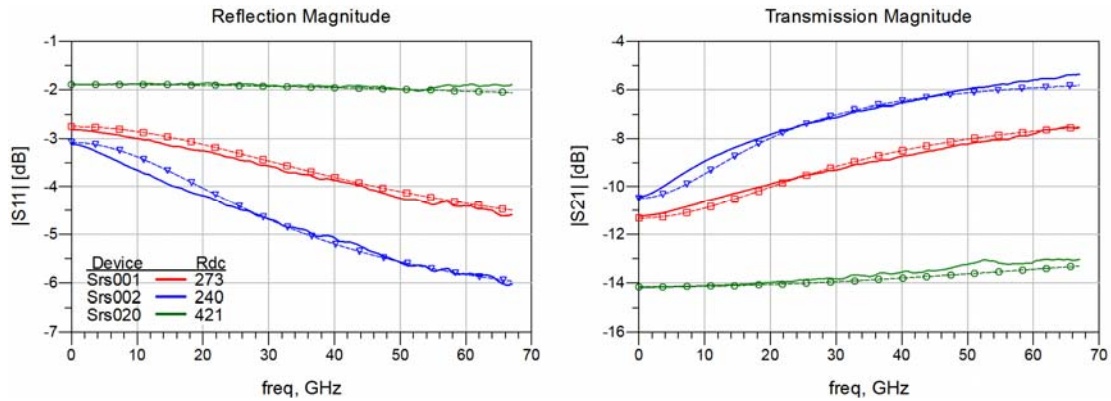


Figure 7 - Mesures (ligne pleine) et simulations (symbols) des dispositifs à base de graphène.

Device	$R_{dc}$ [ $\Omega$ ]	$R_{\square}$ [ $\Omega$ ]	$R_C$ [ $\Omega \cdot \text{mm}$ ]	$C_C$ [pF/mm]
Srs001	273	2933	1.70	3.73
Srs002	240	1021	1.64	6.40
Srs020	421	251	2.02	0.78

Tableau 1 - Resistance de contact et de surface.

## Travaux futures

Le banc d'essai, et en particulier les dimensions de la ligne de CPW, doit être ajustée sur le substrat final, dès que la technologie est optimisée. Pendant le temps imparti pour cette étude, il n'était pas possible d'effectuer une caractérisation de l'ensemble nano-contacts, qui aurait donné la première mesure de l'impédance de contact d'interface en RF pour le graphène et Au. En plus des expériences décrites dans ce travail, un certain nombre de matériaux d'essai différents, des films minces, non seulement carboné, peut être analysé sur ce banc d'essai et de comparaison. La Cascade-Thru technique de de-embedding devrait être étendue aux systèmes 4-ports et vérifiée sur les dispositifs actifs pour être un candidat valable pour l'industrie des semi-conducteurs à haute fréquence et de la recherche. Enfin, un nouveau masque optique qui prend en compte le rétrécissement du substrat doit être fabriqué, l'obtention d'un rendement beaucoup plus élevé de dispositifs de graphène et permettant la mesure de données statistiquement significatives.



[1] Y.-M. Lin, A. Valdes-Garcia, S.-J. Han, D. B. Farmer, I. Meric, Y. Sun, Y. Wu, C. Dimitrakopoulos, A. Grill, P. Avouris, and K. a. Jenkins, "Wafer-scale graphene integrated circuit.", *Science* (New York, N.Y.), vol. 332, no. 6035, pp. 1294-1297, Jun. 2011. doi: 10.1126/science.1204428.

[2] O. Habibpour, J. Vukusic, and J. Stake, "A 30-GHz Integrated Subharmonic Mixer Based on a Multichannel Graphene FET", *IEEE Transactions on Microwave Theory and Techniques*, vol. 61, no. 2, pp. 841-847, Feb. 2013. doi: 10.1109/TMTT.2012.2236434.

## Chapitre 6 - Conclusions

Trois mots-clés émergents des plus récentes recherches sur les dispositifs de graphène, et ils sont la réduction d'échelle, transport balistique et parasites de contact minimisation. Dans ce travail, ils ont été abordés dans deux thèmes : le transport par diffusion et balistique mixte en sous-micrométriques FET de graphène, et le comportement de RF de parasites de contact.

Chapitre 3 aborde le premier sujet. Un modèle purement balistique a été enrichi avec le traitement du scattering dépendant du mean-free-path et de l'effet de thermalisation, prolongeant ainsi la validité du modèle de quelques nanomètres à l'échelle micrométrique. Cette simple modification du modèle top-of-the-barrier permet la simulation précise d'un large éventail de transistors à base de graphène. Il est capable de décrire correctement les caractéristiques I- V des deux dispositifs balistiques et de diffusion. En outre, il est capable de prédire correctement le comportement des deux grandes surfaces et graphène nano-ruban dispositifs à effet de champ à base. Sa simplicité par rapport à des modèles plus complexes, comme le NEGF, permet son utilisation dans des outils de simulation de circuit graphène permis.

Chapitre 4 traite de la modélisation de la RF de graphène. Un modèle à large bande décrivant des phénomènes associés à l'un contact a été établi. Ce modèle a permis l'extraction de résistifs et capacitifs parasites de DC et des mesures RF d'un seul appareil, à la place d'un ensemble dédié de dispositifs que dans la méthode TLM. En outre, les paramètres extraits ici sont indépendants de la fréquence, ce qui signifie que la plupart des phénomènes physiques mis en jeu sont correctement traités avec les paramètres appropriés.

Chapitre 5 aborde la deuxième question : le comportement RF de parasites de contact. Un banc d'essai dédié à la caractérisation RF de l'impédance de contact et son contrôle contre la méthode TLM à Washington DC a été développé, simulée et mesurée. Une variante d'une seule norme de la Cascade-Thru technique de de-embedding a été développée, par rapport aux méthodes de de-embedding existants qui sont couramment utilisés dans l'industrie des semi-conducteurs. L'impédance de contact métal/graphène a été analysée par le test de plastique dédié lit jusqu'à 67 GHz. Le graphène contacts parasite et la résistance de la feuille ont été extraites à partir d'un sous-ensemble réduit des appareils dans les expériences.